



UNIVERSITY
OF WOLLONGONG
AUSTRALIA

University of Wollongong
Research Online

University of Wollongong Thesis Collection
1954-2016

University of Wollongong Thesis Collections

2016

Flexible graphene based materials for energy storage

Kewei Shu
University of Wollongong

UNIVERSITY OF WOLLONGONG

COPYRIGHT WARNING

You may print or download ONE copy of this document for the purpose of your own research or study. The University does not authorise you to copy, communicate or otherwise make available electronically to any other person any copyright material contained on this site. You are reminded of the following:

This work is copyright. Apart from any use permitted under the Copyright Act 1968, no part of this work may be reproduced by any process, nor may any other exclusive right be exercised, without the permission of the author.

Copyright owners are entitled to take legal action against persons who infringe their copyright. A reproduction of material that is protected by copyright may be a copyright infringement. A court may impose penalties and award damages in relation to offences and infringements relating to copyright material. Higher penalties may apply, and higher damages may be awarded, for offences and infringements involving the conversion of material into digital or electronic form.

Recommended Citation

Shu, Kewei, Flexible graphene based materials for energy storage, Doctor of Philosophy thesis, Intelligent Polymer Research Institute, University of Wollongong, 2016. <http://ro.uow.edu.au/theses/4843>

Research Online is the open access institutional repository for the University of Wollongong. For further information contact the UOW Library: research-pubs@uow.edu.au



UNIVERSITY
OF WOLLONGONG
AUSTRALIA

**Australian Research Council Centre of Excellence for Electromaterials Science
The Intelligent Polymer Research Institute**

Flexible Graphene based Materials for Energy Storage

Kewei Shu

This thesis is presented as part of the requirement for the

Award of the Degree of

Doctor of Philosophy

The University of Wollongong

March 2016

Certification of Originality

I, Kewei Shu, declare that this thesis, submitted in fulfilment of the requirements for the award of Doctor of Philosophy, is my original work unless otherwise referenced and acknowledged. This thesis, which was carried out under the supervision of Prof. Gordon G. Wallace and Dr. Caiyun Wang in the Intelligent Polymer Research Institute at the University of Wollongong, has not been submitted for qualifications at any other academic institution.

Kewei Shu

Date: 10/10/2016

Acknowledgements

First of all, I would like to avail myself of this opportunity to express my great thanks to my supervisors Professor Gordon Wallace and Dr. Caiyun Wang, who provided expert guidance, direction, encouragement and support. To Professor Gordon Wallace, it is great pleasure for me to work in such a brilliant research group under your supervision. Thank you for the research experiences you shared, the research environment you provided, also the big picture of my research field you depicted. To Dr. Caiyun Wang, any achievements I've attained during my PhD study would have been impossible without your meticulous guidance and help in the project design, experimental works and scientific writing. The professional knowledge and research skills I've learned from my supervisors, will offer great benefits to my future academic career.

I've had pleasant experiences with my collaborators Dr. Sureyya Saricilar, Mr. Chen Zhao, Dr. Sha Li, Dr. Yang Yang, Dr. Sanjeev Gambhir, Dr. Zhu-yin Sui, Dr. Jie Ding and Dr. Gangrou Peng. I thank them for their help with various technical aspects, and for bringing me into contact with many fascinating projects. I am sincerely grateful to the members of IPRI and ACES, including Mr. Tony Romeo, Dr. Patricia Hayes, Dr. Dongqi Shi, Dr. Meng Wang, Miss Tian Zheng, who give me technical support on microscope and instrumental analysis. Also, I would like to express my sincere gratitude to Assoc. Prof. Chee O. Too for his critical proof-reading on my publications and thesis.

To my friends in IPRI, Dr. Lei Tong, Dr. Long Zhao, Dr. Hai Xin, Xiaoteng Jia, Yu Ge, Qi Gu, Yuqing Liu, Guanran Zhang, thank you for all the wonderful times we spent and all the encouragement you gave. I also want to give special thanks to my

girlfriend Miss Qijie Wu, who accompanies me with understanding, unconditional support and love.

I would like to acknowledge the China Scholarship Council and University of Wollongong, for the scholarships they kindly provided.

Finally, I owe my achievements to my beloved parents. I thank them for giving me life, raising me up and teaching me about life. Thanks for their endless love and support.

Abstract

With the rapid development of portable electronic devices, increasing interest is being aroused in flexible energy storage units with high energy and power density. The electrodes used in such energy systems should combine superior electrochemical properties with high mechanical flexibility. Graphene based free-standing thin films or papers are promising binder-free flexible electrodes. The main drawback of graphene paper electrode is the deterioration of electrochemical performance caused by the restacking of graphene sheets during the fabrication process. Fabricating 3D structured graphene macro-assemblies can address this issue, but compromise mechanical strength and low areal capacitance.

This thesis considers the development of non-stacked graphene paper with good flexibility, in which the graphene sheets are highly separated. The flexible porous structured graphene paper was prepared from graphene cryogel, which was formed by freeze-drying a solution containing chemically reduced graphene and graphene oxide (CRG/GO). At a current density of 2000 mA g^{-1} , it exhibited a discharge capacity higher than 400 mAh g^{-1} , in sharp contrast to that 229 mAh g^{-1} at 50 mA g^{-1} delivered by conventional graphene papers. The CRG/GO ratio in the precursor solution determined the mechanical properties of this cryogel paper. It can achieve a Young's modulus nearly 9 times greater than an equivalent paper made from pure GO when the CRG/GO mass ratio was 2:1.

With an improved strategy, by directly freeze-drying graphene wet gel obtained from filtration, graphene paper with continuous pores was prepared without mechanical pressing. This porous graphene (PG) paper showed high discharge capacity and excellent rate capability in lithium ion batteries. The discharge capacity can reach 420

mAh g⁻¹ at a current density of 2000 mA g⁻¹. A flexible all-solid-state supercapacitor based on such PG papers exhibited a specific capacitance of 137 F g⁻¹ at 1 A g⁻¹.

Due to low areal loading mass, graphene paper with porous structure delivers a low areal capacitance. We developed a free-standing chemically reduced graphene (CRG)-polypyrrole (PPy) hybrid paper with enhanced areal capacitance, via electropolymerization of pyrrole on a paper-like graphene gel. A high areal mass loading of 2.7 mg cm⁻² can be obtained. It afforded a greatly enhanced areal capacitance of 440 mF cm⁻² at 0.5 A g⁻¹, in sharp contrast to that 186 mF cm⁻² from flexible graphene paper. It is also much higher than the previously reported 151~198.5 mF cm⁻² for flexible polypyrrole-graphene papers/films.

The most frequently used graphene preparation approach, exfoliation of graphite oxide, involves a time-consuming procedure and the resultant defected graphene structure. As an alternative, graphene obtained via surfactant assisted liquid phase exfoliation from expanded graphite produces less defects in the graphene and avoids involving complicated post-treatment. In this work, graphene obtained from direct exfoliation of expanded graphite was used to fabricate flexible film electrodes incorporated with polypyrrole fibre (PPyF). PPy fibre was synthesized in the presence of the surfactant that served as dopant and template. Such composite film delivered a capacitance of up to 161 F g⁻¹ at 0.5 A g⁻¹, and 80 % of this value can be retained even at a higher current density of 8 A g⁻¹.

Table of Contents

Acknowledgements	i
Abstract	1
Table of Contents	3
List of Abbreviations	8
List of Figures	10
List of Tables	19
Publications	20
1 Introduction	23
1.1 Overview of Flexible Energy Storage	23
1.2 Brief Introduction of Lithium-ion Batteries and Supercapacitors	26
1.2.1 Lithium-ion batteries and supercapacitors.....	27
1.2.1.1 Lithium-ion batteries (LIBs).....	27
1.2.1.2 Supercapacitors (SCs)	29
1.2.1.3 Comparison between LIBs and SCs	31
1.2.2 Evaluation techniques of LIBs and SCs	33
1.2.3 Electrode materials for lithium-ion batteries.....	37
1.2.4 Electrode materials for supercapacitors.....	40
1.3 Graphene for Energy Storage Application	43
1.3.1 Graphene and its preparation.....	44
1.3.2 Graphene based materials for energy storage.....	50
1.4 Graphene Based Flexible Electrodes	54
1.4.1 Flexible graphene electrodes with mechanical support.....	55

1.4.2	Free-standing graphene based flexible electrodes	58
1.4.2.1	Flexible graphene based paper/film electrodes for LIBs	58
1.4.2.2	Flexible graphene based paper/film electrodes for SCs	61
1.4.2.3	Three dimensional (3D) graphene based flexible electrodes.....	63
1.4.2.4	Flexible graphene composite electrodes	67
1.5	Thesis Objective	73
1.6	References	76
2	Experimental.....	87
2.1	List of Chemical Reagents and Materials.....	87
2.2	General Synthesis and Device Assembly	88
2.2.1	Synthesis of graphene oxide	88
2.2.2	Preparation of stable aqueous CRG solution.....	89
2.2.3	Fabrication of graphene paper/wet gel	90
2.2.4	Electrochemical deposition of polypyrrole.....	91
2.2.5	Lithium-ion coin cell and supercapacitor assembly	91
2.3	Physicochemical Properties Characterization Techniques	93
2.3.1	Scanning electron microscope	93
2.3.2	Atomic force microscopy	94
2.3.3	X-ray photoelectron spectroscopy	95
2.3.4	X-ray diffraction	95
2.3.5	Raman spectroscopy	96
2.3.6	Thermogravimetric analysis (TGA)	97
2.3.7	Zeta potential measurement.....	97
2.3.8	Ultraviolet-visible spectroscopy	98
2.3.9	Conductivity measurement.....	99

2.4	Electrochemical Properties Characterization Techniques	99
2.4.1	Cyclic voltammetry	99
2.4.2	Galvanostatic charge/discharge	101
2.4.3	Electrochemical impedance spectroscopy	101
2.5	References	102
3 Graphene Cryogel Paper with Enhanced Mechanical Strength for High Performance Lithium-ion Battery.		103
3.1	Introduction	103
3.2	Experimental Specific to This Chapter.....	105
3.2.1	Synthesis of graphene oxide (GO) and CRG dispersion	105
3.2.2	Fabrication of Graphene Cryogel Paper and Coin Cell Assembly	106
Table 3.1 Recipe for precursor solution with different CRG/GO ratio		106
3.2.3	Characterization techniques.....	107
3.3	Results and Discussion	107
3.3.1	Characterization of chemically reduced graphene dispersion	107
3.3.2	Characterization of graphene cryogel paper	109
3.3.3	Electrochemical performances as a LIB anode	114
3.4	Conclusion.....	120
3.5	References	122
4 Flexible Free-standing Graphene Paper with Interconnected Porous Structure for Energy Storage		124
4.1	Introduction	124
4.2	Experimental Specific to This Chapter.....	126
4.2.1	Fabrication of porous graphene paper	126
4.2.2	Device assembly	126

4.3	Results and Discussion	127
4.3.1	Characterization of graphene oxide	127
4.3.2	Physiochemical characterization of porous graphene paper.....	128
4.3.3	Electrochemical performance as a lithium-ion battery anode	132
4.3.4	Graphene paper based flexible all-solid-state supercapacitor	136
4.4	Conclusion.....	142
4.5	References	144
5 Free-standing Graphene-Polypyrrole Hybrid Paper via Electropolymerization		
with an Enhanced Areal Capacitance.....		148
5.1	Introduction	148
5.2	Experimental Specific to This Chapter.....	150
5.2.1	Preparation of CRG-PPy paper.....	150
5.2.2	Assembly of device and characterization	150
5.3	Results and Discussion	151
5.3.1	Preparation of CRG-PPy paper.....	151
5.3.2	Physicochemical characterization of CRG-PPy paper	152
5.3.3	Electrochemical performance for supercapacitor	157
5.4	Conclusion.....	164
5.5	References	166
6 Fabrication of Flexible Graphene/polypyrrole Film Directly from the Exfoliated		
Expanded Graphite and in-situ formed polypyrrole nanofibres for Supercapacitor		
Application		170
6.1	Introduction	170
6.2	Experimental Specific to This Chapter.....	172
6.2.1	Exfoliation of worm-like expanded graphite.....	172

6.2.2	Preparation of DEG-PPyF film.....	172
6.3	Results and Discussion	173
6.3.1	Exfoliation of graphite.....	173
6.3.2	Physicochemical characterization of DEG-PPyF film	177
6.3.3	Electrochemical performance of DEG-PPyF film.....	181
6.4	Conclusion.....	187
6.5	References	189
7	Conclusion and Outlook.....	193

List of Abbreviations

A	ampere
AFM	atomic force microscopy
cm	centimetre
CPs	conducting polymers
CRG	chemically reduced graphene
CTAB	cetyl trimethylammonium bromide
CV	cyclic voltammetry
DEG	directly exfoliated graphene
EDL	electric double layer
EDX	energy dispersive X-ray
EIS	electrochemical impedance spectroscopy
EPG	expanded graphite
ESR	equivalent series resistance
F	faraday
g	gram
GO	graphene oxide
h	hour
LIBs	lithium-ion batteries
M	moles per litre
mAh	miliampere-hour
min	minute
nm	nanometre
PEDOT	poly(3,4-ethylenedioxythiophene)

PG	porous graphene
PPy	polypyrrole
PPyF	polypyrrole nanofibre
pTS	p-toluenesulfonate
PVA	poly(vinyl alcohol)
rGO	reduced graphene oxide
S	siemens
SCs	supercapacitors
SEM	scanning electron microscopy
TED	transmitted electron detection
TGA	thermo-gravimetric analysis
TMOs	transition metal oxides
V	volt
XPS	X-ray photoelectron spectroscopy
XRD	X-ray diffraction
μ	micro
Ω	ohm

List of Figures

Figure 1.1 Some commercially available or prototype flexible electronics: (A) LG bendable smartphone [5]; (B) Plastic Logic’s flexible AMOLED display [6]; (C) Ralph Lauren’s “smart polo shirt” [7]; (D) PowerFilm Solar Rollable Solar Panels [8], and (E) LG e-ink flexible display [9].	23
Figure 1.2 Schematic of a flat type (A), and fibre type (B) flexible power source [15].	25
Figure 1.3 Schematic illustration of a LIB cell [20].	28
Figure 1.4 Schematic illustration of a supercapacitor [23].	30
Figure 1.5 Ragone chart showing power density vs. energy density of various energy storage devices [24].	32
Figure 1.6 Stage forming process during lithium intercalation between graphene layers in a lithium-ion battery [34].	39
Figure 1.7 Lithium storage mechanism of hard carbon and penetration of electrolyte in pores [31].	40
Figure 1.8 (a) Dispersions of graphite flakes in NMP, at a range of concentrations ranging from 6 mg ml ⁻¹ (A) to 4 mg ml ⁻¹ (E) after centrifugation. (b) Bright-field TEM images of monolayer graphene flakes deposited from NMP. (c) Histogram of the number of visual observations of flakes as a function of the number of monolayers per flake for NMP dispersions [50].	46
Figure 1.9 (A) Schematic procedure of exfoliation of graphite with gradually added surfactant; (B) TEM image of graphene; (C) Image of a highly concentrated graphene suspension [70].	48
Figure 1.10 A proposed schematic of graphene oxide structure [73].	49

Figure 1.11 (a) An SEM image of aggregated reduced GO sheets; (b) A platelet having an upper bound thickness at a fold of ~ 2 nm; (c) AFM image of exfoliated GO sheets with three height profiles acquired at different locations [31]..... 50

Figure 1.12 (a) Irreversible Li Storage at the Interface between the Graphene Nanosheets and Electrolyte; (b) Reversible Li Storage at Edge Sites and Internal Defects (Vacancies etc.) of Nanodomains Embedded in Graphene Nanosheets; (c) Reversible Li Storage between (002) Planes [81]. 51

Figure 1.13 Graphene for batteries. (A) Relationship between the d-spacing and the charge capacity of graphene nanosheet (GNS) families and graphite; (B) Cross-sectional TEM images of GNS families with almost the same numbers (5–6) of graphene stacking layers for (a) GNS, (b) GNS + CNT, and (c) GNS + C60 [83].52

Figure 1.14 (a) SEM image of CMG particle surface, (b) TEM image showing individual graphene sheets extending from CMG particle surface, (c) low and high (inset) magnification SEM images of CMG particle electrode surface, and (d) schematic of test cell assembly [88]..... 53

Figure 1.15 (A) A schematic to show the preparation procedure of KOH activated microwave exfoliated GO (a-MEGO); (B) Low-magnification SEM image of a-MEGO; (C) High-resolution SEM image of a-MEGO that demonstrates the porous morphology; (D) ADF-STEM image of the same area as (C); (E) High-resolution phase contrast electron micrograph of the thin edge of a-MEGO chunk; (F) CV curves at different scan rates; (G) Galvanostatic charge/discharge curves under different constant currents [90]. 54

Figure 1.16 SEM images of the filter paper or graphene–cellulose paper surfaces with different graphene nanosheet loading amounts. (A) 0 wt% (pristine filter

paper), (B) 2.3 wt%, and (C) 7.5 wt%. (D) Illustration of the structural evolution of graphene–cellulose paper as the graphene nanosheets loading increases [96].	56
Figure 1.17 (a) A schematic diagram of the structure of an assembled symmetric supercapacitor, (b) photo of the assembled supercapacitor, (c) CV curves of the assembled supercapacitor at various scan rates in 6 M KOH solution, and (d) its specific capacitances at various scan rates [94].	57
Figure 1.18 (A) Photograph of two pieces of free-standing graphene paper fabricated by vacuum filtration of chemically prepared graphene dispersions, followed by air drying and peeling off the membrane. Front and back surfaces are shown. (B) Side-view SEM images of a ca. 6 μm thick sample. (C) Charge/discharge profiles and (D) cycle performance of graphene paper at a current density of 50 mA g^{-1} [99, 100].	60
Figure 1.19 Schematic drawing (not to scale) of the introduction of in-plane pores into chemically exfoliated graphene oxide (GO) and the subsequent filtration into a holey graphene oxide paper (HGO) [102].	60
Figure 1.20 (A) A photo showing the flexibility of an electrolyte-mediated chemically converted graphene (EM-CCG) film. (B, C) SEM cross-sectional images of EM-CCG films with mass loadings of 0.42 and 1.33 mg cm^{-3} . (D) Volumetric capacitance and (E) energy density as a function of the areal mass loading of an EM-CCG film (1.25 g cm^{-3}) and a dried CCG film (1.49 g cm^{-3}) at a current density of 0.1 A g^{-1} [104].	62
Figure 1.21 Illustration of the formation process of graphene paper and its performance as a lithium-ion battery or supercapacitor electrode. Reproduced with permission [106].	63

Figure 1.22 (A) Schematic drawings illustrating the process to prepare RGO foams. (B and C) Cross-sectional SEM images of RGO foams. (D and E) Schematic diagram and optical image of the flexible RGO foam supercapacitor. (F) CV curves of the RGO foam supercapacitor before bending and while bent [108].	64
Figure 1.23 (a-c) Schematic illustration of the interfacial gelation mechanism; (d) Graphene gelation procedure; (e-f) SEM images of freeze-dried aerogels prepared at different conditions [109].	65
Figure 1.24 (a) An illustration of the fabrication of ‘bubble’ graphene paper and photos of (b) as-prepared GO/PMMA paper, (c) “bubble” graphene paper [111].	67
Figure 1.25 Schematic of Li storage mechanism of graphene-MnO ₂ NT film as a LIB anode [117].	69
Figure 1.26 (a) A schematic diagram showing the formation of graphene/VNW composite; (b) SEM micrographs of the surface and cross-section of the graphene paper (inset); (c) Surface morphology of graphene/VNW composite paper. Inset shows a digital image and cross-sectional SEM image of the flexible freestanding graphene/VNW paper [119].	70
Figure 1.27 (a) Diagram of the apparatus used to deposit PPy on graphene paper and electrochemical testing. (b) Electrodeposition potential waveform used in the deposition. (c) Photographs showing the flexibility of graphene-PPy films [120].	72
Figure 2.1 Schematic of a filtration set for making graphene paper/wet gel.....	90
Figure 2.2 A three-electrode cell setup for electropolymerization.....	91
Figure 2.3 Lithium-ion coin cell configuration.	92
Figure 2.4 Configuration of Swagelok [®] -type testing cell for supercapacitor.	92
Figure 2.5 Illustration of a scanning electron microscope [8].....	93

Figure 2.6 Diagram of the basic principle of an AFM [9].....	94
Figure 2.7 Schematic of XPS physics [10].....	95
Figure 2.8 Representation of the X-ray diffraction principle.	96
Figure 2.9 Energy-level diagram showing the states involved in Raman signals [11].	97
Figure 2.10 Schematic of a four-point resistance measurement [12].....	99
Figure 2.11 A classical triangular waveform used in cyclic voltammetry.	100
Figure 3.1 (a) UV-vis spectra of GO and CRG dispersion; (b) AFM images of CRG.	108
Figure 3.2 SEM images of (a) rGO-CRG-0.5, (b) rGO-CRG-2, (c) rGO-CRG-5 and (d) rGO cryogels. Photograph of (e) rGO-CRG-0.5 cryogel and (f) rGO-CRG-0.5 paper.	110
Figure 3.3 SEM images of the surface morphology and cross section of rGO-CRG-0.5 paper (a, b) and CRG paper by filtration (c, d). (f inset: cross section of CRG by filtration at higher magnification, scale bar, 1 μm)	111
Figure 3.4 (a) XRD patterns of GO and hybrid papers; (b) TGA curves of graphene papers with different CRG/GO ratio.	113
Figure 3.5 Stress-strain curves of graphene papers with different CRG/GO ratio.	114
Figure 3.6 The first and second discharge/charge curves of graphene papers: (a) rGO, (b) GO-CRG-5 (c), GO-CRG-2, (d) GO-CRG-0.5 and (e) CRG.	116
Figure 3.7 Cyclic voltammograms obtained for graphene papers at a scan rate of 0.1 mV s^{-1} : (a) rGO, (b) GO-CRG-5, (c) GO-CRG-2, (d) GO-CRG-0.5 and (e) CRG.	117

Figure 3.8 Charge/discharge curves of graphene papers at different current densities: (a) rGO, (b) GO-CRG-0.5. Capacity versus cycle number at a current density of 2000 mA g ⁻¹ : (c) rGO, (d) GO-CRG-0.5.....	119
Figure 3.9 Nyquist plots of graphene cryogel papers and the CRG papers.....	120
Figure 4.1 Schematic procedure to fabricate a flexible all solid-state supercapacitor.....	127
Figure 4.2 (a) XPS spectrum of graphene oxide; (b) AFM image and height profile of graphene oxide.	128
Figure 4.3 SEM images of the cross-section of (a) PG paper, (b) G-87 paper and (c) air dried graphene paper; Photograph of PG paper (d). (Figure 4.3a inset: SEM image of cycle PG paper.)	130
Figure 4.4 XRD patterns (a), Raman spectra (b), and TGA curves (c) of GO and PG papers [Figure 4a inset: expanded peak view for PG paper (5-40°)]......	132
Figure 4.5 First and second charge/discharge curves of PG paper (a), G-87 papers (c) and G-air paper (d); (b) Cyclic voltammograms obtained for PG paper at a scan rate of 0.1 mV s ⁻¹	134
Figure 4.6 Charge/discharge curves of PG paper (a) and G-87 paper (b) at different current densities.....	135
Figure 4.7 (a) Capacity versus cycle number for PG paper at 2000 mA g ⁻¹ . (b) Nyquist plots of PG paper and the graphene paper (filtration).....	136
Figure 4.8 Cyclic voltammograms of PG paper (a), G-87 paper (b), and G-air paper (c) at different scan rates.	137
Figure 4.9 (a) Charge/discharge curves of PG paper (solid line), G-87 paper (dotted line) and G-air paper (dash line) based flexible supercapacitors; (b) CV curves of the bent and unbent device at a scan rate of 10 mV s ⁻¹ ; (c) Photograph of the bent	

flexible PG paper based supercapacitor; (d) Cycle stability of the PG paper device at a current density of 1 A g ⁻¹	139
Figure 4.10 Nyquist plots (a) (scatter: experimental plots, line: fitting plots), and capacitance versus frequency (b) of PG, G-87 and G-air paper. (a inset: equivalent circuit model).....	141
Figure 4.11 Ragone plot of PG papers in comparison with the reported graphene-based all-solid-state supercapacitors.	142
Figure 5.1 Schematic procedure to fabricate a CRG-PPy paper that includes the following steps (a): formation of wet CRG paper via filtration, soaking the wet paper in pyrrole monomer solution, PPy electropolymerization and drying. Digital image of a CRG-PPy40 paper (b).....	151
Figure 5.2 SEM images of the cross-section of a neat CRG (a), CRG-PPy20 (b), CRG-PPy40 (c) and CRG-PPy60 paper (d); Surface morphology and cross-sectional view of a neat CRG (e, g) and CRG-PPy40 paper (f, h) at higher magnification.....	153
Figure 5.3 Elemental analysis of a neat CRG (a, surface; e, cross-section) and CRG-PPy40 paper (c, surface; g, cross-section). Elemental mapping of the surface of neat CRG (b), CRG-PPy40 (d), and the cross-section of CRG (f) and CRG-PPy40 (h).	155
Figure 5.4 Raman spectra of a neat CRG or CRG-PPy40 paper (a) and the expanded view over 500~1200 cm ⁻¹ (b); XPS spectra of C _{1s} in neat CRG (c), C _{1s} in CRG-PPy (d), N _{1s} in CRG-PPy40 (e) and S _{2p} in CRG-PPy (f). (black line, experimental data; colour line: fitting line)	157
Figure 5.5 Cyclic voltammograms of a CRG (a), or CRG-PPy60 (b) paper in 1 M H ₂ SO ₄ between -0.5 to 0.5 V (vs. Ag/AgCl) at scan rates of 20, 50, 100 mV s ⁻¹ .	158

Figure 5.6 Cyclic voltammograms of a CRG (a), CRG-PPy20 (b), CRG-PPy40 (c) or CRG-PPy60 (d) paper in 1 M H ₂ SO ₄ at a scan rate 20, 50, 100 mV s ⁻¹	159
Figure 5.7 Electrochemical performance of the symmetric supercapacitors using CRG, CRG-PPy 20, CRG-PPy40 or CRG-PPy60 paper electrodes in 1M H ₂ SO ₄ . (a-d) Charge/discharge curves; (e) Areal capacitance versus current densities; (f) Cycle stability at a current density of 2 A g ⁻¹	161
Figure 5.8 Ragone plot of CRG-PPy hybrid papers in comparison with the reported graphene-based paper materials.....	163
Figure 5.9 Nyquist plots (a) (scatter: experimental plots, line: fitting plots), and frequency response (b) of neat CRG or CRG-PPy papers based supercapacitor. (a inset: equivalent circuit model)	164
Figure 6.1 SEM images of worm-like expanded graphite (a-b), TED-SEM image of DEG (c) and AFM image (d) and height profile of DEG (e).	174
Figure 6.2 (a) Raman spectra of CCG, DEG and WG. (b) 2D peak of CCG, DEG and WG.....	175
Figure 6.3 XPS spectra of WG C1s (a), WG O1s (b), DEG C1s (c), DEG O1s (d).	177
Figure 6.4 Digital image of DEG-PPyF1 flexible film (a), and film with a DEG:pyrrole ratio of 1:2 (b).	178
Figure 6.5 Cross-sectional view of PPyF film (a, b), DEG-PPyF1 film (d,e), DEG-PPyF2 film (g, h) and DEG film (j, k, on filter membrane); and surface morphology of PPyF film (c), DEG-PPyF1 film (f) and DEG-PPyF2 film (i)	179
Figure 6.6 Raman spectra of PPyF (a), DEG (b), DEG-PPyF1 (c), DEG-PPyF2 (d) and 2D peak of DEG, DEG-PPyF1 and DEG-PPyF2 (e). TGA curves of PPyF,	

DEG, DEG-PPyF1 and DEG-PPyF2 film (f). (a, c, d inset: raman spectra between 500-1200 cm^{-1}).	181
Figure 6.7 CV curves of PPyF (a), DEG (b), DEG-PPyF1 (c) and DEG-PPyF2 (d) film electrodes in 1 M Li_2SO_4	183
Figure 6.8 Charge/discharge curves of PPyF (a), DEG (b), DEG-PPyF1 (c) and DEG-PPyF2 film (d) electrode in 1 M Li_2SO_4	184
Figure 6.9 Rate performance (a), cycle stability (b), Nyquist plots (c) and frequency response (d) of DEG, PPyF and DEG-PPyF film electrodes. (c inset: proposed equivalent circuit)	187

List of Tables

Table 1.1 Some key features comparison between a capacitor, supercapacitor and lithium-ion battery [23-25].	33
Table 1.2 Theoretical and experimental specific capacitances of common conducting polymers [44-49].	42
Table 3.1 Recipe for precursor solution with different CRG/GO ratio	106

Publications

1. **Shu, K.**; Wang, C.; Zhao, C.; Ge, Y.; Wallace, G., A Free-standing Graphene-Polypyrrole Hybrid Paper via Electropolymerization with Enhanced Areal Capacitance. *Electrochimica Acta*, **2016**, 212, 561-571.
2. **Shu, K.**; Wang, C.; Li, S.; Zhao, C.; Yang, Y.; Liu, H.; Wallace, G., Flexible free-standing graphene paper with interconnected porous structure for energy storage. *Journal of Materials Chemistry A* **2015**, 3 (8), 4428-4434.
3. **Shu, K.**; Wang, C.; Wang, M.; Zhao, C.; Wallace, G. G., Graphene cryogel papers with enhanced mechanical strength for high performance lithium battery anodes. *Journal of Materials Chemistry A* **2014**, 2 (5), 1325-1331.
4. Liu, Y.; Weng, B.; Xu, Q.; Hou, Y.; Zhao, C.; Beirne, S.; **Shu, K.**; Jalili, R.; Wallace, G. G.; Razal, J. M.; Chen, J., Facile fabrication of flexible micro-supercapacitor with high energy density. *Advanced Materials Technologies* **2016**, Accepted.
5. Yu, C.; Wang, C.; Liu, X.; Jia, X.; Naficy, Sina.; **Shu, K.**; Forsyth, Maria; Wallace, G. G., A Cytocompatible Robust Hybrid Conducting Polymer Hydrogel for Use in a Magnesium Battery. *Advanced Materials* **2016**, Accepted.
6. Ge, Y.; Wang, C.; **Shu, K.**; Zhao, C.; Jia, X.; Gambhir, S.; Wallace, G. G., A facile approach for fabrication of mechanically strong graphene/polypyrrole films with large areal capacitance for supercapacitor applications. *RSC Advances* **2015**, 5 (124), 102643-102651.
7. Ding, J.; Peng, G.; **Shu, K.**; Wang, C.; Tian, T.; Yang, W.; Zhang, Y.; Wallace, G. G.; Li, W., Novel reversible and switchable electrolytes based on magnetorheology. *Scientific Reports* **2015**, 5, Article number: 15663.

8. Zhao, C.; **Shu, K.**; Wang, C.; Gambhir, S.; Wallace, G. G., Reduced graphene oxide and polypyrrole/reduced graphene oxide composite coated stretchable fabric electrodes for supercapacitor application. *Electrochimica Acta* **2015**, 172, 12-19.
9. Sui, Z.-Y.; Wang, C.; Yang, Q.-S.; **Shu, K.**; Liu, Y.-W.; Han, B.-H.; Wallace, G. G., A highly nitrogen-doped porous graphene - an anode material for lithium ion batteries. *Journal of Materials Chemistry A* **2015**, 3 (35), 18229-18237.
10. Sui, Z.-Y.; Wang, C.; **Shu, K.**; Yang, Q.-S.; Ge, Y.; Wallace, G. G.; Han, B.-H., Manganese dioxide-anchored three-dimensional nitrogen-doped graphene hybrid aerogels as excellent anode materials for lithium ion batteries. *Journal of Materials Chemistry A* **2015**, 3 (19), 10403-10412.
11. Li, S.; Zhao, C.; **Shu, K.**; Wang, C.; Guo, Z.; Wallace, G. G.; Liu, H., Mechanically strong high performance layered polypyrrole nano fibre/graphene film for flexible solid state supercapacitor. *Carbon* **2014**, 79, 554-562.
12. Li, S.; **Shu, K.**; Zhao, C.; Wang, C.; Guo, Z.; Wallace, G.; Liu, H. K., One-Step Synthesis of Graphene/Polypyrrole Nanofiber Composites as Cathode Material for a Biocompatible Zinc/Polymer Battery. *ACS Applied Materials & Interfaces* **2014**, 6 (19), 16679-16686.
13. Zhao, C.; Wang, C.; Gorkin Iii, R.; Beirne, S.; **Shu, K.**; Wallace, G. G., Three dimensional (3D) printed electrodes for interdigitated supercapacitors. *Electrochemistry Communications* **2014**, 41, 20-23.
14. Zhao, C.; Wang, C.; Yue, Z.; **Shu, K.**; Wallace, G. G., Intrinsically Stretchable Supercapacitors Composed of Polypyrrole Electrodes and Highly Stretchable Gel Electrolyte. *ACS Applied Materials & Interfaces* **2013**, 5 (18), 9008-9014.

15. Saricilar, S.; Antiohos, D.; **Shu, K.**; Whitten, P. G.; Wagner, K.; Wang, C.; Wallace, G. G., High strain stretchable solid electrolytes. *Electrochemistry Communications* **2013**, 32, 47-50.

1 Introduction

1.1 Overview of Flexible Energy Storage

Flexible electronic devices are devices that are bendable and deformable without a dramatic decrease in their performances. With the increasing demand of wearable sensors, flexible displays and implantable diagnostic devices, the research for flexible electronics has developed rapidly [1-4]. There have already been some commercially available or prototype flexible electronics such as e-ink screen, bendable smartphone and “smart polo shirt” (Figure 1.1). The development of rechargeable batteries or supercapacitors focuses on maximizing the charge storage and cycle stability. Those used to drive flexible electronics need to meet the requirements of flexibility, light weight, and high performance as well.

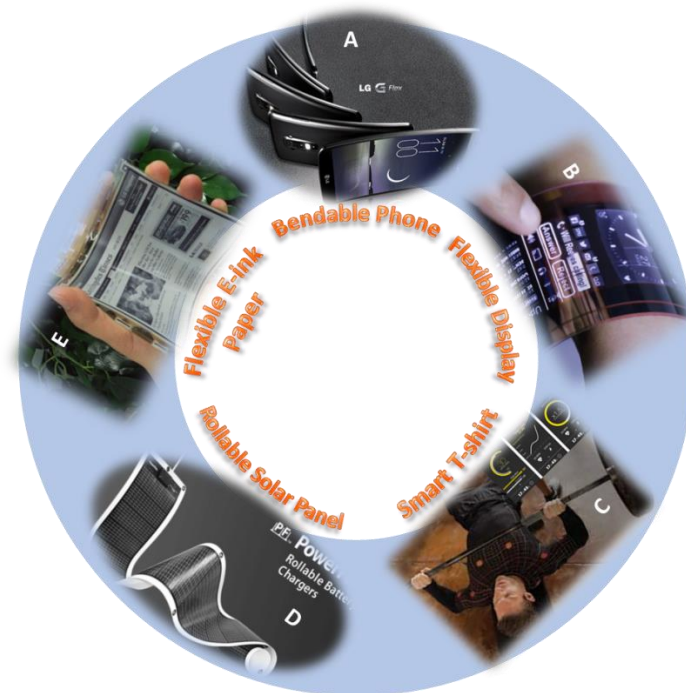


Figure 1.1 Some commercially available or prototype flexible electronics: (A) LG bendable smartphone [5]; (B) Plastic Logic’s flexible AMOLED display [6]; (C) Ralph

Lauren's "smart polo shirt" [7]; (D) PowerFilm Solar Rollable Solar Panels [8], and (E) LG e-ink flexible display [9].

Commonly used flexible energy storage devices include flexible lithium-ion batteries (LIBs) and supercapacitors (SCs). They can be assembled into flat type or fibre type for use (Figure 1.2). They all consist of three main components: electrodes, electrolyte and separator. Fibre batteries contain the same essential elements, yet are coaxially assembled. The wire-shaped designs make it easy to be integrated with or even woven into textiles. For flat type configuration, two flexible electrodes are separated by either separator or flexible electrolyte, and then packaged into soft materials [10]. The work in this thesis focuses on the latter type. The commonly used electrolytes for flexible energy storage devices are polymer-based solid state electrolytes, which consist of ionic conductor and high-molecular-weight polymer matrix. They can serve as separator as well, and permit the realization of flexible, compact solid-state energy storage devices.

To develop flexible energy storage, the key challenge is to design and develop flexible electrodes. Recently, tremendous research has been dedicated to the development of electrodes with not only large capacity/capacitance, high energy and power density, long cycle stability, but also good mechanical properties. These electrodes are required to retain their function during a small deformation.

There are two common strategies to develop flexible electrodes for flat type energy devices. One approach is to prepare electrodes with flexible mechanical support (substrate). Materials that can combine the properties of mechanical flexibility and electrochemical activity together are quite limited. Most active materials used in energy storage are in the form of powders. They are combined with polymer binders to be stuck

on the substrates for use. Researchers have attempted to address this issue by using flexible substrates. They can be obtained by integrating conventional active materials with flexible supports such as carbon-based papers, polymers, fabrics or even thin metal foils. Facile fabrication techniques include printing [11], coating [12], deposition [13] or spraying [14]. The use of flexible supports allows a wide variety of materials to be selected. However, this type of flexible electrodes has some disadvantages: dead volume, dead weight from the substrate, and the detachment between the materials and substrate caused by the deformation.

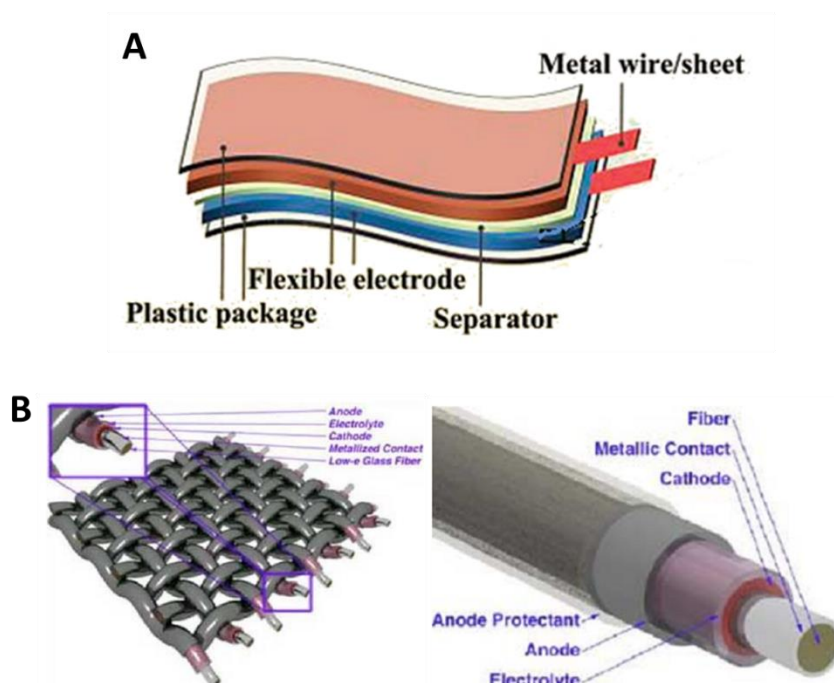


Figure 1.2 Schematic of a flat type (A), and fibre type (B) flexible power source [15].

An alternative approach is to fabricate intrinsically flexible electrodes that mainly focuses on carbon-based or conducting polymer-based materials. Owing to their high electrochemical activity, high mechanical flexibility, and ease of process, carbon-based materials are the most used materials for free-standing electrodes. They mainly include carbon nanotube (CNT) or graphene based materials. They can be fabricated simply

using the techniques of vacuum filtration, gelation or wet spinning from well-dispersed solutions [16].

Graphite is commercially used in LIBs as an anode material, and activated carbon is used in commercial SCs. Recent emerging nanocarbon material, graphene, has been considered as an alternative due to its fascinating physical and electronic properties derived from its unique nanostructures. The use of wet chemical method in graphene preparation allows mass production for large scale applications. The excellent mechanical properties of graphene single sheets and the strong intersheets interaction make it feasible to fabricate highly flexible free-standing graphene macro-assemblies electrodes.

Conducting polymers are another important materials family for use as free-standing electrodes due to their large theoretical capacitance/capacity, good conductivity, and facile synthesis [17-19]. Furthermore, the combination of conducting polymer and graphene materials in making flexible electrodes could take advantage of the large capacitance/capacity from conducting polymers, and high stability and flexibility from graphene. A synergistic effect can be derived resulting in improved electrochemical performances and enhanced mechanical properties.

1.2 Brief Introduction of Lithium-ion Batteries and Supercapacitors

Flexible LIBs/SCs have the same operating principle and evaluation methods as the conventional types. A brief introduction of common lithium-ion batteries and supercapacitors is given in this section. It includes their working principle, evaluation methods and the electrode materials selection.

1.2.1 Lithium-ion batteries and supercapacitors

1.2.1.1 Lithium-ion batteries (LIBs)

A battery is an energy storage device that can convert chemical energy into electrical energy through electrochemical reduction-oxidation (redox) reaction. Depending on their capability of being recharged, batteries can be classified as primary (non-rechargeable) or secondary (rechargeable) type. When an external current is applied, a secondary battery can be recharged, following the reversed electrochemical reaction occurred during discharge. The earliest secondary battery, lead-acid battery, was invented in 1859. The lead-acid battery with improved performance is still widely used in vehicles currently. Other types of rechargeable batteries such as silver-zinc, nickel-metal hydride, nickel-cadmium have been introduced into commercial use since the mid-20th century.

Lithium-ion batteries, with high energy density (100-265 Wh kg⁻¹) and long cycle life (>1000 cycles), are the predominant rechargeable batteries used in consumer electronics at present, since it was commercially released by Sony in 1991. A LIB contains a positive electrode (cathode), a negative electrode (anode), a porous membrane separating the electrodes, and electrolyte (Figure 1.3). The commonly used anode materials are carbonaceous materials on a copper current collector, and the cathode materials are lithium metal oxides (i.e. LiCoO₂, LiNiO₂, LiMn₂O₄, LiFePO₄, etc.) on an aluminium foil. The electrolyte is typically a lithium salt (i.e. LiPF₆, LiBF₄, LiClO₄, etc.) in organic solvents such as mixtures of organic carbonates, ethers or acetates. Thin microporous polyethylene or polypropylene films are used as the separator to isolate the cathode and anode.

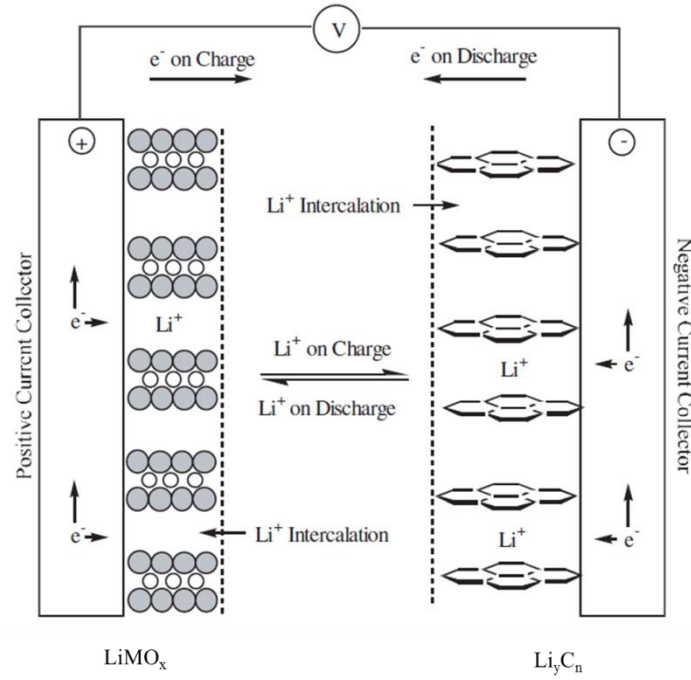
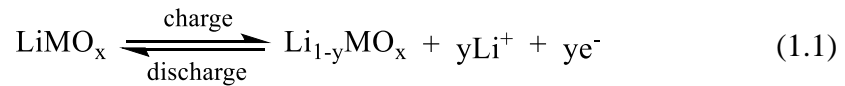
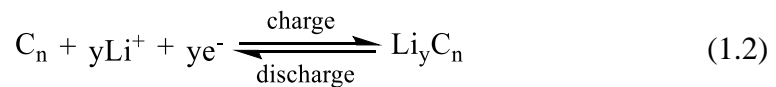


Figure 1.3 Schematic illustration of a LIB cell [20].

In LIBs, both the cathode and anode follow a lithium insertion (intercalation) mechanism; the lithium cations are inserted (defined as intercalation) and de-inserted (de-intercalation) during the charge/discharge process. The electrode materials, lithium metal oxide (cathode) or graphite (anode), can act as hosts to reversibly accommodate lithium ions, forming “sandwich” like structures [21]. The following half- reaction occurs on the cathode:



while on the anode, the half-reaction is:



where C represents carbon material and M indicates a metal.

While discharging, lithium ions are de-intercalated from the anode materials and inserted into the sites in the cathode materials, providing current to the external circuit. In the charging process, the external power sources force the current to pass from the cathode to the anode. Lithium ions then migrate to the anode and become embedded between layers of carbonaceous materials, which is known as intercalation.

1.2.1.2 Supercapacitors (SCs)

A capacitor is an electrical device to store energy temporarily. It contains two terminals connected to metal plates separated by a non-conductive substance (dielectric). Capacitors store the electrical energy statically by charge separation in the dielectric layer between parallel-plate electrodes when an external potential is applied. The charges will then rearrange to produce current when connected to an external load.

Supercapacitors (SCs), also named as ultracapacitor or electrochemical capacitors, are believed to be promising candidates to meet ever increasing demands of low-cost, sustainable and high performance energy storage systems. Similar to conventional capacitors, supercapacitors store energy by means of a charge separation between two oppositely charged electrodes, but with much larger capacitance. The energy density of a supercapacitor is 10 to 100 times higher, compared to that of conventional electrolytic capacitor. With high power density ($>10 \text{ kW kg}^{-1}$) and long cycle life ($>10,000$) [22], a supercapacitor has much faster charge/discharge rate and longer service life than that of rechargeable batteries.

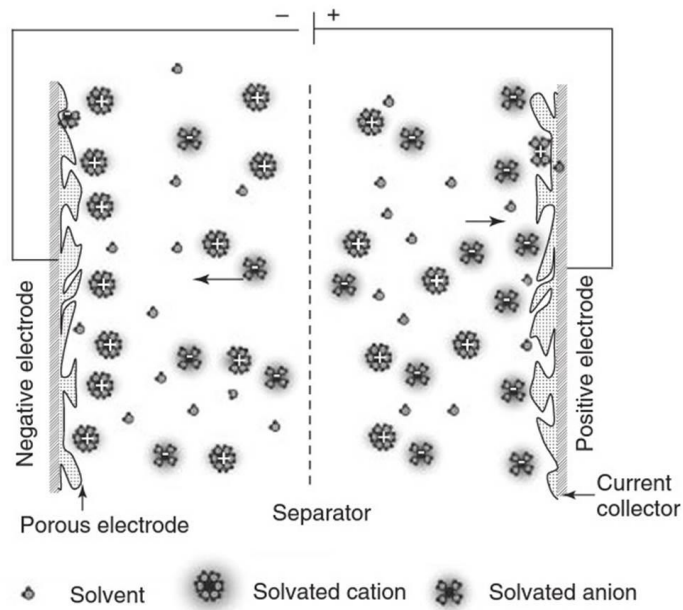


Figure 1.4 Schematic illustration of a supercapacitor [23].

A supercapacitor consists of two porous electrodes, an ion-permeable membrane separator and an electrolyte (Figure 1.4). Energy in a supercapacitor is stored via two different mechanisms: electrical double layer capacitance (EDLC) and pseudocapacitance. The EDLC originates from the accumulation of electrostatically charged layers at the electrolyte/electrode interface. It is influenced strongly by the surface area of the electrode materials. The EDL capacitance C (unit, F) can be calculated by the following Equation 1.3 [22]:

$$C = \frac{A\epsilon_r\epsilon_0}{d} \quad (1.3)$$

Where ϵ_r is the relative dielectric constant, ϵ_0 (F m^{-1}) is the relative dielectric constant in vacuum, A ($\text{m}^2 \text{g}^{-1}$) is the specific area of the electrode, and d (m) is the effective thickness of the electrical double layer.

The pseudocapacitance originates from the reversible, fast redox reactions that occur at or near the electrode-electrolyte interface. In a pseudocapacitor, non-Faradic

double layer charge accumulation and surface faradic processes occur simultaneously. A pseudocapacitor hence may combine the features of a supercapacitor and a battery. Commonly used pseudocapacitance materials include conducting polymers, transition metal oxides, heteroatoms (O, N, S, P, etc.) doped carbon materials [23].

1.2.1.3 Comparison between LIBs and SCs

Ragone plot is a chart to compare the power and energy capability of energy storage devices. The unit for those two axes is power density (W kg^{-1} , W L^{-1} , or W cm^{-1}) and energy density (Wh kg^{-1} , Wh L^{-1} , or Wh cm^{-1}). They are usually presented on a logarithmic scale. A simplified Ragone plot (Figure 1.5) is presented to compare the capacitors, supercapacitors and batteries. Among these three devices, batteries can deliver the highest specific energy, while supercapacitors are high-power systems. Some devices present the combined features of batteries and supercapacitors, as demonstrated with the overlapped areas. Thin film batteries exhibit specific power characteristics similar to those of supercapacitors. Meanwhile, asymmetric supercapacitors with the combination of a battery-type electrode and an EDL-type electrode, can deliver a specific energy close to batteries.

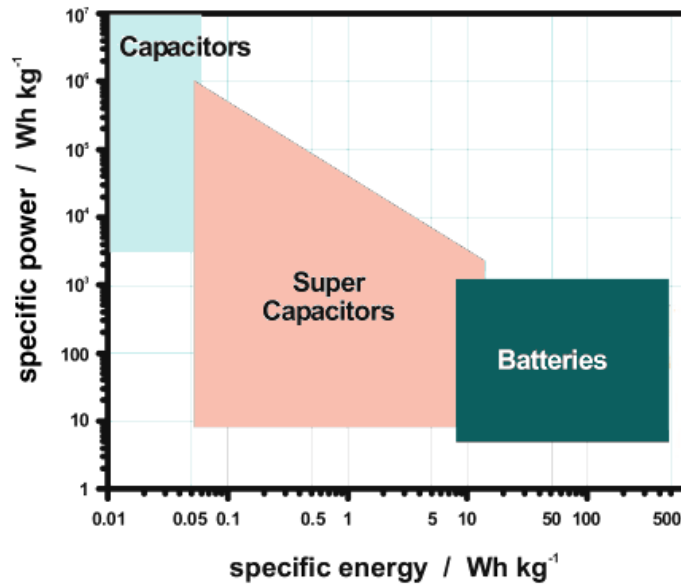


Figure 1.5 Ragone chart showing power density vs. energy density of various energy storage devices [24].

A comparison of key features from capacitors, supercapacitors and lithium ion batteries is shown in Table 1.1. Following the mechanism of surface charge separation and rearrangement on a conductive surface, a capacitor can undergo fast charge and discharge (millisecond to microsecond time scale), possess a nearly perfect coulombic efficiency and ultralong cycle life. However, it can only store limited energy, and suffers from severe self-discharge as well. These features cause the capacitor to be commonly used as power conditioning, signal coupling and substitutional short-term power sources. For the electric double layer or fast faradic reaction mechanism, a supercapacitor can provide much higher energy compared to a conventional capacitor, but takes a longer time to charge (still within second time scale). It can still endure a large number of charge-discharge cycles. The application of supercapacitors varies from buffer power to consumer electronic power sources, depending on its EDL or pseudocapacitance mechanism. Lithium-ion batteries can deliver quite large energy but

with lower charging speed. As the chemical reactions are not fully reversible, the cycle life of a lithium-ion battery is limited, much shorter than that of a capacitor or supercapacitor. Lithium-ion batteries can power a large variety of devices from consumer electronics to electric vehicles.

Table 1.1 Some key features comparison between a capacitor, supercapacitor and lithium-ion battery [23-25].

Function	Capacitor	Supercapacitor	Lithium- ion Battery
Charge time	10 ⁻⁶ -10 ⁻³ sec	1-10 sec	10-60 min
Energy density (Wh kg⁻¹)	< 0.1	1-10	100-265
Power density (kW kg⁻¹)	Up to 100	Up to 10	0.3-1.5
Cycle life	>500,000	>100,000	500-2,000
Self discharge time at room temperature	Short (days)	Middle-Long (weeks-month)	Long (several months)
Operation temperature (°C)	-40-125	-20-70	-20-60
Efficiency (%)	99	90-95	90

1.2.2 Evaluation techniques of LIBs and SCs

The capacity of a LIB is the quantity of the electric charge that can be delivered, which is based on the amount of active materials participating in the electrochemical reaction. It is defined in terms of coulombs or ampere-hours. The value of theoretical capacity C_0 (Ah g⁻¹) of the reactants is calculated using the following Equation 1.4:

$$C_0 = 26.8n \frac{m_0}{M} \quad (1.4)$$

C_0 is the theoretical capacity, m_0 (g) is the mass of the active material, M (g mol^{-1}) is the molar weight of the active material, n is the number of electrons involved in the reaction. The experimental capacity C (mAh g^{-1} or A g^{-1}) of a LIB is evaluated by galvanostatic charge/discharge test, and can be calculated using [t (s) is the discharge time, i (mA or A) is the applied current]:

$$C = it \quad (1.5)$$

“C” rate is a term used to indicate the discharge/charge current for a battery or an electrode. It can be expressed as:

$$I = M \times C \quad (1.6)$$

Where I (A) is the discharge current, M is the multiple or fraction of C , C is the numerical value of the theoretical capacity that can be fully discharged in 1 hour. For example, a 1 C rate for a 372 mAh battery is 372 mA. It can be calculated as follows:

$$M = \frac{I}{C} = \frac{0.372}{0.372} = 1 \quad (1.7)$$

The experimental energy density W (Wh g^{-1} or Wh kg^{-1}) and power density P (W g^{-1} or W kg^{-1}) equals to:

$$W = CV \quad P = IV \quad (1.8)$$

Here V (V) is the operation voltage (or average operation voltage).

The capacitance C describes the amount of electric charge stored in a capacitor. It can be characterized via three most commonly used techniques: cyclic voltammetry (CV), galvanostatic charge/discharge (C-DC) and electrochemical impedance spectroscopy (EIS). For CV testing, it involves applying a linearly varying electric potential between the reference and working electrodes. The speed of the potential change is named sweep rate or scan rate v (mV s^{-1} or V s^{-1}). The capacitance C (F g^{-1}) from CV method can be given by:

$$C = \frac{\Delta Q}{\Delta V} = \frac{\Delta Q}{v\Delta t} = \Delta i/v \quad (1.9)$$

$$\Delta i = \frac{1}{V_2 - V_1} \int_{V_1}^{V_2} i(V)dV \quad (1.10)$$

Where V_1 (V) and V_2 (V) are the switching potentials, and $\int_{V_1}^{V_2} i(V)dV$ is the voltammetric charge through the integration of the positive or negative sweep in a CV.

For charge-discharge test, a constant current is applied to charge the SCs to a desired voltage or discharged until the voltage decreased to 0.0 V. The value of the capacitance can be deduced according to the Equation 1.9:

$$C = \frac{i\Delta t}{\Delta V} \quad (1.11)$$

Where i (A) is the constant current, Δt (s) is the discharge time and ΔV (V) is the potential range.

The electrochemical impedance spectroscopy (EIS) test measures the impedance of a supercapacitor as a function of frequency by applying a low-amplitude alternating voltage under the applied potential. It is used to study charge transfer and storage mechanisms. An equivalent electrical circuit is proposed to simulate the electrochemical process that has occurred in a supercapacitor. It generally consists of the circuit elements such as resistance of electrolyte R_s , electric double layer capacitance from charge separation C_{dl} , bulk Faradic impedance of the active materials. The Faradic impedance can be divided into pseudocapacitance C_p and charge transfer resistance R_{ct} in the redox process. The capacitance measured by EIS is calculated by the imaginary part of the complex impedance Z_{Im} (Ω) as shown in the following Equation 1.12:

$$C = -\frac{1}{2\pi f Z_{Im}} \quad (1.12)$$

Where f (Hz) is normally the frequency at which the phase angle reaches -45° or at the lowest frequency applied [26]. An alternative calculation introduced by Simon et al. is [27]:

$$Z = \sqrt{Z_{Re}^2 + Z_{Im}^2} \quad (1.13)$$

$$C_{Re} = -\frac{Z_{Im}}{\omega|Z|^2} \quad C_{Im} = \frac{Z_{Re}}{\omega|Z|^2} \quad (1.14)$$

where $\omega = 2\pi f$ is angular velocity, Z_{Re} (Ω) is the real part of the complex impedance, Z is the overall complex impedance. The real capacitance C_{Re} (F) at the lowest applied frequency that can be used to represent the cell capacitance C .

Apart from the capacitance, energy and power density are another two important parameters to evaluate the performance of a SC. Power density is to describe the efficiency in energy delivery, while the energy density is to evaluate the electrical energy stored. They can be evaluated in terms of the unit mass, volume or area, as $W\text{ kg}^{-1}$, $W\text{ L}^{-1}$ or $W\text{ cm}^{-1}$ for power density; and $Wh\text{ kg}^{-1}$, $Wh\text{ L}^{-1}$ or $Wh\text{ cm}^{-1}$ for energy density. They are calculated by (taking gravimetrically energy/power density for example):

$$E = \frac{1}{2} \frac{C \Delta V^2}{m} \quad (1.15)$$

$$P = \frac{\Delta V^2}{4mR_{ES}} \quad (1.16)$$

The R_{ES} (Ω) is the “equivalent series resistance” which can be calculated from the sharp voltage drop at the beginning of the discharge cycle; or directly obtained from the EIS test [27]. C ($F\text{ g}^{-1}$) is the capacitance, m (g) is the mass of the electrode, and ΔV (V) is the potential range.

1.2.3 Electrode materials for lithium-ion batteries

At present, lithiated metal oxides are utilized as the cathode material for commercial LIBs. Sony's first commercial LIB product used LiCoO_2 [28, 29]. Later less costly materials such as LiMn_2O_4 , LiFePO_4 and higher capacity materials $\text{LiNi}_{1-x}\text{Co}_x\text{O}_2$ have been developed. These commercially available materials can be divided into two types of structure. LiCoO_2 , LiNiO_2 and $\text{LiNi}_{1-x}\text{Co}_x\text{O}_2$, have layered structures, whereas LiMn_2O_4 have a three-dimensional "framework" structure. In the case of LiCoO_2 or LiNiO_2 , the cobalt/nickel atoms reside within oxygen octahedra, and lithium atoms are intercalated/de-intercalated in the space between oxygen layers. The LiMn_2O_4 have a framework or tunnelled structure based on $\lambda\text{-MnO}_2$. Lithium fills 1/8 of the tetrahedral sites within $\lambda\text{-MnO}_2$.

In the early stages of secondary lithium battery development, lithium metal was used as anode because of its high specific capacity. The safety issue/concern about lithium metal encouraged the development of lithium-intercalated carbon materials as anode materials. Petroleum coke-based carbon was firstly utilized as anode material in LIBs marketed by Sony, offering a good capacity of 180 mAh g^{-1} [20]. In the mid-1990s most Li-ion cells utilized electrodes employing graphitic carbon, in particular a mesocarbon microbead (MCMB) carbon. MCMB carbon offers a much higher specific capacity, 300 mAh g^{-1} [30]. Other graphitic carbons are also used, such as natural graphite that has afforded a capacity of 365 mAh g^{-1} [31]. In LIBs, graphitic carbon anode like MCMB and natural graphite can form LiC_6 structures (Equation 1.17), the layers of lithium ions and graphite are arranged one after another. The theoretical capacity of graphite can be calculated using Equation 1.18 as below [32, 33]:



$$C_{\text{graphite}} = 26.8 \times \frac{1}{72.06} \times 1000 \approx 372 \text{ (mAh g}^{-1}\text{)} \quad (1.18)$$

A single lithium ion layer is firstly formed at low lithium ion concentration, and then the lithium ions will not be intercalated into adjacent graphene layers. Those layers without lithium ions inserted are periodically arranged, and the lithium ion concentration in graphite increases. The number of unfilled graphene layers is reduced with more intercalated lithium ions [34]. The above gradual lithium ion intercalation process is known as “stage formation”, as illustrated in Figure 1.6. The stage index is used to describe the number of non-lithiated graphene layers between lithium layers. The voltage plateau in the discharge curve indicates the coexistence of two phases [35]. In practical terms, experimental charge-discharge curves have no obvious discontinuities between the two-phase regions because various types of over-potential result in the plateau sloping.

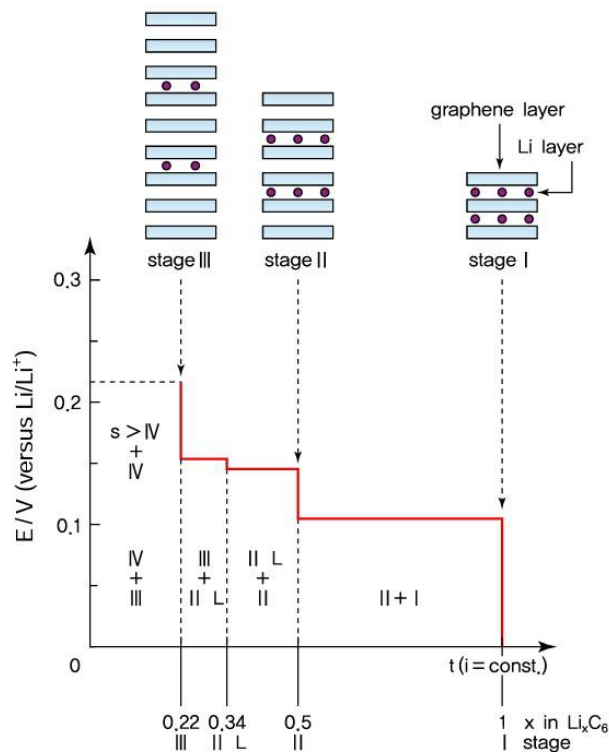


Figure 1.6 Stage forming process during lithium intercalation between graphene layers in a lithium-ion battery [34].

Compared with graphitic carbon, the amorphous non-graphitic “hard” carbon materials offer higher capacity, over 1000 mAh g^{-1} , but suffered from higher irreversible capacity, and higher voltage ($\sim 1 \text{ V}$) [36, 37]. Hard carbon materials do not have stacked graphene sheets and exhibit an amorphous structure with numerous micropores. The high capacity from hard carbon can be explained by the adsorption of lithium ions on the carbon layer surface and the formation of lithium clusters within micropores (Figure 1.7). The opening of micropores from heat treatment also allows the electrolyte to penetrate, which leads to irreversible capacity since lithium ions surrounded by electrolyte cannot be stored [31]. Another factor of irreversible capacity results from the reaction of lithium with surface functional groups or absorbed molecules [38].

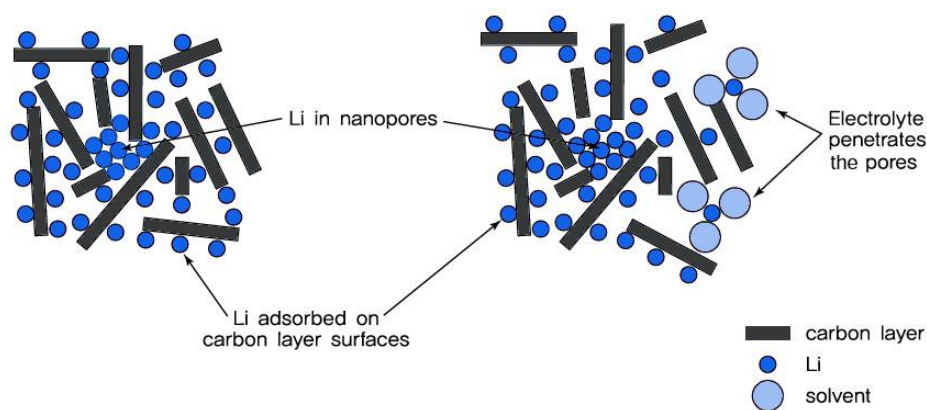


Figure 1.7 Lithium storage mechanism of hard carbon and penetration of electrolyte in pores [31].

In addition to carbon materials, metal alloy anodes such as Sn, Si, Ge, Sb are known for high specific capacity and safety characteristics. They can provide large theoretical capacity that is 2-10 times higher than that of graphite, also a moderate operation potential versus lithium (0.4~0.9 V) [39-41]. However, the performances of these materials were primarily hampered by capacity fading caused by large volume changes (up to 150-300%), or slow reaction kinetics.

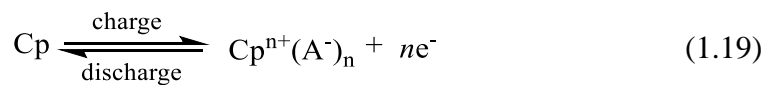
1.2.4 Electrode materials for supercapacitors

Depending on different mechanisms, electrode materials for supercapacitors can be classified into EDL capacitor materials and pseudocapacitor materials. Many different types of carbon can be used as EDL materials. Activated carbons are the most used materials because of their high specific surface area and low cost. They can be prepared from carbon-rich organic precursors by heat treatment under inert atmosphere followed by physical/chemical activation. The activation process may lead to a specific surface area as high as $3000 \text{ m}^2 \text{ g}^{-1}$. For fabricating the electrode, activated carbon (AC)

powders are mixed with conductive carbon black and organic binder to form a slurry which is then coated onto current collectors. When operating in organic electrolytes, AC electrodes give a capacitance of up to 100 F g^{-1} and a cell operating voltage of up to 2.7 V. Using aqueous electrolytes, the capacitance of AC electrodes can be increased to 200 F g^{-1} but the operating voltage is limited to 1 V [42].

Carbon aerogels are made from organic gel precursors prepared by a sol-gel route through a poly-condensation reaction. After pyrolysis treatment of the precursor gel under an inert atmosphere, a controlled and uniform mesoporous structure (pore size, 2-50 nm) is then formed. The gravimetric capacitance of a carbon aerogel is in the range of $50\text{-}100 \text{ F g}^{-1}$ [43]. However, the low density of aerogel materials results in a poor volumetric capacitance that limits their practical application.

Pseudocapacitive materials are able to store higher amount of energy than that of EDL materials. Conducting polymers (CPs) such as polyaniline (PANI), polypyrrole (PPy) and poly[3, 4-ethylenedioxythiophene] (PEDOT), are important classes of pseudocapacitance active materials. They can store and release charges through fast faradic reactions. Conducting polymers can be *p*-doped with (counter) anions or *n*-doped with (counter) cations. PANI and PPy can only be *p*-doped, whereas polythiophene derivatives can be both *p*-doped and *n*-doped. Taking *p*-doped conducting polymer as an example, when oxidation occurs (*p*-doping), ions from the electrolyte are transferred to the polymer backbone and, on reduction (undoping state), they are released back into the solution. The simplified equation for this charge/discharge process of *p*-doped conducting polymer is as follows:



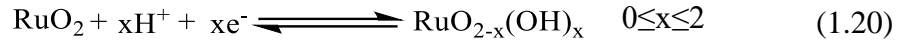
EDL materials based supercapacitors have high power capabilities, due to the fast ion adsorption and desorption, but a low specific energy. Conducting polymers can increase the stored energy as they undergo electrochemical redox reactions in addition to the EDL mechanism. However, they suffer from slow ions diffusion within the bulk of the electrode, resulting in relatively low power density. Nevertheless, it is still proposed that conducting polymers can bridge the gap between batteries and supercapacitors, for they could provide higher energy than EDL materials and undergo faster charge/discharge process than batteries. The typical dopant level for these polymers, as well as their typical specific capacitances and voltage ranges, are given in Table 1.2 [44].

Table 1.2 Theoretical and experimental specific capacitances of common conducting polymers [44-49].

Conducting Polymer	Dopant Level	Potential Range (V)	Theoretical (F g ⁻¹)	Measured Aqueous (F g ⁻¹)	Measured Value Organic (F g ⁻¹)
PANi	0.5	0.7	750	742 [46]	430 [48]
PPy	0.33	0.8	620	530 [45]	450 [49]
PEDOT	0.33	1.2	210	92 [50]	140 [47]

Transition metal oxides (TMO), as pseudocapacitive materials, are able to store more energy than carbon materials, and possess better electrochemical stability than conducting polymers. Noble metal oxides such as RuO₂ and IrO₂, exhibit good conductivity and excellent power densities. Take RuO₂ as an example, it has three oxidation states within 1.2 V, delivering a specific capacitance of up to 1580 F g⁻¹ [51]. Also protons can participate in the redox reaction, where RuO₂ acts as “proton

condenser”. The mechanism of RuO₂ as pseudocapacitive materials in acidic solution can be described as [52]:



The main drawbacks of these noble metal oxides as electrode materials are their high cost and potential harm to the environment. However, low cost metal oxides such as MnO₂, NiO, Co(OH)₂, Fe₃O₄ have been explored [53-56], and present outstanding pseudocapacitive behavior. A specific capacitance of 698 F g⁻¹ [54], 1329 F g⁻¹ [53], 2646 F g⁻¹ [56] is reported for MnO₂, NiO and Co(OH)₂, respectively. Among these metal oxides, manganese oxide is the one that possesses the advantages of abundance, no toxicity, ease of synthesis and high capacitance. The proposed mechanism is that protons or alkali metal cations can intercalate into/de-intercalate from the MnO₂ crystal lattice upon reduction/oxidation, which is similar to that of RuO₂ [57].

However, TMOs suffer from poor rate capability and cycle performance, which reduces their ability to reach their maximum capacitance value under a high current rate or after long-term cycling. Specific to electrodes for flexible power sources, TMOs powder or nanoparticles are unfavourable for forming flexible electrodes compared with conducting polymers and graphene. For this reason, investigations of materials for flexible electrodes in this thesis were mainly focused on graphene or its composites with conducting polymers.

1.3 Graphene for Energy Storage Application

As mentioned above, various types of carbon materials play vital roles in LIBs or supercapacitors [20, 58]. To meet the requirements of the rapid development of consumer electronics and green vehicles, the key challenge is to develop novel carbon

materials with higher energy and power density. Graphene, an emerging star in nanocarbon materials, is composed of one-atom-thick planar sheets consisting of sp^2 -bonded carbon atoms densely packed in a honeycomb crystal lattice. Theoretically, graphene without any disorder has a remarkably high electron mobility in excess of $200,000 \text{ cm}^2 \text{ V}^{-1} \text{ s}^{-1}$ at room temperature [59]. The theoretical specific surface area of graphene can reach up to $2630 \text{ m}^2 \text{ g}^{-1}$, twice of that for CNTs [60]. Due to its high theoretical surface area and ability to facilitate electron transfer along the surface, graphene is proposed to be excellent materials for LIBs or SCs.

1.3.1 Graphene and its preparation

Although the concept of monolayered graphene can be tracked back to the 1960s-1970s [61], not until 2004 was graphene firstly prepared and studied by Andre Geim and Konstantin Novoselov [62]. Graphene was obtained via mechanical exfoliation of graphite by a simple scotch tape method. The adhesive tape was used to repeatedly split graphite crystals into increasingly thinner pieces. The exfoliated transparent monolayer graphene flakes attached on the tape was then dissolved in acetone. For their contributions regarding graphene materials, Andre Geim and Konstantin Novoselov were awarded jointly the 2010 Nobel Prize in Physics.

A different “bottom up” strategy was then developed to directly grow graphene onto a substrate surface. There are two different ways for graphene growth, depending on the carbon source: carbon already exists in the substrate or to be added by chemical vapor deposition (CVD). Graphene can be epitaxially grown by simply heating and cooling a SiC crystal. The 6H-SiC single crystal is heated in an ultra-high vacuum (UHV) to high temperature ($>1300^\circ\text{C}$), which causes Si to sublime, forming wafer-

size graphene on the surface [63]. This method is highly dependent on the parameters including temperature, heating rate and pressure. The growth of carbon nanotubes instead of graphene can occur if the temperature and pressure is too high [64].

CVD is a process where a substrate is exposed to gaseous compounds. Then these compounds decompose on the substrate surface to grow a thin film, while the by-products evaporate. Graphene can be grown by the CVD method from carbon containing gases on catalytic metal surfaces or by surface segregation of carbon dissolved in the bulk of metals. The growth of graphene through graphitization of Ni in a CH₄-H₂ mixture at ≥ 1000 °C follows a combined process of surface-mediated deposition and surface segregation. The carbon atoms from the decomposition of CH₄ are diffused into the metal, forming a “solid solution”. The carbon dissolved is then segregated on the metal surface upon cooling, producing graphene monolayers. Through a surface-mediated CVD process, graphene can be deposited on Cu surface with methane and hydrogen gas as precursors [65]. Since the solubility of C in Cu is minimal compared to Ni, graphene can form on Cu only by direct decomposition of the C containing gas on the catalytic Cu surface. The graphene growth process on Cu can be easily controlled to stop at one monolayer. In contrast, such control is very difficult on Ni due to the considerable solubility of C in Ni [66, 67].

In order to facilitate large scale production of graphene, a “top down” strategy was followed where, in addition to mechanical exfoliation, an exfoliation method using graphite (or graphite oxide) as precursor was developed. By overcoming the van der Waals attractions between graphene layers, liquid-phase exfoliation of “pristine” graphite assisted by ultrasonication can produce defect-free graphene. Immersion of graphite in liquid can reduce the strength of van der Waals attractions, for the energy between adjacent layers will be balanced by the interactions between liquid and graphite

sheets. The graphene flakes tend to separate from each other and disperse into the liquid if the interfacial tension between solid and liquid is low enough [68]. With a surface tension γ around 40 mJ m^{-2} , solvents such as N-methyl-2-pyrrolidone (NMP, $\sim 40 \text{ mJ m}^{-2}$), N, N-dimethylformamide (DMF, $\sim 37.1 \text{ mJ m}^{-2}$) and ortho-dichlorobenzene (o-DCB, $\sim 37 \text{ mJ m}^{-2}$) are the best choice for exfoliation of graphite [50]. Graphene dispersions with concentrations of up to $\sim 0.01 \text{ mg ml}^{-1}$ can be produced by exfoliation of graphite in NMP. This method results in the monolayer yield of $\sim 1 \text{ wt\%}$, and can potentially be improved to 7-12 wt% through recycling of the sediment (Figure 1.8) [50]. The obtained graphene is confirmed to have no defects or oxygen functional groups.

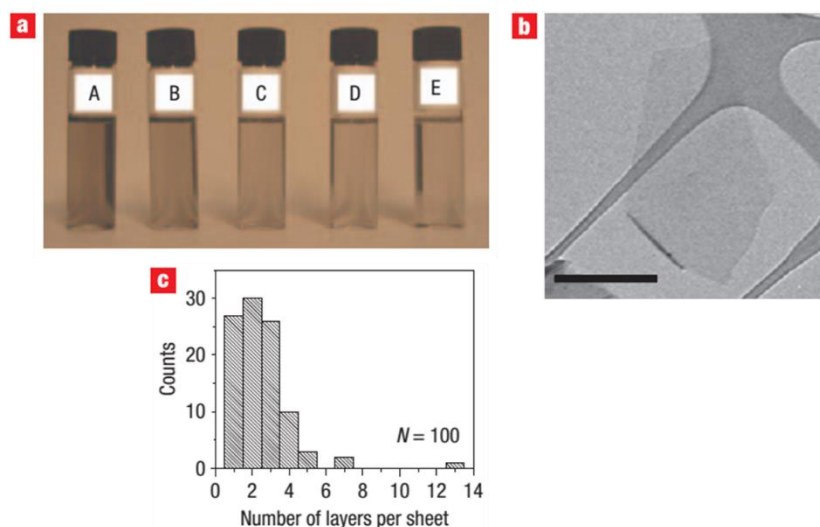


Figure 1.8 (a) Dispersions of graphite flakes in NMP, at a range of concentrations ranging from 6 mg ml^{-1} (A) to 4 mg ml^{-1} (E) after centrifugation. (b) Bright-field TEM images of monolayer graphene flakes deposited from NMP. (c) Histogram of the number of visual observations of flakes as a function of the number of monolayers per flake for NMP dispersions [50].

The use of surfactant in solvent exfoliation, can promote the exfoliation of graphite, especially when the surfactant has high adsorption energy on the basal plane of

graphene, higher than that of the solvent molecule interacting with graphene. Also the surfactant can stabilize the exfoliated graphene, where the zeta potential of the surfactant stabilized graphene controls the dispersion concentration [69]. Coleman *et al.* demonstrated that the successful exfoliation of graphite in water-sodium dodecylbenzene sulfonate (SDBS) solution [69]. It is revealed that over 40% of exfoliated flakes are less than 5 layers and 3% of the flakes are monolayer. Moreover, the sediment remaining after centrifugation can be recycled to improve the overall yield of graphene exfoliation. Recycling the sediment results in narrowing of the flake thickness distribution, shifting it toward thinner flakes with large quantities of bilayers or trilayers (67% of flakes have <5 layers). Cationic surfactants like cetyltrimethylammonium bromide (CTAB) can also be used to assist the solvent exfoliation of graphite. The mass fraction of graphene via solvent exfoliation is typically less than 0.01 wt%. To address this issue, Notely *et al.* developed a method through continuous addition of surfactant to prepare highly concentrated graphene suspension of up to 1.5 wt% via solvent exfoliation (Figure 1.9) [70]. By continuously replacing the surfactant to lower the surface tension during sonication, the concentration of flakes can be significantly increased.

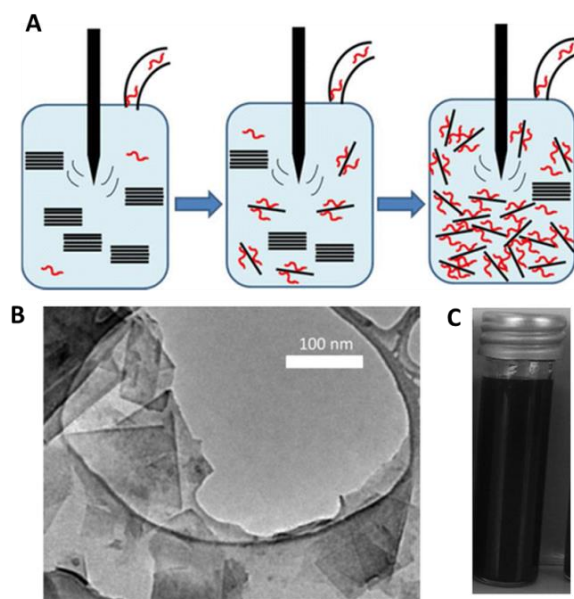


Figure 1.9 (A) Schematic procedure of exfoliation of graphite with gradually added surfactant; (B) TEM image of graphene; (C) Image of a highly concentrated graphene suspension [70].

Graphene production through the graphite oxide exfoliation route is the mostly used one due to its low-cost, large-scale production and easy manipulation. Graphite oxide can be produced by oxidation of graphite via various methods as reported by Brodie, Hummers, and Staudenmeier [71]. Graphite is oxidized by the combination of potassium chlorate with nitric acid (Brodie and Staudenmaier) or potassium permanganate with sulfuric acid (Hummers). The formed graphite oxide is still a layered stack of puckered sheets but has much larger interlayer distance (0.7~1.2 nm) than graphite (0.335 nm) [72], thus can be easier to exfoliate into graphene oxide in solvents upon the application of mechanical energy.

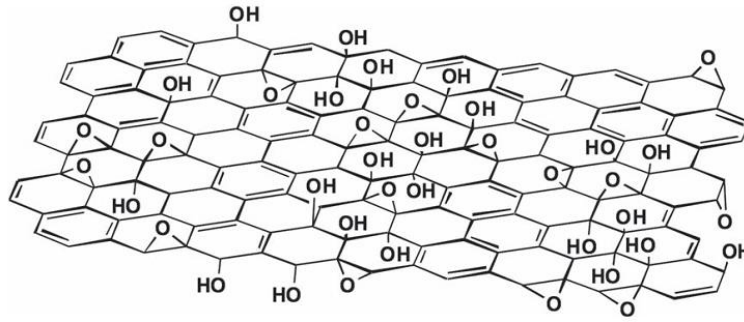


Figure 1.10 A proposed schematic of graphene oxide structure [73].

Graphene oxide is an insulation material due to the disrupted sp^2 bonding networks. To recover its electrical conductivity, GO needs to be reduced to restore its π - π conjugated structure. The product of GO reduction has been given a variety of names, including reduced graphene oxide (rGO), chemically reduced graphene (CRG), chemical converted graphene (CCG) or graphene. Ruoff *et al.* first prepared reduce graphene oxide from the exfoliation of graphite oxide [74, 75]. Graphite oxide was prepared using a modified Hummers' method, and then exfoliated into water with the assistance of ultrasonication. Hydrazine hydrate was used to reduce graphene oxide (Figure 1.11). This treatment results in the formation of unsaturated and conjugated carbon atoms, which can partially recover the electrical conductivity. In addition to hydrazine reduction, GO can be reduced with other chemical reducing agents (i.e. ascorbic acid, sodium borohydride, etc.) [76, 77]. It can also be reduced via thermal treatment [78] or electrochemical routes [79, 80].

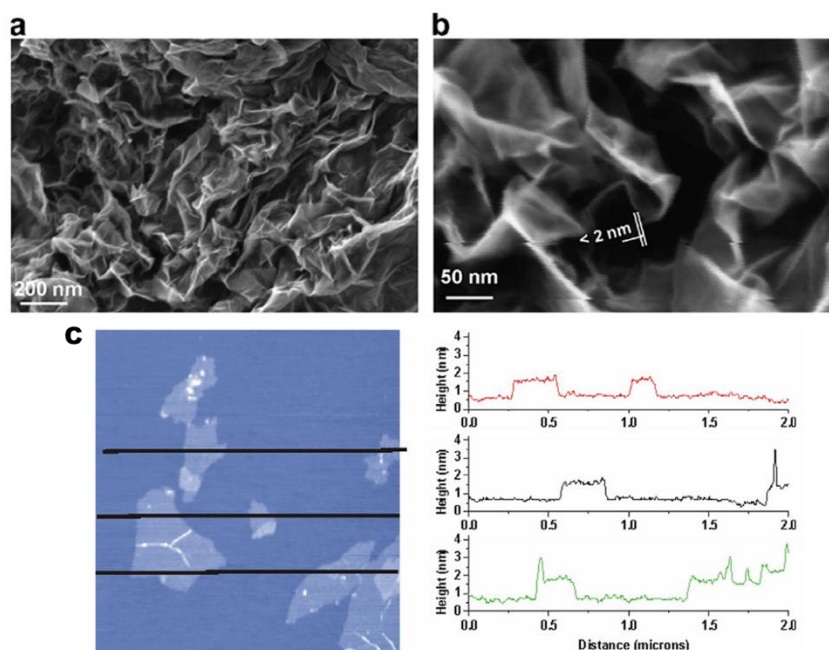


Figure 1.11 (a) An SEM image of aggregated reduced GO sheets; (b) A platelet having an upper bound thickness at a fold of ~ 2 nm; (c) AFM image of exfoliated GO sheets with three height profiles acquired at different locations [31].

1.3.2 Graphene based materials for energy storage

Theoretical study has shown that, a single layer graphene sheet can accommodate Li^+ ions on both sides to create a Li_2C_6 structure, providing twice the capacity (744 mAh g^{-1}) of that from conventional carbon materials. In highly disordered graphene, the theoretical capacity can be even higher than the Li_2C_6 model due to the contribution of defects in the edge sites and internal basal planes (Figure 1.12) [81]. The disordered graphene delivered a reversible capacity of $794\text{-}1054 \text{ mAh g}^{-1}$, which is close to Li_2C model proposed for disordered carbon by Sato *et al.* [82].

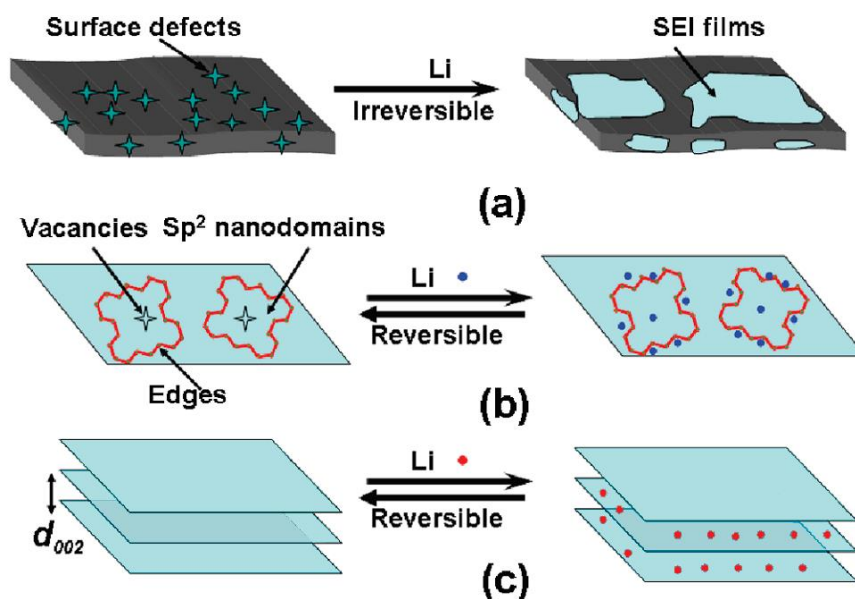


Figure 1.12 (a) Irreversible Li Storage at the Interface between the Graphene Nanosheets and Electrolyte; (b) Reversible Li Storage at Edge Sites and Internal Defects (Vacancies etc.) of Nanodomains Embedded in Graphene Nanosheets; (c) Reversible Li Storage between (002) Planes [81].

In 2008, graphene sheet-based electrodes were firstly employed by Yoo et al. for lithium storage, and achieved a capacity of 540 mAh g^{-1} [83]. This value was lower than the theoretical calculation, which may be caused by the restacking of graphene. The lithium storage capacity of graphene nanosheets material can be increased to 730 and 784 mAh g^{-1} , with carbon nanotubes or fullerenes introduced to increase the inter-graphene sheet distance (Figure 1.13).

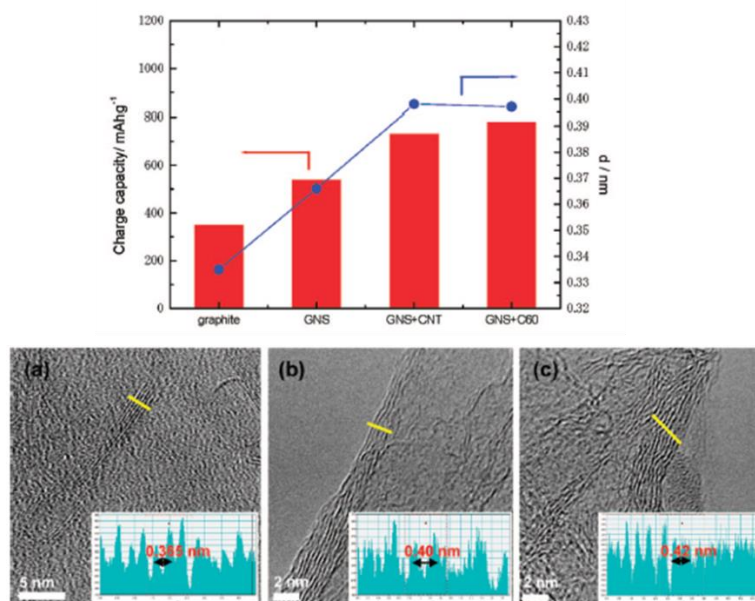


Figure 1.13 Graphene for batteries. (A) Relationship between the d-spacing and the charge capacity of graphene nanosheet (GNS) families and graphite; (B) Cross-sectional TEM images of GNS families with almost the same numbers (5–6) of graphene stacking layers for (a) GNS, (b) GNS + CNT, and (c) GNS + C60 [83].

A crumpled-paper-shaped graphene was prepared by means of rapid heating and ultrasonication. This graphene anode exhibited a reversible capacity of 672 mAh g⁻¹ and good cycle performance [84]. Flower-petals shaped loose graphene nanosheets powders were prepared by a soft-chemistry approach, and exhibited a reversible capacity of 650 mAh g⁻¹ [85]. It was proposed that the nano-cavities formed between graphene sheets due to scrolling and crumpling contribute to the lithium storage [86].

With the merits of theoretically high surface area and excellent conductivity, graphene are also expected to be an ideal material for supercapacitors. The intrinsic capacitance of one single-layer graphene was reported to be ~21 mF cm⁻². Theoretically graphene could achieve an EDL capacitance of ~550 F g⁻¹ [87]. Supercapacitors based on graphene was first reported by R. S. Ruoff's group [88]. They used chemically

modified graphene (CMG) with a high specific surface area of $705 \text{ m}^2 \text{ g}^{-1}$ as the electrode materials that provided a specific capacitance of 135 F g^{-1} in aqueous electrolyte and 99 F g^{-1} in organic electrolyte (Figure 1.14).

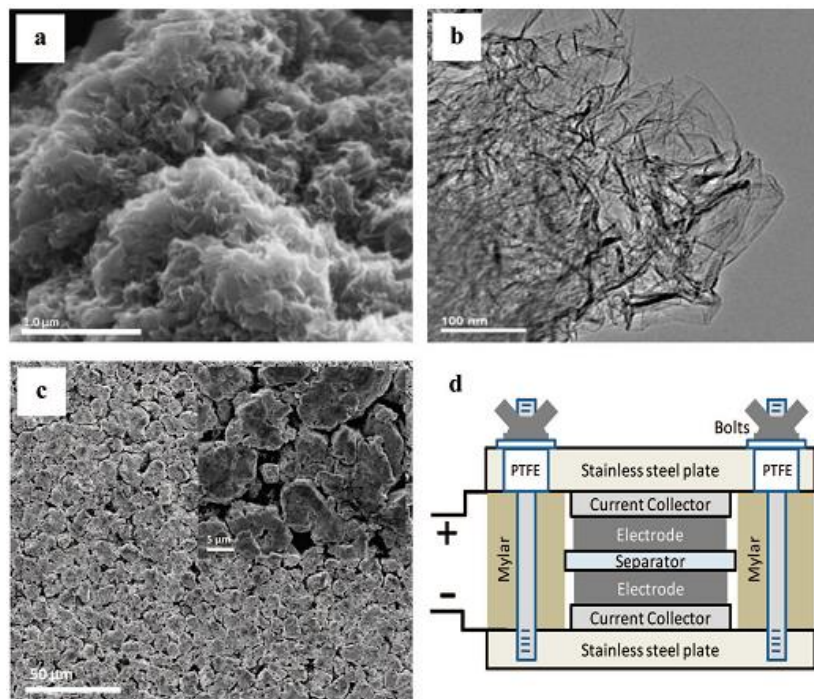


Figure 1.14 (a) SEM image of CMG particle surface, (b) TEM image showing individual graphene sheets extending from CMG particle surface, (c) low and high (inset) magnification SEM images of CMG particle electrode surface, and (d) schematic of test cell assembly [88].

Carbon can be activated with steam, KOH, and $\text{KOH}+\text{CO}_2$, forming activated carbon with a specific surface area as high as $2821 \text{ m}^2 \text{ g}^{-1}$ [89]. A similar strategy can also be utilized to prepare activated graphene. Porous graphene was produced by KOH activation of the microwave exfoliated graphite oxide [90]. The activation process created pores with 0.6-5 nm in width on the graphene surface, forming a continuous, 3D carbon network with atom-thick walls (Figure 1.15). Such porous graphene afforded combined high electrical conductivity and high surface area ($3100 \text{ m}^2 \text{ g}^{-1}$). It achieved

an energy density of 70 Wh kg^{-1} at a current density of 5.7 A g^{-1} in ionic liquid (1-ethyl-3-methylimidazolium bis(trifluoromethylsulfonyl)imide).

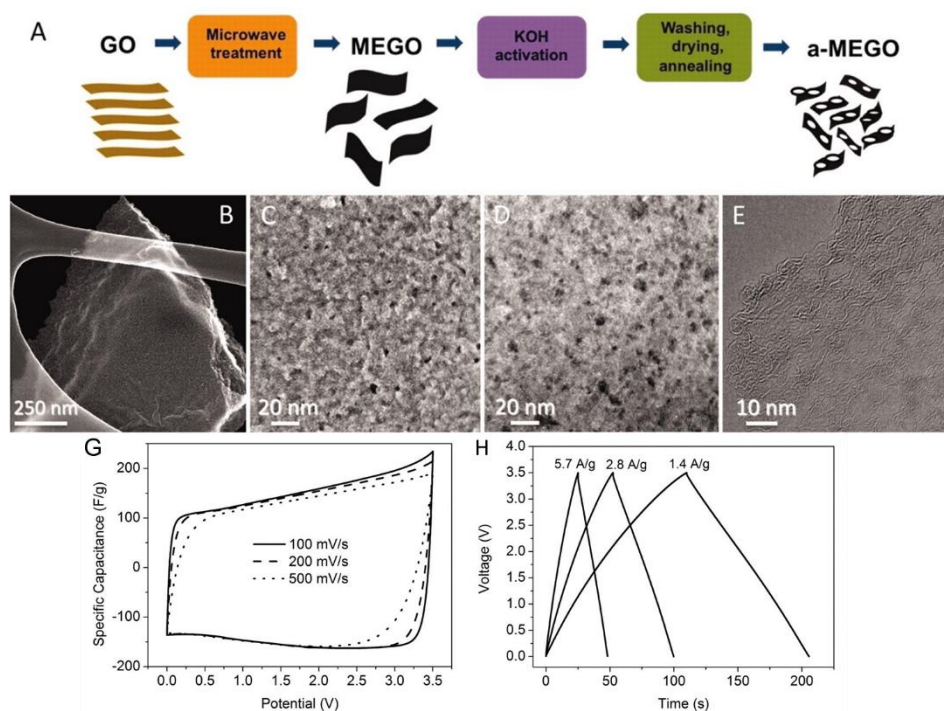


Figure 1.15 (A) A schematic to show the preparation procedure of KOH activated microwave exfoliated GO (a-MEGO); (B) Low-magnification SEM image of a-MEGO; (C) High-resolution SEM image of a-MEGO that demonstrates the porous morphology; (D) ADF-STEM image of the same area as (C); (E) High-resolution phase contrast electron micrograph of the thin edge of a-MEGO chunk; (F) CV curves at different scan rates; (G) Galvanostatic charge/discharge curves under different constant currents [90].

1.4 Graphene Based Flexible Electrodes

The inherent excellent mechanical and electronic properties of graphene make it an attractive material for applications in flexible energy storage devices. With one-atom layer thick structure, graphene is easily deformed in the vertical direction to the surface,

providing good flexibility. In flexible energy devices, graphene based materials can work with multiple functions. They can serve as high performance active materials, also they can provide flexibility for their excellent mechanical properties. Graphene materials can be made into substrate-supported flexible electrodes, intrinsic flexible fibres, free-standing papers/films or three-dimensional macro-assemblies [91]. Furthermore, graphene sheets can be incorporated with conducting polymers or inorganic metal oxides forming composites. It can serve as a flexible backbone to enhance the flexibility of the composites, and can also help to improve the rate and cycle stability of conducting polymers or metal oxides.

1.4.1 Flexible graphene electrodes with mechanical support

The mechanical support for graphene-based flexible electrodes can be either planar substrates like plastics and metal foils, or porous substrates including textiles, cellulose papers and sponges. Flexible, thin and light-weight plastics such as polyethylene terephthalate (PET) are ideal substrates. An ultrathin, transparent (70% transmittance) PET supported graphene film showed a specific capacitance of 135 F g^{-1} at a current density of 0.75 A g^{-1} [92]. A multilayer film of Co, Al layered double hydroxide nanosheets and graphene on PET substrate via layer-by-layer assembly can achieve a high specific capacitance of 1204 F g^{-1} and 9 mF cm^{-2} [93].

Compared to planar flexible substrates, textile [94], sponge [95], and cellulose paper [96] substrates have large surface area and porous structure. Therefore, flexible graphene electrodes on those substrates have demonstrated an enhanced electrochemical performance. It can be achieved by simply dip-coating or by a filtration process. Cheng *et al.* fabricated a flexible graphene-cellulose paper (GCP) membrane by simple vacuum

filtration of graphene dispersion through cellulose paper [96]. The graphene nanosheets penetrated throughout the cellulose paper, and strongly bound to the cellulose fibres (Figure 1.16). Benefiting from the macroporous structure of the cellulose paper and the excellent conductivity of graphene, the obtained film shows high stability with a decrease of only 6% after being bent 1000 times. Such a flexible electrode exhibited an areal capacitance of 81 mF cm^{-2} and a gravimetric capacitance of 120 F g^{-1} . An all solid-state flexible supercapacitor based on GCP using H_2SO_4 -PVA electrolyte exhibited a capacitance as high as 46 mF cm^{-2} .

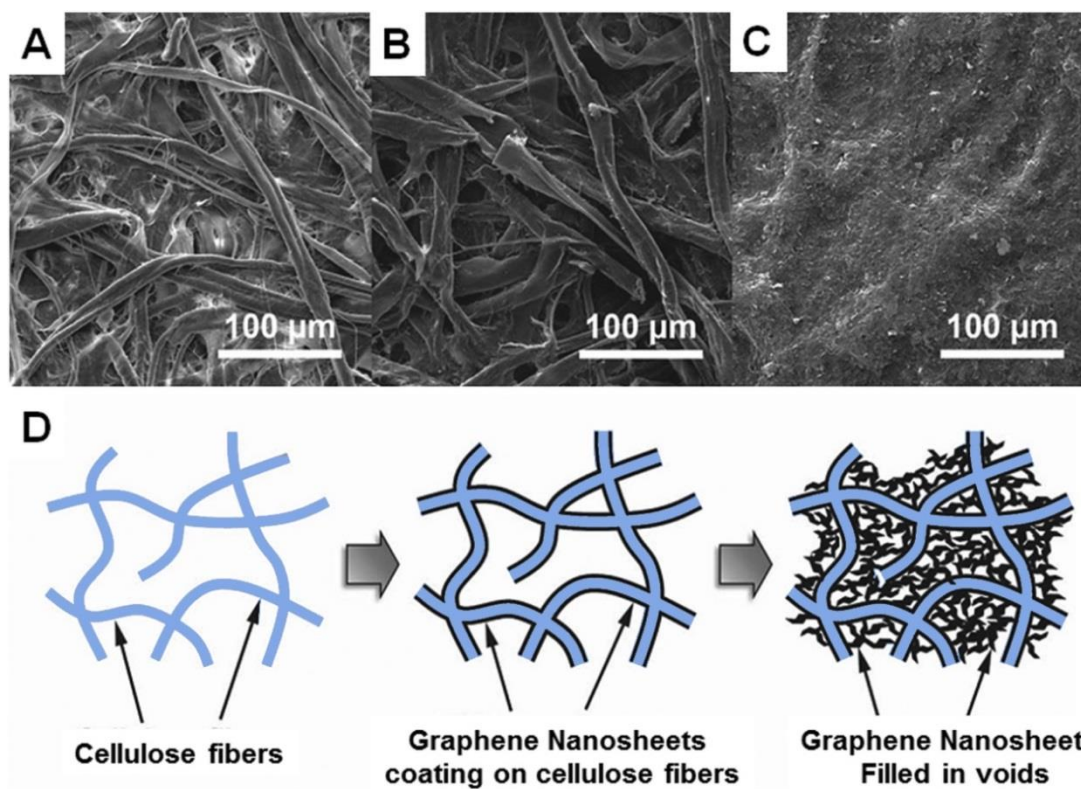


Figure 1.16 SEM images of the filter paper or graphene–cellulose paper surfaces with different graphene nanosheet loading amounts. (A) 0 wt% (pristine filter paper), (B) 2.3 wt%, and (C) 7.5 wt%. (D) Illustration of the structural evolution of graphene–cellulose paper as the graphene nanosheets loading increases [96].

Textiles with hierarchical network and complex surface morphology, are another commonly used porous substrate. These textiles have hierarchical network structures with a complex surface morphology. The hydroxyl functional groups and high porosity in the textile substrate could facilitate electrolyte ions transportation and integration with the active materials. Liu et al. prepared a flexible graphene based electrode via a simple “brush-coating and drying” method [94]. Cotton cloth was used as substrate and GO suspension was “ink”. Graphene based fabric exhibits good electrical conductivity, outstanding flexibility, and strong adhesion between graphene and cotton fibres. An all fabric supercapacitor with cotton cloth as separator and these graphene fabric electrodes can achieve a high specific cell capacitance of 81.7 F g^{-1} (based on the total mass of electrodes) at a scan rate of 10 mV s^{-1} .

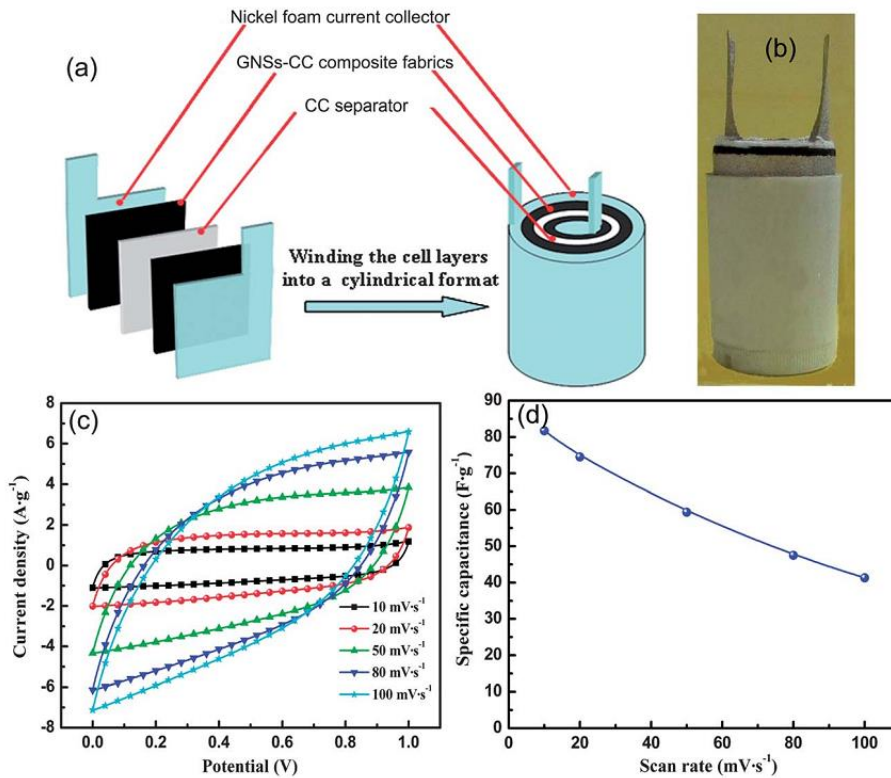


Figure 1.17 (a) A schematic diagram of the structure of an assembled symmetric supercapacitor, (b) photo of the assembled supercapacitor, (c) CV curves of the

assembled supercapacitor at various scan rates in 6 M KOH solution, and (d) its specific capacitances at various scan rates [94].

Using metal foils as substrates, graphene based flexible electrodes are expected to have better performance due to their very low resistance. Based on a CVD method, monolayer graphene was grown on Cu foil to obtain a flexible cathode [97]. An all-solid-state battery was assembled using this flexible electrode, a lithium foil anode and thin polymer electrolyte [poly(ethylene glycol) borate ester- LiClO_4]. The 50 μm thick flexible device shows a volumetric energy density of 10 Wh L^{-1} at a power density of 50 W L^{-1} and a stable cyclic performance of up to 100 cycles.

1.4.2 Free-standing graphene based flexible electrodes

1.4.2.1 Flexible graphene based paper/film electrodes for LIBs

Although the utilization of a mechanical support is a simple and effective strategy to realize flexible electrodes, this technique also suffers from some drawbacks. The attachment between substrate and graphene coating can be affected or deteriorated during repeated deformation. More importantly, the introduction of a substrate adds dead weight and dead volume to the device. Therefore, it is more favourable to use conductive, intrinsic flexible films/papers to meet the requirements of flexible electrodes. Such intrinsic free-standing materials can endure repeated deformation without affecting the performance; also can be easily made into the designed shape. It can help reduce the total weight of the device because the flexible electrode can be fabricated without substrate, and used directly without the need of binder and current collector.

Ultrathin, flexible and light-weight freestanding graphene-based films or papers have attracted much attention. It can be fabricated via various methods that include Langmuir-Blodgett, layer-by-layer deposition, interfacial self-assembly, spin-coating and vacuum filtration. Driven by the intersheets π - π interactions, the highly ordered free-standing graphene paper can be easily formed from a well-dispersed graphene dispersion assisted by vacuum filtration [98, 99]. Such graphene papers are ideal materials for flexible electrodes due to their facile preparation and superior flexibility. The performance of such graphene paper as a lithium battery anode was first reported by Wang et al [100]. It displayed the first discharge capacity of 582 mAh g^{-1} and a reversible capacity of only 84 mAh g^{-1} at 50 mA g^{-1} (Figure 1.18). The plateau in the first discharge at 2.20 V was attributed to lithium interactions with the residual oxygen-containing functional groups within graphene nanosheets. The unsatisfactory performance may be ascribed to the restacking effects of the graphene sheets during formation of the paper.

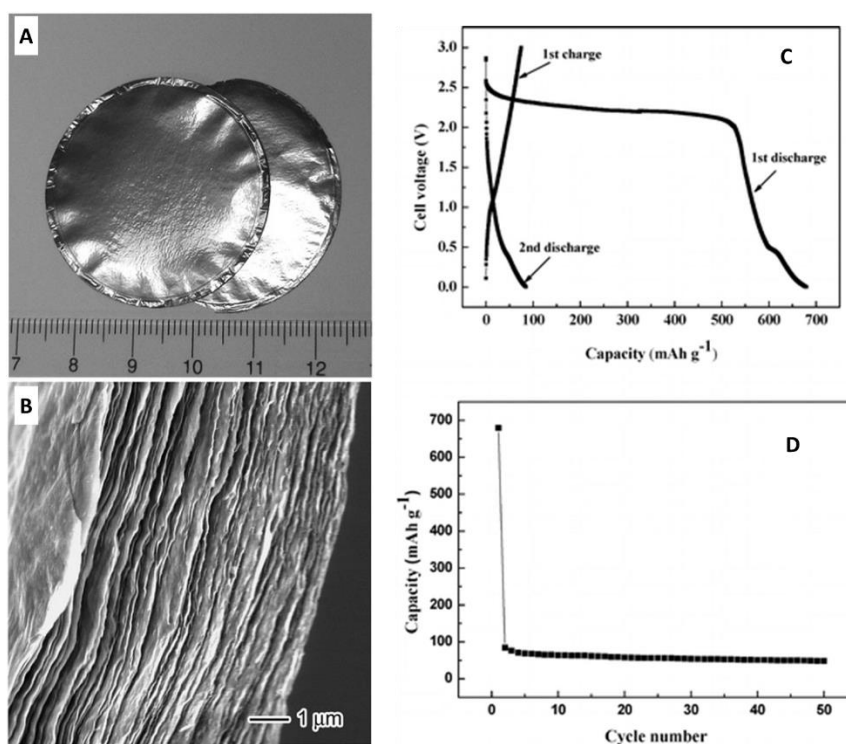


Figure 1.18 (A) Photograph of two pieces of free-standing graphene paper fabricated by vacuum filtration of chemically prepared graphene dispersions, followed by air drying and peeling off the membrane. Front and back surfaces are shown. (B) Side-view SEM images of a ca. 6 μm thick sample. (C) Charge/discharge profiles and (D) cycle performance of graphene paper at a current density of 50 mA g^{-1} [99, 100].

A non-annealed graphene paper was prepared via reduction of graphene oxide paper with hydrazine, and it displayed improved cycling stability but with low capacity and poor rate capability. The capacity was still 84 mAh g^{-1} at 50 mA g^{-1} , and can increase to 214 mAh g^{-1} at a lower current density of 10 mA g^{-1} [101]. Kung et al. used ultrasonic vibration and mild acid oxidation to create in-plane porosity on the graphene sheets, and obtained a flexible holey graphene paper (Figure 1.19). The holey defects provided abundant ion binding sites and enhanced lithium ion diffusion kinetics, resulting in an improved performance; especially at high C rates. At 13.3 C and 26.6 C rates, a capacity of 150 and 70 mAh g^{-1} were obtained, without obvious capacity degradation up to 1000 cycles [102].

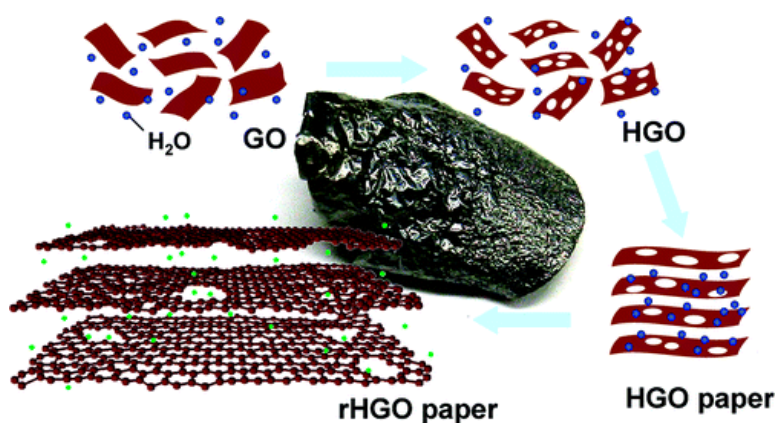


Figure 1.19 Schematic drawing (not to scale) of the introduction of in-plane pores into chemically exfoliated graphene oxide (GO) and the subsequent filtration into a holey graphene oxide paper (HGO) [102].

1.4.2.2 Flexible graphene based paper/film electrodes for SCs

Graphene paper via filtration has also attracted great attention in the research of flexible supercapacitors because of their facile preparation, large-scale fabrication and superior flexibility. However, the severe re-stacking of graphene sheets during the filtration process results in a relatively low specific surface area (SSA) limiting ion diffusion, thus strongly affecting its performance as a supercapacitor electrode. In order to solve the problem, several strategies have been launched to prevent the restacking of graphene sheets, increasing SSA and facilitating ion transport.

It was reported that during the filtration process, graphene can form paper-like wet gel when the repulsive force between hydrated sheets and inter-sheet π - π attractions reach a balance [103]. The graphene sheets in such gel were highly separated. Following such strategy, a flexible electrolyte-mediated chemically converted graphene film (EM-CCG) was created using electrolytes (sulfuric acid, and ionic liquid 1-ethyl-3-methylimidazolium tetrafluoroborate, EMIMBF₄) to inhibit graphene sheets restacking. It was prepared from precursor paper-like graphene hydrogel by exchanging water inside the gel with a mixture of volatile (water) and non-volatile liquid electrolytes (ionic liquid or sulfuric acid), and then evaporating the volatile liquid under vacuum [104]. By adjusting the ratio of volatile and non-volatile liquids, the packing density of the EM-CCG films can be easily tuned from 0.13 to 1.33 g cm⁻³. The highly compact EM-CCG films based symmetric supercapacitors exhibit a gravimetric capacitance of ~190 F g⁻¹ and a high specific volumetric capacitance of 255.5 F cm⁻³ at 0.1 A g⁻¹ in aqueous electrolyte. (Figure 1.20)

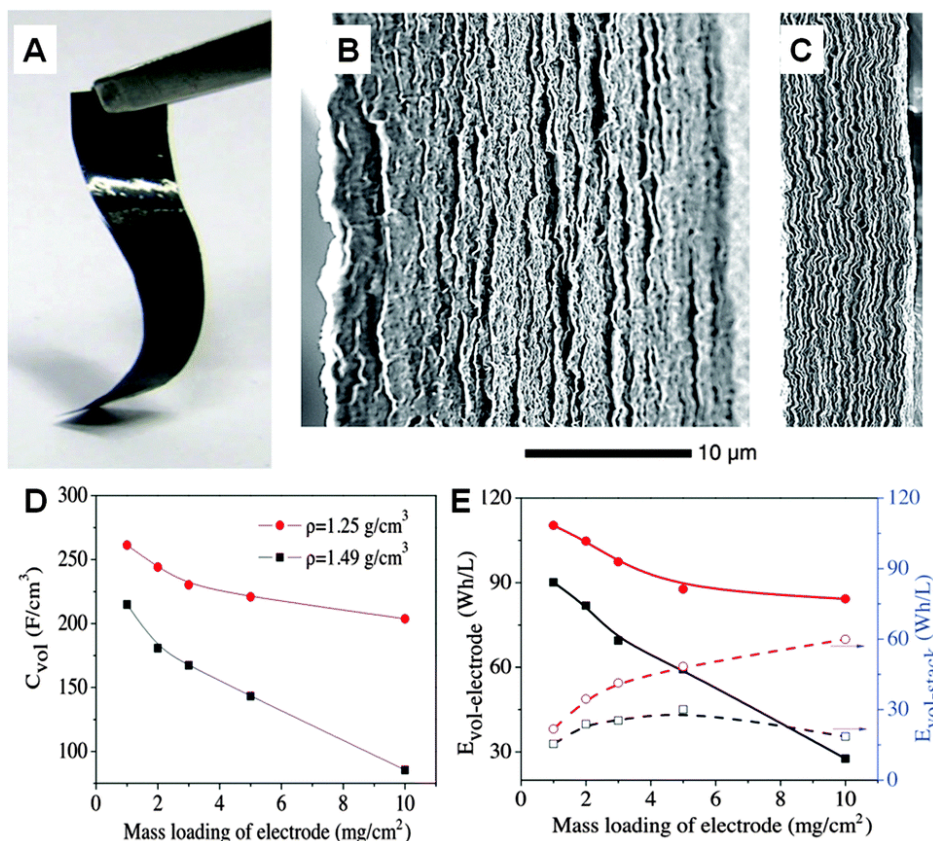


Figure 1.20 (A) A photo showing the flexibility of an electrolyte-mediated chemically converted graphene (EM-CCG) film. (B, C) SEM cross-sectional images of EM-CCG films with mass loadings of 0.42 and 1.33 mg cm⁻³. (D) Volumetric capacitance and (E) energy density as a function of the areal mass loading of an EM-CCG film (1.25 g cm⁻³) and a dried CCG film (1.49 g cm⁻³) at a current density of 0.1 A g⁻¹ [104].

Alternative strategies including self-assembly, freeze drying and laser scribing have been developed to fabricate graphene paper (or film) from the chemically converted graphene [105-107]. Liu et al. prepared graphene paper from pressing a freeze-dried graphene aerogel (Figure 1.21) [106]. That flexible graphene paper consists of wrinkled graphene sheets, delivering a high charge capacity of 864 mAh g⁻¹ at 100 mA g⁻¹ with a Coulombic efficiency above 98% at the second cycle. The author

proposed that the existence of graphene sheets folding could enhance the accessibility of Li^+ ions and electrolyte, resulting in an exceptional performance.

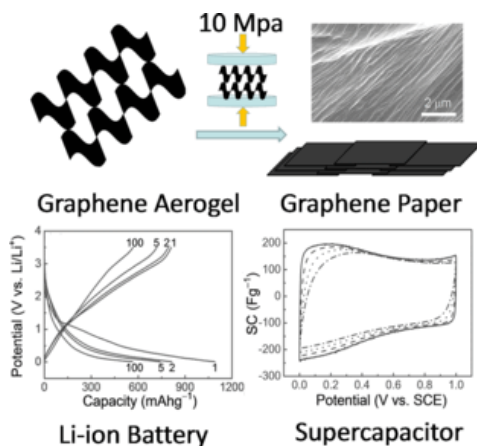


Figure 1.21 Illustration of the formation process of graphene paper and its performance as a lithium-ion battery or supercapacitor electrode. Reproduced with permission [106].

1.4.2.3 Three dimensional (3D) graphene based flexible electrodes

The electrochemical performance of graphene based electrode can be significantly affected by electrolyte and electron transportation ability, which depends on the nanostructures of graphene materials. Free-standing graphene materials with 3D porous structure, such as aerogels, foams and sponges, can provide high surface area and fast ion/electron transport. Chen *et al.* prepared paper-like graphene foam following the “leavening” strategy (Figure 1.22) [108]. The precursor GO paper by filtration was placed into a sealed autoclave to react with the additive hydrazine monohydrate, producing bread-like graphene foams after being reacted at 90 °C for 10 h. The foam-like graphene paper was composed of an open porous network with pores ranging from sub-micrometre to several micrometres. Such graphene foam based symmetric SCs

showed a capacitance of 110 F g^{-1} at 0.5 A g^{-1} , much larger than that of compact graphene paper based SCs (17 F g^{-1}).

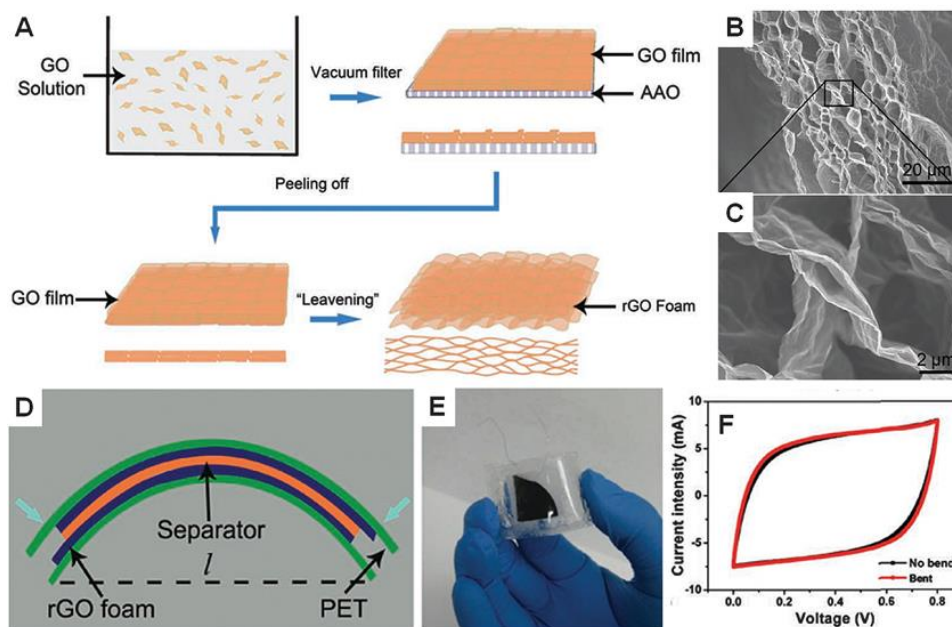


Figure 1.22 (A) Schematic drawings illustrating the process to prepare RGO foams. (B and C) Cross-sectional SEM images of RGO foams. (D and E) Schematic diagram and optical image of the flexible RGO foam supercapacitor. (F) CV curves of the RGO foam supercapacitor before bending and while bent [108].

Gelation is a simple, straightforward route to prepare 3D porous macroscopic functional materials. A zinc ion induced interfacial gelation approach was developed to fabricate a 3D porous graphene framework at large scale (Figure 1.23) [109]. By simple immersion of a Zn template with arbitrary shape in the aqueous dispersions of GO, the gelation as well as GO reduction spontaneously occurred at the Zn surface, forming 3D graphene gel with continuous porous network. Such method provides a facile route to obtaining 3D graphene gels with specific shapes. Accordingly, the freeze-dried graphene hydrogel films exhibited a high specific area of up to $778.5 \text{ m}^2 \text{ g}^{-1}$. A

supercapacitor based on such graphene gel delivered a gravimetric specific capacitance of 76.8 F g^{-1} at 2.3 A g^{-1} and an areal specific capacitance of 33.8 mF cm^{-2} at 1 mA cm^{-2} . An outstanding cycle performance was also demonstrated, with a capacitance retention of 97.8% after 4,000 cycles.

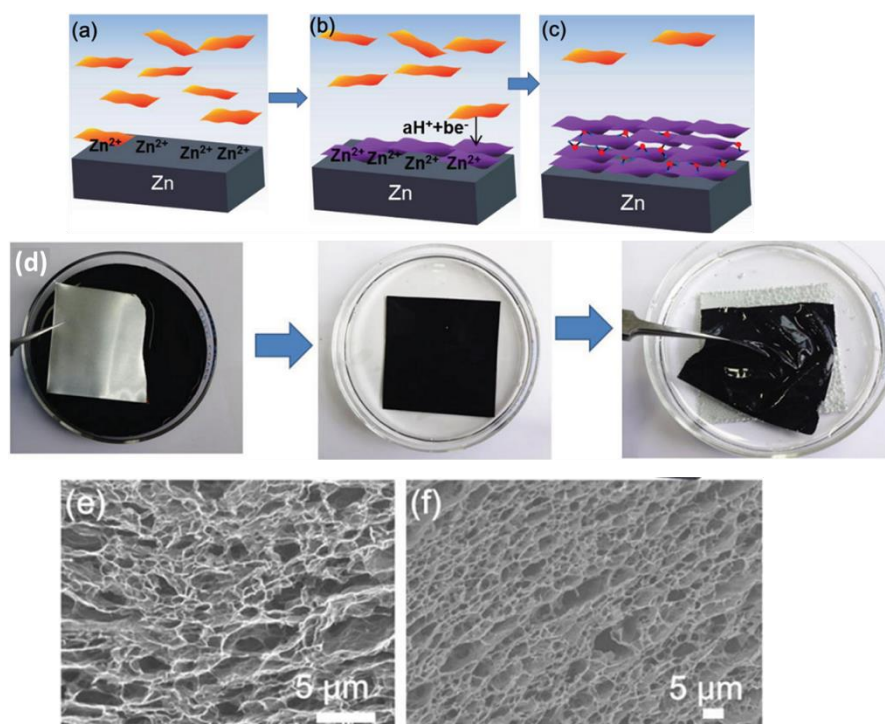


Figure 1.23 (a-c) Schematic illustration of the interfacial gelation mechanism; (d) Graphene gelation procedure; (e-f) SEM images of freeze-dried aerogels prepared at different conditions [109].

Alternatively, an hydrothermal method was also developed to prepare Graphene hydrogels or aerogels [110]. However, the poor mechanical strength hindered their direct use as flexible electrodes. Duan *et al.* addressed this issue by simply pressing the hydrothermal graphene hydrogel onto a current collector, and obtained a flexible 3D graphene hydrogel film electrode. An all solid-state supercapacitor was then assembled

using such flexible graphene hydrogel electrode with polymer electrolyte. The graphene hydrogel film based all solid-state supercapacitor showed a high specific capacitance of 186 F g^{-1} at a current density of 1 A g^{-1} . Due to the high mass loading, this 3D graphene hydrogel film achieved a superior area-specific capacitance of 372 mF cm^{-2} . As a flexible supercapacitor, the device was able to be bent up to 150° , and showing an 87% capacitance retention after 10,000 cycles under this bending angle.

Template assisted assembly is a versatile approach to construct 3D nanostructured materials. Su *et al.* used a template-mediated assembly method to fabricate a macroporous ‘bubble’ flexible graphene paper (Figure 1.24) [111]. The graphene oxide precursor along with PMMA template spheres were orientatedly assembled by vacuum filtration. After calcination, the reduction of graphene oxide and removal of polymer template occurs simultaneously. The utilizable total capacitance of this ‘bubble’ graphene paper is 92.7 F g^{-1} (determined by EIS), which is 3 times higher than that from the compact graphene paper. Furthermore, the ‘bubble’ graphene paper can afford quite high rate capability, and exhibit a high rate retention of 67.9 % when the scan rate increases from 3 to 1000 mV s^{-1} . These superior performances can be attributed to the three dimensional macroporous structure.

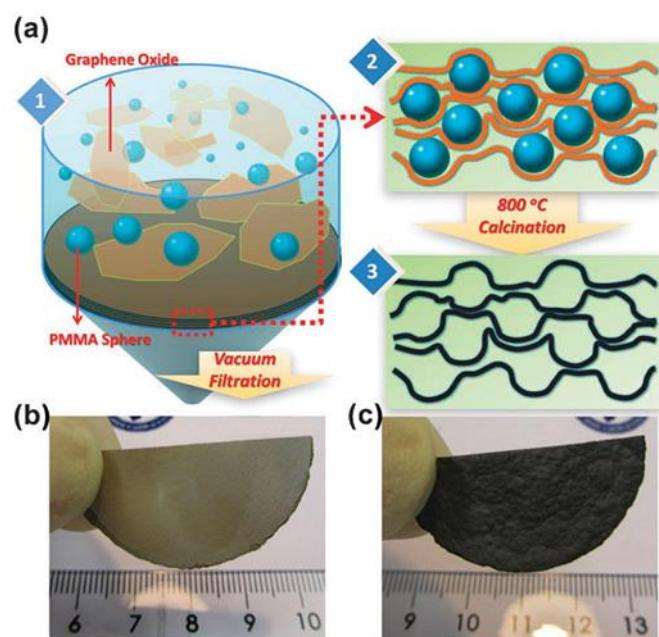


Figure 1.24 (a) An illustration of the fabrication of ‘bubble’ graphene paper and photos of (b) as-prepared GO/PMMA paper, (c) “bubble” graphene paper [111].

1.4.2.4 Flexible graphene composite electrodes

For supercapacitor applications, the capacitance of pure graphene film/paper is limited by its EDLC energy storage mechanism. The formation of a porous or loosely-compact structure with flexible graphene electrodes can effectively increase the capacitance/capacity gravimetrically, but deliver relatively low areal/volumetric capacitance/capacity due to low mass loading. A graphene electrode for LIB is also limited by its relatively low maximum theoretical capacity (748 mAh g^{-1}). To solve this issue, active materials with high capacity/capacitance such as transition metal oxides (TMOs) or conducting polymers are added to form composites in order to improve the performance. TMOs or conducting polymer can contribute large capacitance/capacity, while effectively prevent graphene sheets aggregation. In addition, an enhanced capacitance/capacity per areal/volume can be achieved due to the greater

areal/volumetric loading mass. On the other hand, the existence of graphene in the composites enables flexibility, and also improves the rate and cycle performance of TMOs or conducting polymers. Flexible electrodes combining TMOs or conducting polymers with graphene is anticipated to have excellent electrochemical performance as well as good mechanical properties.

Transition metal (Fe, Co, Ni, Sn) oxides (TMOs) have been widely studied as anode materials for their high theoretical lithium storage capacities ($> 600 \text{ mAh g}^{-1}$) [112-116]. In graphene/TMOs composite materials, graphene can serve as a conductive network and anchor for nanoparticles. The volume expansion and contraction of those materials during charge/discharge can be mitigated by graphene. On the other hand, the inorganic particles in the composites act as spacers to reduce the restacking of graphene sheets. So the composites have both high lithium storage capacity and excellent cycle stability. Wang *et al.* demonstrated a ternary surfactant directed self-assembly approach using graphene as building blocks to construct ordered flexible SnO_2 -graphene nanocomposite for lithium-ion battery application. This material presented a capacity of 760 mAh g^{-1} at 8 mA g^{-1} and 225 mAh g^{-1} at 80 mA g^{-1} . Other TMOs such as MnO_2 , TiO_2 and Co_3O_4 , were also employed to prepare flexible graphene based hybrid electrodes. Free-standing hybrid graphene- MnO_2 nanotube thin films were layer-by-layer assembled via an ultrafiltration technique (Figure 1.25). Graphene thin layers provided conductive pathways facilitating the conversion reaction of MnO_2 , and also maintained the electrical contact with MnO_2 nanotube during lithium insertion/de-insertion. The composite film presented excellent cycle performance and rate capability with a reversible capacity of 495 mAh g^{-1} at 100 mA g^{-1} after 40 cycles. At a high current rate of 1600 mA g^{-1} , the charge capacity of graphene- MnO_2 NT film reached 208 mAh g^{-1} [117].

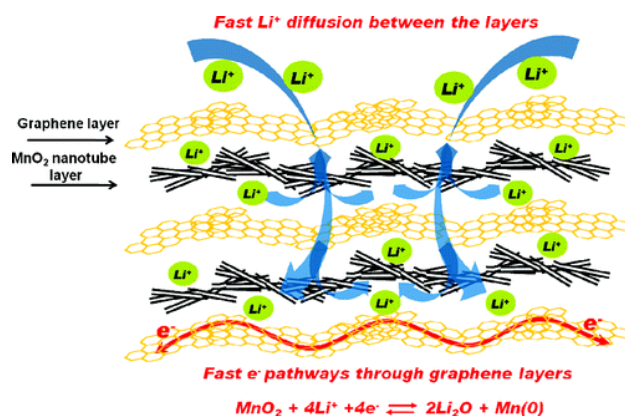


Figure 1.25 Schematic of Li storage mechanism of graphene-MnO₂ NT film as a LIB anode [117].

Flexible TMOs/graphene hybrid materials such as MnO₂/graphene, RuO₂/graphene, and V₂O₅/graphene have also been reported for supercapacitor applications. A simple strategy using the *in situ* grown MnO₂ nanoparticles decorated graphene oxide as precursor to prepare graphene/MnO₂ composite paper was reported. The specific capacitance of graphene/MnO₂ composite paper with 24 wt% MnO₂ reached 256 F g⁻¹ at a current density of 500 mA g⁻¹, and showed good cycle stability as well [118]. A similar method was also applied to fabricate V₂O₅ nanowires/graphene paper. The V₂O₅ nanowires (VNW) were *in situ* grown on the surface of GO sheets (Figure 1.26) [119]. Then the hybrid paper was fabricated by traditional filtration process followed by GO reduction. The composite electrode showed an energy density of 38.8 Wh kg⁻¹ at a power density of 455 W kg⁻¹. The maximum power density of 3.0 kW kg⁻¹ was delivered at a constant current discharge rate of 5.5 A g⁻¹. The device prepared using hGO-VNW₁₂₀ anode showed a specific capacitance of 80 F g⁻¹.

Although graphene-TMO based flexible electrodes have demonstrated their promising performance, there are still some limitations. These composites still

demonstrate relatively poor rate capability and cycle performance, although the performance had been improved compared with that of neat TMOs. Another drawback is the deteriorated mechanical strength of the flexible composite electrode induced by the incorporation of TMO powder/nanoparticles.

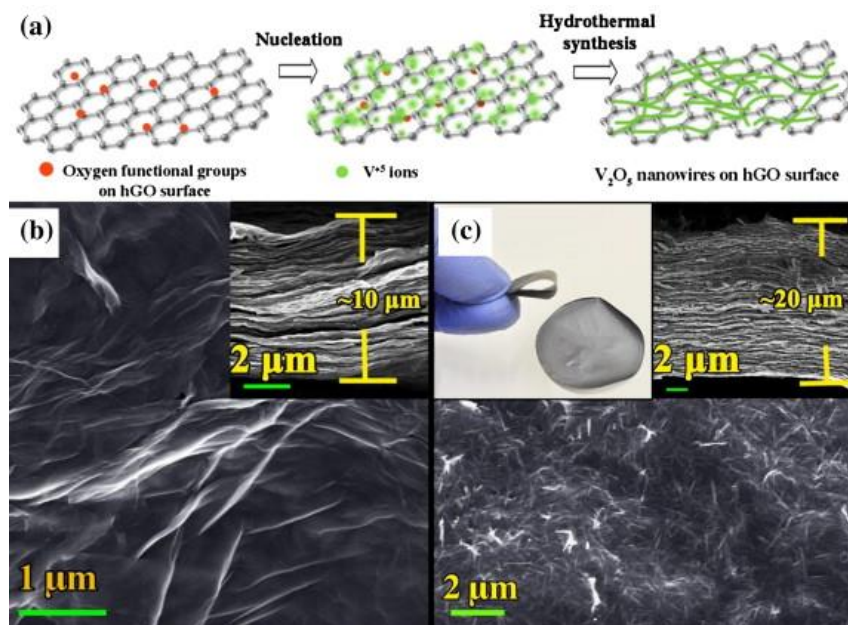


Figure 1.26 (a) A schematic diagram showing the formation of graphene/VNW composite; (b) SEM micrographs of the surface and cross-section of the graphene paper (inset); (c) Surface morphology of graphene/VNW composite paper. Inset shows a digital image and cross-sectional SEM image of the flexible freestanding graphene/VNW paper [119].

Other than graphene-TMO, graphene-conducting polymers composite films/papers are the more promising candidates for flexible electrodes. Combining graphene with conducting polymers, affords ability to obtain lightweight, high performance composite materials. The mechanical strength of composite materials can

also be enhanced with the introduction of conducting polymers. The biocompatibility of conducting polymers, also enable potential use for biomedical applications.

Polypyrrole (PPy), a low-cost, high-capacitance and environmentally stable conducting polymer, has been the subject of research for a supercapacitor or battery electrode for a considerable time. As a pseudocapacitance material, PPy stores and releases charges through redox processes associated with the π -conjugated polymer chains. It can provide a theoretical capacitance of up to 620 F g^{-1} (with 0.33 dopant level), and large volumetric capacitance of $400\text{-}500 \text{ F cm}^{-3}$ [44]. The properties of PPy can be further enhanced by forming composites between PPy and carbon materials such as graphene.

Flexible, uniform graphene-PPy composite film was created through a pulsed electropolymerization technique on the graphene paper substrate (Figure 1.27) [120]. The flexible electrode affords high performance benefiting from the pseudocapacitive contribution from PPy, while still maintaining the inherent flexibility of graphene papers. By adjusting the electropolymerization time, a high specific capacitance of 237 F g^{-1} was obtained for the composite electrode using a moderate deposition time of 120 sec. This flexible supercapacitor film exhibited a very high energy and power density of 33 Wh kg^{-1} and 1184 W kg^{-1} , respectively, at a scan rate of 0.01 V s^{-1} .

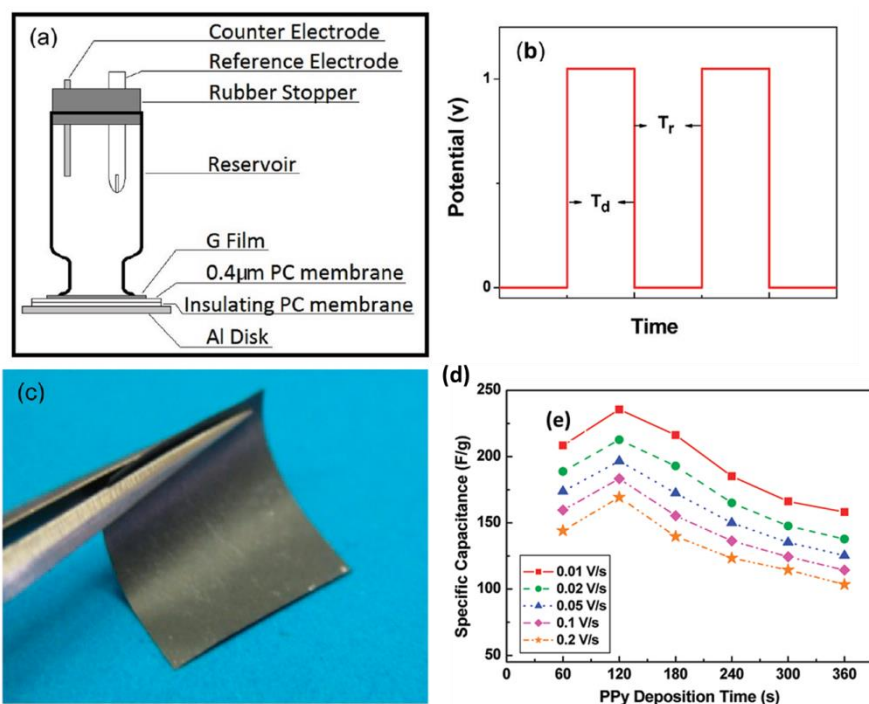


Figure 1.27 (a) Diagram of the apparatus used to deposit PPy on graphene paper and electrochemical testing. (b) Electrodeposition potential waveform used in the deposition. (c) Photographs showing the flexibility of graphene-PPy films [120].

Li *et al.* reported on a mechanically strong flexible rGO/PPy fibre paper prepared by a simple filtration method from a rGO and PPy fibre hybrid solution [121]. PPy fibres were uniformly distributed within the graphene sheets, creating enormous amount of pores for charge carrier storage/release. The mechanical strength of the composite paper was also enhanced by the interlayer distributed PPy nano-fibres. Such paper electrode can be assembled into a solid-state supercapacitor with polymer electrolyte polyvinyl alcohol-phosphate acid, to obtain a high capacitance of 345 F g^{-1} at 1 A g^{-1} and an excellent cycling stability (9.4% drop after 1000 cycles).

1.5 Thesis Objective

In summary, from the literature survey, free-standing graphene based flexible electrodes have shown great potential for application in flexible energy storage devices. However, the densely packed flexible graphene paper electrodes suffer from the restacking problem that occurred during the paper forming process, which leads to loss of effective surface area and limited ion transport, resulting in the deteriorated electrochemical performance. Fabricating flexible graphene-TMO electrodes can increase the capacity/capacitance. However, the performance of graphene-TMO composites under higher current rate or after long-term cycling is still unsatisfactory. Alternatively, construction of 3D structured flexible graphene macro-assemblies can effectively reduce the graphene restacking level, but deteriorate the mechanical strength. The existence of porosity leads to low areal loading mass, resulting in relatively low areal capacity/capacitance.

This thesis, therefore, aims to address the above stated problems by developing superior flexible graphene-based materials with 3D structure networks. Such materials are expected to combine excellent electrochemical performance with good mechanical strength. The improvement of areal capacitance is also a focus of attention, by making graphene-polypyrrole composite films. In addition, graphene obtained via directly solvent exfoliation from expanded graphite, other than commonly used graphite oxide exfoliation method, is also studied and used as building blocks for construction of flexible electrodes. Description of the experimental chapters in this thesis are given below.

Chapter 3 describes a graphene paper with porous structure prepared through pressing freeze-dried graphene cryogel originated from chemically reduced

graphene/graphene oxide hybrid dispersion precursor. Generally, graphene cryogel paper originated from pure graphene oxide precursor presents poor mechanical properties. To improve the mechanical properties, chemically reduced graphene (CRG) is introduced into the graphene oxide precursor solution. Since CRG have much less functional groups than GO, it can decrease the entrapped water content associated with H-bond during formation of the graphene cryogel. Lower water content in precursor cryogel leads to better H-bond networks in the formed paper, resulting in better mechanical strength. Such graphene cryogel paper demonstrates much higher capacity as a LIB anode, as well as the enhanced mechanical strength compared to pure reduced GO cryogel paper. However, mechanical pressing does result in partial loss of porous structure and, hence, performance. Therefore, an alternative approach to obtain porous structured graphene paper is reported in the next chapter (Chapter 4).

To avoid the partial loss of porous structure during mechanical pressing of graphene cryogel, the work in Chapter 4 further developed a novel approach to obtain porous structured graphene paper without pressing. Such graphene paper with interconnected porous structure is prepared by freeze-drying of a filtrated graphene oxide wet gel. The porous graphene paper has a similar porous network as freeze dried graphene aerogel, yet mechanically robust and flexible. The porous structure within the graphene paper can enable easier access for ions and electrolytes, leading to an improved electrochemical performance. The porous graphene paper based LIBs and all solid-state flexible SCs are studied and evaluated, demonstrating high capacity/capacitance.

The graphene based flexible electrodes prepared by this freeze drying method present promising gravimetric capacitance, but deliver a low areal capacitance due to

their low areal loading mass. Therefore, further work was done to address this problem, as reported in the next chapter (Chapter 5).

Chapter 5 demonstrates a novel flexible PPy/chemically reduced graphene (CRG) hybrid paper with an enhanced areal capacitance by electrochemical synthesis of PPy on paper-like CRG gel. The PPy is grown uniformly inside the paper-like graphene gel. It can effectively separate graphene sheets and also provide large pseudocapacitance that imparts to the obtained paper excellent electrochemical performance. With the increased areal loading mass, the flexible composite electrode is allowed to present higher areal capacitance.

The graphene used in our previous work originated from exfoliation of graphite oxide. Such method has its shortcomings including strong oxidative and corrosive reagent used, time-consuming procedure, and the graphene with defected structure produced. Surfactant assisted liquid phase exfoliation (LPE) can overcome the above disadvantages. However, the surfactant is difficult to be completely removed. Thus the obtained graphene from this dispersion demonstrates deteriorated electrochemical activities. To overcome these shortcomings mentioned above, Chapter 6 describes further work in the development of a tandem strategy to obtain flexible graphene/PPy nanofibre (PPyF) film electrode using graphene originated from surfactant assisted LPE. PPyF is synthesized directly in the exfoliated graphene (DEG)/surfactant dispersion using surfactant as the template. The PPyF benefits the forming of flexible film by binding the DEG platelets. It can also provide pseudocapacitance to the composite electrode. Electrochemical performances of such flexible DEG-PPyF film have then been optimized and studied.

1.6 References

- [1] F.R. Fan, L. Lin, G. Zhu, W.Z. Wu, R. Zhang, Z.L. Wang, Transparent Triboelectric Nanogenerators and Self-Powered Pressure Sensors Based on Micropatterned Plastic Films, *Nano Letters*, 12 (2012) 3109-3114.
- [2] M.K. Kwak, H.E. Jeong, K.Y. Suh, Rational Design and Enhanced Biocompatibility of a Dry Adhesive Medical Skin Patch, *Advanced Materials*, 23 (2011) 3949-3953.
- [3] D.J. Lipomi, M. Vosgueritchian, B.C.K. Tee, S.L. Hellstrom, J.A. Lee, C.H. Fox, Z.N. Bao, Skin-like Pressure and Strain Sensors based on Transparent Elastic Films of Carbon nanotubes, *Nature Nanotechnology*, 6 (2011) 788-792.
- [4] C. Pang, G.Y. Lee, T.I. Kim, S.M. Kim, H.N. Kim, S.H. Ahn, K.Y. Suh, A Flexible and Highly Sensitive Strain-gauge Sensor using Reversible Interlocking of Nanofibres, *Nature Materials*, 11 (2012) 795-801.
- [5] "LG G Flex Phones." from <http://www.lg.com/us/lg-g-flex-phones>.
- [6] "Plastic Logic's Flexible AMOLED Technology Wins Innovation Excellence Award." from http://www.opjournal.com/news/items/Plastic_Logics_flexible AMOLED technology wins Innovation Excellence Award.html.
- [7] "The PoloTech™ Shirt." from <http://www.ralphlauren.com/product/index.jsp?productId=69917696>.
- [8] "PowerFilm Solar Rollable Solar Panels." from <http://www.flexsolarcells.com/PowerFilm-Solar-Rollable-Solar-Panels.php>.
- [9] "LG Begins Mass Production of First Flexible, Plastic E-ink Displays." from <http://www.extremetech.com/electronics/124229-lg-begins-mass-production-of-flexible-plastic-e-ink-displays>.
- [10] C. Wang, G.G. Wallace, Flexible Electrodes and Electrolytes for Energy Storage, *Electrochimica Acta*, 175 (2015) 87-95.
- [11] P. Chen, H. Chen, J. Qiu, C. Zhou, Inkjet Printing of Single-Walled Carbon Nanotube/RuO₂ Nanowire Supercapacitors on Cloth Fabrics and Flexible Substrates, *Nano Res.*, 3 (2010) 594-603.
- [12] L. Yuan, B. Yao, B. Hu, K. Huo, W. Chen, J. Zhou, Polypyrrole-coated Paper for Flexible Solid-state Energy Storage, *Energy & Environmental Science*, 6 (2013) 470-476.

- [13] J. Chen, A.I. Minett, Y. Liu, C. Lynam, P. Sherrell, C. Wang, G.G. Wallace, Direct Growth of Flexible Carbon nanotube Electrodes, *Advanced Materials*, 20 (2008) 566-570.
- [14] D.Y. Choi, H.W. Kang, H.J. Sung, S.S. Kim, Annealing-free, Flexible Silver nanowire-polymer Composite Electrodes via a Continuous Two-step Spray-coating Method, *Nanoscale*, 5 (2013) 977-983.
- [15] F. Carpi, D. De Rossi, Electroactive Polymer-based Devices for E-textiles in Biomedicine, *Information Technology in Biomedicine, IEEE Transactions on*, 9 (2005) 295-318.
- [16] M.T. Byrne, Y.K. Gun'ko, Recent Advances in Research on Carbon Nanotube–Polymer Composites, *Advanced Materials*, 22 (2010) 1672-1688.
- [17] Q. Wu, Y. Xu, Z. Yao, A. Liu, G. Shi, Supercapacitors Based on Flexible Graphene/Polyaniline Nanofiber Composite Films, *ACS Nano*, 4 (2010) 1963-1970.
- [18] L. Nyholm, G. Nyström, A. Mihranyan, M. Strømme, Toward Flexible Polymer and Paper-Based Energy Storage Devices, *Advanced Materials*, 23 (2011) 3751-3769.
- [19] H.K. Song, G.T.R. Palmore, Redox-Active Polypyrrole: Toward Polymer-Based Batteries, *Advanced Materials*, 18 (2006) 1764-1768.
- [20] D.R. Linden, Thomas B., *Handbook of Batteries*, McGraw-Hill, New York 2002.
- [21] D.R. Linden, Thomas B., *Handbook of Batteries*, McGraw-Hill, New York 2002, pp. 35.34.
- [22] L.L. Zhang, R. Zhou, X.S. Zhao, Graphene-based Materials as Supercapacitor Electrodes, *Journal of Materials Chemistry*, 20 (2010) 5983-5992.
- [23] M.B. Lu, Francois; Frackowiak, Elzbieta, *New Materials for Sustainable Energy and Development : Supercapacitors*, John Wiley & Sons, Somerset, NJ, USA, 2013.
- [24] M. Winter, R.J. Brodd, What Are Batteries, Fuel Cells, and Supercapacitors?, *Chemical Reviews*, 104 (2004) 4245-4270.
- [25] D. Antiohos, *Nanostructured Carbon Electrodes*, School of Chemistry, University of Wollongong, 2013.
- [26] S. Zhang, N. Pan, Supercapacitors Performance Evaluation, *Advanced Energy Materials*, 5 (2015) 1401401 (1-19).
- [27] P.L. Taberna, P. Simon, J.F. Fauvarque *Electrochemical Characteristics and Impedance Spectroscopy Studies of Carbon-Carbon Supercapacitors*, *Journal of The Electrochemical Society*, 150 (2003) A292-A300.

- [28] J.B. Goodenough, K. Mizushima, Fast Ion Conductors, Google Patents, 1982.
- [29] J.B. Goodenough, K. Mizuchima, Electrochemical Cell with New Fast Ion Conductors, Google Patents, 1981.
- [30] Y.-C. Chang, H.-J. Sohn, C.-H. Ku, Y.-G. Wang, Y. Korai, I. Mochida, Anodic Performances of Mesocarbon Microbeads (MCMB) Prepared from Synthetic Naphthalene Isotropic Pitch, *Carbon*, 37 (1999) 1285-1297.
- [31] J.-K. Park, Anode Materials, Principles and Applications of Lithium Secondary Batteries, Wiley-VCH Verlag GmbH & Co. KGaA2012, pp. 89-139.
- [32] P.G. Bruce, B. Scrosati, J.-M. Tarascon, Nanomaterials for Rechargeable Lithium Batteries, *Angewandte Chemie International Edition*, 47 (2008) 2930-2946.
- [33] C. Liu, F. Li, L.-P. Ma, H.-M. Cheng, Advanced Materials for Energy Storage, *Advanced Materials*, 22 (2010) E28-E62.
- [34] M. Winter, J.O. Besenhard, M.E. Spahr, P. Novák, Insertion Electrode Materials for Rechargeable Lithium Batteries, *Advanced Materials*, 10 (1998) 725-763.
- [35] J.R. Dahn, Phase-Diagram of Li_xC_6 , *Physical Review B*, 44 (1991) 9170-9177.
- [36] W. Xing, R.A. Dunlap, J.R. Dahn, Studies of Lithium Insertion in Ballmilled Sugar Carbons, *Journal of The Electrochemical Society*, 145 (1998) 62-70.
- [37] Y. Jung, M.C. Suh, S.C. Shim, J. Kwak, Lithium Insertion into Disordered Carbons Prepared from Organic Polymers, *Journal of The Electrochemical Society*, 145 (1998) 3123-3129.
- [38] W. Xing, J.R. Dahn, Study of Irreversible Capacities for Li Insertion in Hard and Graphitic Carbons, *Journal of the Electrochemical Society*, 144 (1997) 1195-1201.
- [39] M. Winter, J.O. Besenhard, Electrochemical Lithiation of Tin and Tin-based Intermetallics and Composites, *Electrochimica Acta*, 45 (1999) 31-50.
- [40] W.-J. Zhang, A Review of the Electrochemical Performance of Alloy Anodes for Lithium-ion Batteries, *Journal of Power Sources*, 196 (2011) 13-24.
- [41] X.-L. Wu, Y.-G. Guo, L.-J. Wan, Rational Design of Anode Materials Based on Group IVA Elements (Si, Ge, and Sn) for Lithium-Ion Batteries, *Chemistry – An Asian Journal*, 8 (2013) 1948-1958.
- [42] V. Ruiz, R. Santamaría, M. Granda, C. Blanco, Long-term Cycling of Carbon-based Supercapacitors in Aqueous Media, *Electrochimica Acta*, 54 (2009) 4481-4486.

- [43] Y.J. Lee, J.C. Jung, J. Yi, S.-H. Baeck, J.R. Yoon, I.K. Song, Preparation of Carbon Aerogel in Ambient Conditions for Electrical Double-layer Capacitor, *Current Applied Physics*, 10 (2010) 682-686.
- [44] G.A. Snook, P. Kao, A.S. Best, Conducting-polymer-based Supercapacitor Devices and Electrodes, *Journal of Power Sources*, 196 (2011) 1-12.
- [45] G.A. Snook, G.Z. Chen, The Measurement of Specific Capacitances of Conducting Polymers using the Quartz Crystal Microbalance, *Journal of Electroanalytical Chemistry*, 612 (2008) 140-146.
- [46] V. Gupta, N. Miura, Electrochemically Deposited Polyaniline Nanowire's Network: A High-Performance Electrode Material for Redox Supercapacitor, *Electrochemical and Solid-State Letters*, 8 (2005) A630-A632.
- [47] L. Ran, C. Seung Il, L. Sang Bok, Poly(3,4-ethylenedioxythiophene) Nanotubes as Electrode Materials for a High-powered Supercapacitor, *Nanotechnology*, 19 (2008) 215710 (1-8).
- [48] K. Wang, J. Huang, Z. Wei, Conducting Polyaniline Nanowire Arrays for High Performance Supercapacitors, *The Journal of Physical Chemistry C*, 114 (2010) 8062-8067.
- [49] J.S. Kwon, B.C. Kim, G.G. Wallace, J.H. Park, S.H. Kim, J.M. Ko, H. Ahn, Nafion-Doped Polypyrrole as a Supercapacitor Electrode in Ionic Liquid, *Molecular Crystals and Liquid Crystals*, 520 (2010) 262-266.
- [50] Y. Hernandez, V. Nicolosi, M. Lotya, F.M. Blighe, Z. Sun, S. De, I.T. McGovern, B. Holland, M. Byrne, Y.K. Gun'Ko, J.J. Boland, P. Niraj, G. Duesberg, S. Krishnamurthy, R. Goodhue, J. Hutchison, V. Scardaci, A.C. Ferrari, J.N. Coleman, High-yield Production of Graphene by Liquid-phase Exfoliation of Graphite, *Nat Nano*, 3 (2008) 563-568.
- [51] C.-C. Hu, W.-C. Chen, Effects of Substrates on the Capacitive Performance of $\text{RuO}_x \cdot n\text{H}_2\text{O}$ and Activated Carbon- RuO_x Electrodes for Supercapacitors, *Electrochimica Acta*, 49 (2004) 3469-3477.
- [52] J.P. Zheng, P.J. Cygan, T.R. Jow, Hydrous Ruthenium Oxide as an Electrode Material for Electrochemical Capacitors, *Journal of The Electrochemical Society*, 142 (1995) 2699-2703.
- [53] G.-W. Yang, C.-L. Xu, H.-L. Li, Electrodeposited Nickel Hydroxide on Nickel Foam with Ultrahigh Capacitance, *Chemical Communications*, (2008) 6537-6539.

- [54] S.C. Pang, M.A. Anderson, T.W. Chapman, Novel Electrode Materials for Thin - Film Ultracapacitors: Comparison of Electrochemical Properties of Sol - Gel - Derived and Electrodeposited Manganese Dioxide, *Journal of The Electrochemical Society*, 147 (2000) 444-450.
- [55] J. Chen, K. Huang, S. Liu, Hydrothermal Preparation of Octadecahedron Fe₃O₄ Thin Film for use in an Electrochemical Supercapacitor, *Electrochimica Acta*, 55 (2009) 1-5.
- [56] W.-J. Zhou, M.-W. Xu, D.-D. Zhao, C.-L. Xu, H.-L. Li, Electrodeposition and Characterization of Ordered Mesoporous Cobalt Hydroxide Films on Different Substrates for Supercapacitors, *Microporous and Mesoporous Materials*, 117 (2009) 55-60.
- [57] M. Toupin, T. Brousse, D. Bélanger, Influence of Microstructure on the Charge Storage Properties of Chemically Synthesized Manganese Dioxide, *Chemistry of Materials*, 14 (2002) 3946-3952.
- [58] E. Frackowiak, F. Béguin, Carbon Materials for the Electrochemical Storage of Energy in Capacitors, *Carbon*, 39 (2001) 937-950.
- [59] S.V. Morozov, K.S. Novoselov, M.I. Katsnelson, F. Schedin, D.C. Elias, J.A. Jaszczak, A.K. Geim, Giant Intrinsic Carrier Mobilities in Graphene and Its Bilayer, *Physical Review Letters*, 100 (2008) 016602 (1-4).
- [60] A. Peigney, C. Laurent, E. Flahaut, R.R. Bacsa, A. Rousset, Specific Surface Area of Carbon nanotubes and Bundles of Carbon nanotubes, *Carbon*, 39 (2001) 507-514.
- [61] J.C. Shelton, H.R. Patil, J.M. Blakely, Equilibrium Segregation of Carbon to a Nickel (111) Surface-surface Phase-transition, *Surface Science*, 43 (1974) 493-520.
- [62] K.S. Novoselov, A.K. Geim, S.V. Morozov, D. Jiang, Y. Zhang, S.V. Dubonos, I.V. Grigorieva, A.A. Firsov, Electric Field Effect in Atomically Thin Carbon Films, *Science*, 306 (2004) 666-669.
- [63] C. Berger, Z. Song, X. Li, X. Wu, N. Brown, C. Naud, D. Mayou, T. Li, J. Hass, A.N. Marchenkov, E.H. Conrad, P.N. First, W.A. de Heer, Electronic Confinement and Coherence in Patterned Epitaxial Graphene, *Science*, 312 (2006) 1191-1196.
- [64] H. Tetlow, J. Posthuma de Boer, I.J. Ford, D.D. Vvedensky, J. Coraux, L. Kantorovich, Growth of Epitaxial Graphene: Theory and Experiment, *Physics Reports*, 542 (2014) 195-295.

- [65] X. Li, W. Cai, J. An, S. Kim, J. Nah, D. Yang, R. Piner, A. Velamakanni, I. Jung, E. Tutuc, S.K. Banerjee, L. Colombo, R.S. Ruoff, Large-Area Synthesis of High-Quality and Uniform Graphene Films on Copper Foils, *Science*, 324 (2009) 1312-1314.
- [66] W. Cai, R. Piner, Y. Zhu, X. Li, Z. Tan, H. Floresca, C. Yang, L. Lu, M.J. Kim, R. Ruoff, Synthesis of Isotopically-labeled Graphite Films by Cold-wall Chemical Vapor Deposition and Electronic Properties of Graphene Obtained from such Films, *Nano Res.*, 2 (2009) 851-856.
- [67] S. Chen, W. Cai, R.D. Piner, J.W. Suk, Y. Wu, Y. Ren, J. Kang, R.S. Ruoff, Synthesis and Characterization of Large-Area Graphene and Graphite Films on Commercial Cu–Ni Alloy Foils, *Nano Letters*, 11 (2011) 3519-3525.
- [68] A. Ciesielski, P. Samori, Graphene via Sonication Assisted Liquid-phase Exfoliation, *Chemical Society Reviews*, 43 (2014) 381-398.
- [69] M. Lotya, Y. Hernandez, P.J. King, R.J. Smith, V. Nicolosi, L.S. Karlsson, F.M. Blighe, S. De, Z. Wang, I.T. McGovern, G.S. Duesberg, J.N. Coleman, Liquid Phase Production of Graphene by Exfoliation of Graphite in Surfactant/Water Solutions, *Journal of the American Chemical Society*, 131 (2009) 3611-3620.
- [70] S.M. Notley, Highly Concentrated Aqueous Suspensions of Graphene through Ultrasonic Exfoliation with Continuous Surfactant Addition, *Langmuir*, 28 (2012) 14110-14113.
- [71] W.S. Hummers, R.E. Offeman, Preparation of Graphitic Oxide, *Journal of the American Chemical Society*, 80 (1958) 1339-1339.
- [72] T. Nakajima, Y. Matsuo, Formation Process and Structure of Graphite Oxide, *Carbon*, 32 (1994) 469-475.
- [73] H. He, J. Klinowski, M. Forster, A. Lerf, A New Structural Model for Graphite Oxide, *Chemical Physics Letters*, 287 (1998) 53-56.
- [74] S. Stankovich, D.A. Dikin, G.H.B. Dommett, K.M. Kohlhaas, E.J. Zimney, E.A. Stach, R.D. Piner, S.T. Nguyen, R.S. Ruoff, Graphene-based Composite Materials, *Nature*, 442 (2006) 282-286.
- [75] S. Stankovich, D.A. Dikin, R.D. Piner, K.A. Kohlhaas, A. Kleinhammes, Y. Jia, Y. Wu, S.T. Nguyen, R.S. Ruoff, Synthesis of Graphene-based Nanosheets via Chemical Reduction of Exfoliated Graphite Oxide, *Carbon*, 45 (2007) 1558-1565.
- [76] J. Zhang, H. Yang, G. Shen, P. Cheng, J. Zhang, S. Guo, Reduction of Graphene Oxide via L-ascorbic Acid, *Chemical Communications*, 46 (2010) 1112-1114.

- [77] H.-J. Shin, K.K. Kim, A. Benayad, S.-M. Yoon, H.K. Park, I.-S. Jung, M.H. Jin, H.-K. Jeong, J.M. Kim, J.-Y. Choi, Y.H. Lee, Efficient Reduction of Graphite Oxide by Sodium Borohydride and Its Effect on Electrical Conductance, *Advanced Functional Materials*, 19 (2009) 1987-1992.
- [78] M.J. McAllister, J.-L. Li, D.H. Adamson, H.C. Schniepp, A.A. Abdala, J. Liu, M. Herrera-Alonso, D.L. Milius, R. Car, R.K. Prud'homme, I.A. Aksay, Single Sheet Functionalized Graphene by Oxidation and Thermal Expansion of Graphite, *Chemistry of Materials*, 19 (2007) 4396-4404.
- [79] R.S. Sundaram, C. Gómez-Navarro, K. Balasubramanian, M. Burghard, K. Kern, Electrochemical Modification of Graphene, *Advanced Materials*, 20 (2008) 3050-3053.
- [80] M. Zhou, Y. Wang, Y. Zhai, J. Zhai, W. Ren, F. Wang, S. Dong, Controlled Synthesis of Large-Area and Patterned Electrochemically Reduced Graphene Oxide Films, *Chemistry – A European Journal*, 15 (2009) 6116-6120.
- [81] D. Pan, S. Wang, B. Zhao, M. Wu, H. Zhang, Y. Wang, Z. Jiao, Li Storage Properties of Disordered Graphene Nanosheets, *Chemistry of Materials*, 21 (2009) 3136-3142.
- [82] K. Sato, M. Noguchi, A. Demachi, N. Oki, M. Endo, A Mechanism of Lithium Storage in Disordered Carbons, *Science*, 264 (1994) 556-558.
- [83] E. Yoo, J. Kim, E. Hosono, H.-s. Zhou, T. Kudo, I. Honma, Large Reversible Li Storage of Graphene Nanosheet Families for Use in Rechargeable Lithium Ion Batteries, *Nano Letters*, 8 (2008) 2277-2282.
- [84] P. Guo, H. Song, X. Chen, Electrochemical Performance of Graphene Nanosheets as Anode Material for Lithium-ion Batteries, *Electrochemistry Communications*, 11 (2009) 1320-1324.
- [85] G. Wang, X. Shen, J. Yao, J. Park, Graphene Nanosheets for Enhanced Lithium Storage in Lithium ion Batteries, *Carbon*, 47 (2009) 2049-2053.
- [86] Y.-P. Wu, C.-R. Wan, C.-Y. Jiang, S.-B. Fang, Y.-Y. Jiang, Mechanism of Lithium Storage in Low Temperature Carbon, *Carbon*, 37 (1999) 1901-1908.
- [87] J. Xia, F. Chen, J. Li, N. Tao, Measurement of the Quantum Capacitance of Graphene, *Nat Nano*, 4 (2009) 505-509.
- [88] M.D. Stoller, S. Park, Y. Zhu, J. An, R.S. Ruoff, Graphene-Based Ultracapacitors, *Nano Letters*, 8 (2008) 3498-3502.

- [89] F.C. Wu, R.L. Tseng, C.C. Hu, C.C. Wang, The Capacitive Characteristics of Activated Carbons - Comparisons of the Activation Methods on the Pore Structure and Effects of the Pore Structure and Electrolyte on the Capacitive Performance, *Journal of Power Sources*, 159 (2006) 1532-1542.
- [90] Y.W. Zhu, S. Murali, M.D. Stoller, K.J. Ganesh, W.W. Cai, P.J. Ferreira, A. Pirkle, R.M. Wallace, K.A. Cychosz, M. Thommes, D. Su, E.A. Stach, R.S. Ruoff, Carbon-Based Supercapacitors Produced by Activation of Graphene, *Science*, 332 (2011) 1537-1541.
- [91] Y. He, W. Chen, C. Gao, J. Zhou, X. Li, E. Xie, An Overview of Carbon Materials for Flexible Electrochemical Capacitors, *Nanoscale*, 5 (2013) 8799-8820.
- [92] A. Yu, I. Roes, A. Davies, Z. Chen, Ultrathin, Transparent, and Flexible Graphene Films for Supercapacitor Application, *Applied Physics Letters*, 96 (2010) 253105 (1-3).
- [93] X. Dong, L. Wang, D. Wang, C. Li, J. Jin, Layer-by-Layer Engineered Co–Al Hydroxide Nanosheets/Graphene Multilayer Films as Flexible Electrode for Supercapacitor, *Langmuir*, 28 (2012) 293-298.
- [94] W.-w. Liu, X.-b. Yan, J.-w. Lang, C. Peng, Q.-j. Xue, Flexible and Conductive Nanocomposite Electrode based on Graphene Sheets and Cotton Cloth for Supercapacitor, *Journal of Materials Chemistry*, 22 (2012) 17245-17253.
- [95] J. Ge, H.-B. Yao, W. Hu, X.-F. Yu, Y.-X. Yan, L.-B. Mao, H.-H. Li, S.-S. Li, S.-H. Yu, Facile Dip Coating Processed Graphene/MnO₂ Nanostructured Sponges as High Performance Supercapacitor Electrodes, *Nano Energy*, 2 (2013) 505-513.
- [96] Z. Weng, Y. Su, D.-W. Wang, F. Li, J. Du, H.-M. Cheng, Graphene–Cellulose Paper Flexible Supercapacitors, *Advanced Energy Materials*, 1 (2011) 917-922.
- [97] D. Wei, S. Haque, P. Andrew, J. Kivioja, T. Ryhanen, A. Pesquera, A. Centeno, B. Alonso, A. Chuvilin, A. Zurutuza, Ultrathin Rechargeable All-solid-state Batteries based on Monolayer Graphene, *Journal of Materials Chemistry A*, 1 (2013) 3177-3181.
- [98] D.A. Dikin, S. Stankovich, E.J. Zimney, R.D. Piner, G.H.B. Dommett, G. Evmenenko, S.T. Nguyen, R.S. Ruoff, Preparation and Characterization of Graphene Oxide Paper, *Nature*, 448 (2007) 457-460.
- [99] H. Chen, M.B. Müller, K.J. Gilmore, G.G. Wallace, D. Li, Mechanically Strong, Electrically Conductive, and Biocompatible Graphene Paper, *Advanced Materials*, 20 (2008) 3557-3561.

- [100] C. Wang, D. Li, C.O. Too, G.G. Wallace, Electrochemical Properties of Graphene Paper Electrodes Used in Lithium Batteries, *Chemistry of Materials*, 21 (2009) 2604-2606.
- [101] A. Abouimrane, O.C. Compton, K. Amine, S.T. Nguyen, Non-Annealed Graphene Paper as a Binder-Free Anode for Lithium-Ion Batteries, *The Journal of Physical Chemistry C*, 114 (2010) 12800-12804.
- [102] X. Zhao, C.M. Hayner, M.C. Kung, H.H. Kung, Flexible Holey Graphene Paper Electrodes with Enhanced Rate Capability for Energy Storage Applications, *ACS Nano*, 5 (2011) 8739-8749.
- [103] X. Yang, L. Qiu, C. Cheng, Y. Wu, Z.-F. Ma, D. Li, Ordered Gelation of Chemically Converted Graphene for Next-Generation Electroconductive Hydrogel Films, *Angewandte Chemie International Edition*, 50 (2011) 7325-7328.
- [104] X. Yang, C. Cheng, Y. Wang, L. Qiu, D. Li, Liquid-Mediated Dense Integration of Graphene Materials for Compact Capacitive Energy Storage, *Science*, 341 (2013) 534-537.
- [105] M.F. El-Kady, V. Strong, S. Dubin, R.B. Kaner, Laser Scribing of High-Performance and Flexible Graphene-Based Electrochemical Capacitors, *Science*, 335 (2012) 1326-1330.
- [106] F. Liu, S. Song, D. Xue, H. Zhang, Folded Structured Graphene Paper for High Performance Electrode Materials, *Advanced Materials*, 24 (2012) 1089-1094.
- [107] S. Yin, Y. Zhang, J. Kong, C. Zou, C.M. Li, X. Lu, J. Ma, F.Y.C. Boey, X. Chen, Assembly of Graphene Sheets into Hierarchical Structures for High-Performance Energy Storage, *ACS Nano*, 5 (2011) 3831-3838.
- [108] Z. Niu, J. Chen, H.H. Hng, J. Ma, X. Chen, A Leavening Strategy to Prepare Reduced Graphene Oxide Foams, *Advanced Materials*, 24 (2012) 4144-4150.
- [109] U.N. Maiti, J. Lim, K.E. Lee, W.J. Lee, S.O. Kim, Three-Dimensional Shape Engineered, Interfacial Gelation of Reduced Graphene Oxide for High Rate, Large Capacity Supercapacitors, *Advanced Materials*, 26 (2014) 615-619.
- [110] Y. Xu, K. Sheng, C. Li, G. Shi, Self-Assembled Graphene Hydrogel via a One-Step Hydrothermal Process, *ACS Nano*, 4 (2010) 4324-4330.
- [111] C.-M. Chen, Q. Zhang, C.-H. Huang, X.-C. Zhao, B.-S. Zhang, Q.-Q. Kong, M.-Z. Wang, Y.-G. Yang, R. Cai, D. Sheng Su, Macroporous 'bubble' graphene film via

template-directed ordered-assembly for high rate supercapacitors, *Chemical Communications*, 48 (2012) 7149-7151.

[112] X. Wang, L.J. Yu, X.L. Wu, F.L. Yuan, Y.G. Guo, Y. Ma, J.N. Yao, Synthesis of Single-Crystalline Co_3O_4 Octahedral Cages with Tunable Surface Aperture and Their Lithium Storage Properties, *Journal of Physical Chemistry C*, 113 (2009) 15553-15558.

[113] M.Y. Cheng, B.J. Hwang, Mesoporous Carbon-encapsulated NiO Nanocomposite Negative Electrode Materials for High-rate Li-ion Battery, *Journal of Power Sources*, 195 (2010) 4977-4983.

[114] H.S. Kim, Y. Piao, S.H. Kang, T. Hyeon, Y.E. Sung, Uniform Hematite Nanocapsules based on an Anode Material for Lithium-ion Batteries, *Electrochemistry Communications*, 12 (2010) 382-385.

[115] L.S. Zhang, L.Y. Jiang, H.J. Yan, W.D. Wang, W. Wang, W.G. Song, Y.G. Guo, L.J. Wan, Mono Dispersed SnO_2 Nanoparticles on Both Sides of Single Layer Graphene Sheets as Anode Materials in Li-ion Batteries, *Journal of Materials Chemistry*, 20 (2010) 5462-5467.

[116] J.C. Park, J. Kim, H. Kwon, H. Song, Gram-Scale Synthesis of Cu_2O Nanocubes and Subsequent Oxidation to CuO Hollow Nanostructures for Lithium-Ion Battery Anode Materials, *Advanced Materials*, 21 (2009) 803-807.

[117] A. Yu, H.W. Park, A. Davies, D.C. Higgins, Z. Chen, X. Xiao, Free-Standing Layer-By-Layer Hybrid Thin Film of Graphene- MnO_2 Nanotube as Anode for Lithium Ion Batteries, *The Journal of Physical Chemistry Letters*, 2 (2011) 1855-1860.

[118] Z. Li, Y. Mi, X. Liu, S. Liu, S. Yang, J. Wang, Flexible Graphene/ MnO_2 Composite Papers for Supercapacitor Electrodes, *Journal of Materials Chemistry*, 21 (2011) 14706-14711.

[119] S.D. Perera, A.D. Liyanage, N. Nijem, J.P. Ferraris, Y.J. Chabal, K.J. Balkus Jr, Vanadium Oxide Nanowire – Graphene Binder Free Nanocomposite Paper Electrodes for Supercapacitors: A Facile Green Approach, *Journal of Power Sources*, 230 (2013) 130-137.

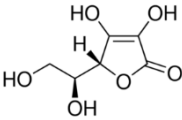
[120] A. Davies, P. Audette, B. Farrow, F. Hassan, Z. Chen, J.-Y. Choi, A. Yu, Graphene-Based Flexible Supercapacitors: Pulse-Electropolymerization of Polypyrrole on Free-Standing Graphene Films, *The Journal of Physical Chemistry C*, 115 (2011) 17612-17620.

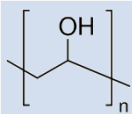
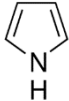
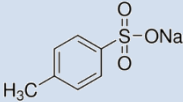
[121] S. Li, C. Zhao, K. Shu, C. Wang, Z. Guo, G.G. Wallace, H. Liu, Mechanically Strong High Performance Layered Polypyrrole Nano fibre/graphene Film for Flexible Solid State Supercapacitor, *Carbon*, 79 (2014) 554-562.

2 Experimental

2.1 List of Chemical Reagents and Materials

Chemicals and reagents used in this work are listed below. They were used as received unless otherwise stated.

Reagents/Materials	Formula	Grade/batch	Supplier
Ammonium persulfate	$K_2S_2O_8$	Analytical	Ajax Finechem
Ammonia solution	$NH_3 \cdot H_2O$	Analytical, 28%	Ajax Finechem
Cetrimonium bromide	$H_3C(H_2C)_{15}-\overset{\overset{CH_3}{ }}{N^+}-CH_3$ Br^-	Analytical	Thermofisher
Electrolyte for lithium-ion batteries	1 M $LiPF_6$ in EC/DMC	---	Guotai-Huarong New Chemical
Expandable graphite flake	C	Analytical, 3772	Asbury Carbon
Graphite	C	Analytical	Fluka
Hydrazine hydrate	$N_2H_4 \cdot xH_2O$	Analytical, 50-60 %	Sigma-Aldrich
Hydrochloric acid	HCl	Analytical, 32%	Ajax Finechem
Hydrogen peroxide	H_2O_2	Analytical, 30 %	Ajax Finechem
L-ascorbic acid		Analytical	Alfa Aesar
Lithium foil	Li	---	Ganfeng Lithium
Lithium sulfate	$Li_2SO_4 \cdot H_2O$	Analytical, monohydrate	Sigma-Aldrich
Phosphorus pentoxide	P_2O_5	Analytical	Sigma

Polycarbonate membrane filter	---	0.22 μm , \varnothing 47/92 mm	Merck Millipore
Poly(vinyl alcohol)		Analytical, MW 85, 000-124, 000	Sigma
Potassium permanganate	KMnO_4	Analytical	Chem Supply
Potassium persulfate	$\text{K}_2\text{S}_2\text{O}_8$	Analytical	Sigma-Aldrich
Pyrrole		Analytical, distilled	Sigma-Aldrich
Sodium p-toluenesulfonate		Analytical	Sigma-Aldrich
Sulfuric acid	H_2SO_4	Analytical, 98%	Chem Supply

2.2 General Synthesis and Device Assembly

2.2.1 Synthesis of graphene oxide

Graphite oxide was synthesized from natural graphite flakes by the modified Hummers method following the procedures as described below [1, 2]. The first step was pre-oxidation of graphite. $\text{K}_2\text{S}_2\text{O}_8$ (2.5 g) and P_2O_5 (2.5 g) were dissolved into concentrated H_2SO_4 (98%, 12 mL) and heated to 80 °C. After P_2O_5 was fully dissolved to form a clear solution, graphite powder (3 g) was added and stirred for 4.5 h at 80 °C. The formed mixture was cooled down to room temperature and diluted with deionised (DI) water (0.5 L) and left overnight. Then the mixture was filtered and the filter cake was washed several times with DI water. The obtained product was dried in a vacuum oven at 70 °C overnight.

Subsequently, concentrated H₂SO₄ (120 mL) was firstly cooled to ~0 °C in an ice-water bath, then the as-prepared pre-oxidized graphite was added. After graphite was well dispersed, KMnO₄ (15 g) was gradually added under stirring, with temperature of mixture solution controlled below 20 °C. The oxidation of graphite was proceeded with stirring at 35 °C for 2h, then DI water (250 mL) was added with temperature controlled lower than 40 °C. This reaction mixture was left for another 2h, followed by addition of DI water (0.7 L). The 30 % H₂O₂ (20 mL) was added into the above diluted solution, and the colour of the mixture turned to bright yellow along with bubbling. After filtration, the filter cake was washed with HCl aqueous solution (1:10) to remove metal oxide residues. The resulting graphite oxide was dried in a vacuum oven at 50 °C overnight to evaporate HCl, then re-dispersed in water for dialysis for one week to remove the residual HCl and metal ions contained. Exfoliation of graphite oxide to graphene oxide (GO) was achieved by ultrasonication of the dispersion using a Branson Digital Sonifier for 30 min (2s on, 1s off, 30 % amplitude). The concentration of the obtained GO dispersion can be confirmed by measuring the weight of GO from the dried solution of a known volume.

2.2.2 Preparation of stable aqueous CRG solution

In this thesis, reduced graphene oxide obtained through wet chemical reduction method is named as chemically reduced graphene (CRG), while rGO refers to reduced graphene oxide obtained from thermal reduction. CRG aqueous solution was prepared by reduction of GO solution using hydrazine in the presence of ammonia solution, [3] and it is described briefly as follows. Ammonium solution (28 wt%, 168 μL) and hydrazine hydrate (138 μL) were added into 1.5 mg mL⁻¹ GO dispersion (40 mL) while

stirring. The resultant mixture was then stirred at 95°C for 1h to complete the reduction. The as-prepared CRG solution was diluted to give 1 mg mL⁻¹ and 0.4 mg mL⁻¹ solutions.

2.2.3 Fabrication of graphene paper/wet gel

The GO or CRG paper was formed by vacuum assisted filtration through polycarbonate membrane filter (pore size 0.22 μm, diameter 47 or 92 mm) (Figure 2.1) [4, 5]. The self-assembly of graphene sheets is driven by the force balance between the electrostatic repulsion and inter-planar interactions within graphene sheets [6]. Free-standing GO or CRG paper can be easily peeled off after drying. The paper-like graphene wet gel can also be prepared via filtration by terminating the process when a small amount of water remained on the gel surface [7].

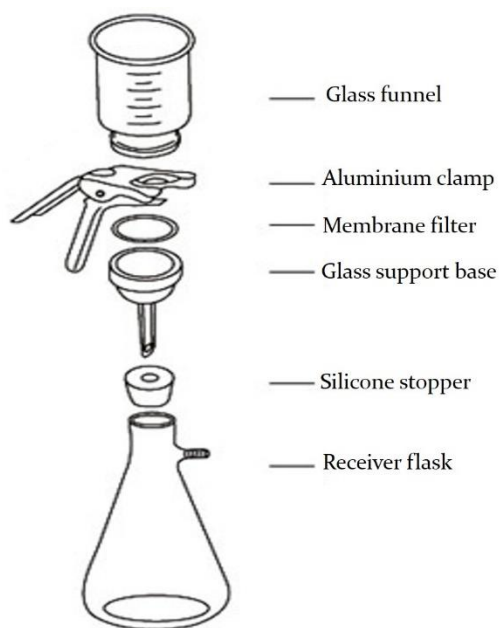


Figure 2.1 Schematic of a filtration set for making graphene paper/wet gel.

2.2.4 Electrochemical deposition of polypyrrole

Electrochemical deposition was carried out in aqueous solution using a standard three-electrode system, which consists of a working electrode (conductive substrates), counter electrode (platinum or stainless steel mesh) and reference electrode (Ag/AgCl reference electrode) (Figure 2.2). The polymerization can occur under constant applied current/potential or dynamic potential.

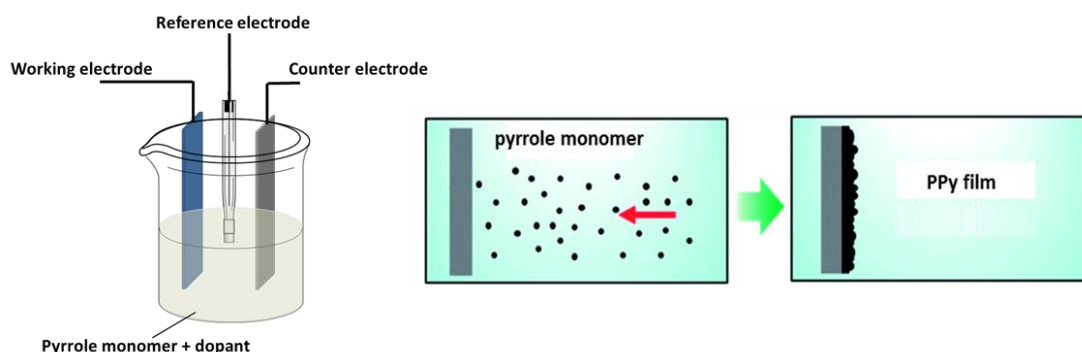


Figure 2.2 A three-electrode cell setup for electropolymerization.

2.2.5 Lithium-ion coin cell and supercapacitor assembly

Since the materials used in my thesis were conductive, free-standing film/paper, they were used directly as electrodes. The conventional slurry mixing and casting procedures involved in the fabrication of conventional electrodes were no longer needed. The film/paper was cut into pieces for use. The coin cell (LR 2032 type) was assembled in an argon-filled glovebox. Figure 2.3 shows the schematic configuration of a coin cell, where the lithium foil and graphene paper act as two electrodes. They are separated by a porous polypropylene membrane, in an electrolyte solution of 1 M LiPF_6 dissolved in the mixed solvent of ethylene carbonate (EC) and dimethyl carbonate (DMC) (1:1 v/v).

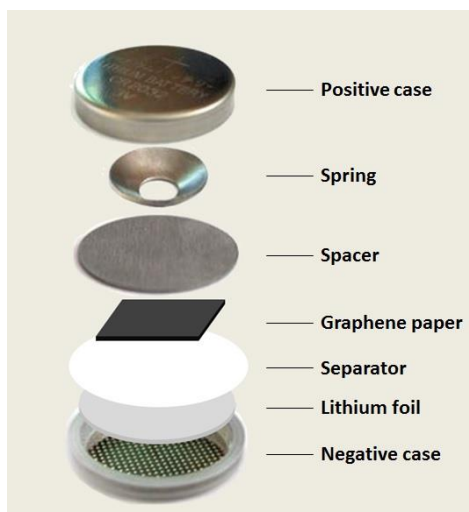


Figure 2.3 Lithium-ion coin cell configuration.

Similar to lithium-ion coin cell fabrication, the graphene based films/papers were cut into pieces and directly used as supercapacitor electrode. A symmetric supercapacitor was assembled into a Swagelok®-type two electrode testing cell. The testing cell consists of a Teflon chamber, two stainless steel plungers and two stainless steel caps. (Figure 2.4) The graphene based film/paper pieces were contacted with the plunger, and separated by the separator. The electrolyte of 1M H_2SO_4 or 1M Li_2SO_4 was filled in the Teflon chamber.

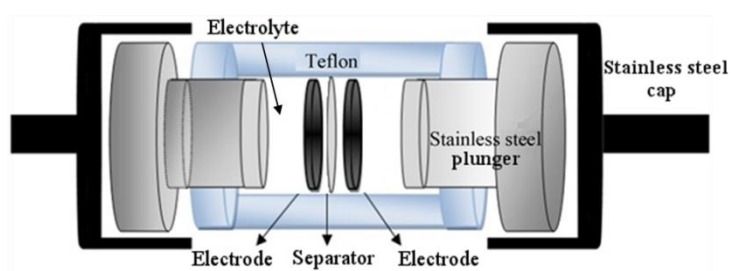


Figure 2.4 Configuration of Swagelok®-type testing cell for supercapacitor.

2.3 Physicochemical Properties Characterization Techniques

2.3.1 Scanning electron microscope

The scanning electron microscope (SEM) is a type of electron microscope used to observe the morphology of samples (Figure 2.5). The samples are scanned by a high-energy focused beam of electrons, and then the signals produced are collected and analyzed from the secondary electrons, back-scattered electrons, characteristic X-rays, transmitted electrons, etc. The electron beam's position coupled with the detected signal forms the images of the specimen that contains information about topography and composition.

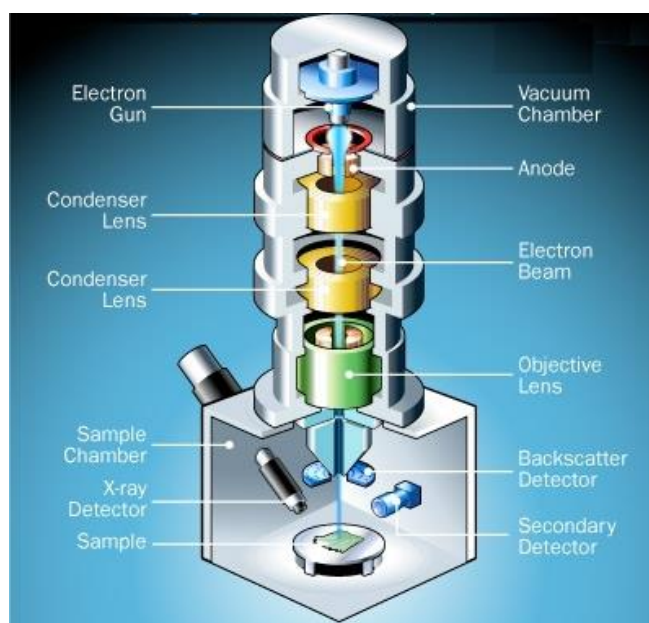


Figure 2.5 Illustration of a scanning electron microscope [8].

Energy-dispersive X-ray spectroscopy (EDX or EDS) is generated by collecting and analyzing the X-ray signals produced by electron beam stimulation. It provides the elemental analysis or chemical characterization of the specimen. In this thesis, SEM images were obtained from a JEOL JSM-7500FA field emission SEM, typically at an

acceleration voltage of 5.0 kV and emission current of 10 μ A. EDX spectroscopy was conducted using a Bruker X-Flash 4010 energy dispersive X-ray (EDX) detector on a JEOL JSM-7500FA, with a 15.0 kV acceleration voltage and a 20 μ A emission current.

2.3.2 Atomic force microscopy

Atomic force microscopy (AFM) is a type of high-resolution scanning probe microscopy, with resolution of several nanometers. The probe in the AFM is a cantilever with a sharp tip. When scanning over the material's surface, forces between the tip and sample lead to a deflection of the cantilever which can be detected using a laser spot which is reflected from the surface of cantilever (Figure 2.6). Using an AFM, it is possible to measure the roughness of a sample surface at a high resolution. In this work, an Asylum MFP-3D AFM is applied for topographical scanning to measure the film thickness.

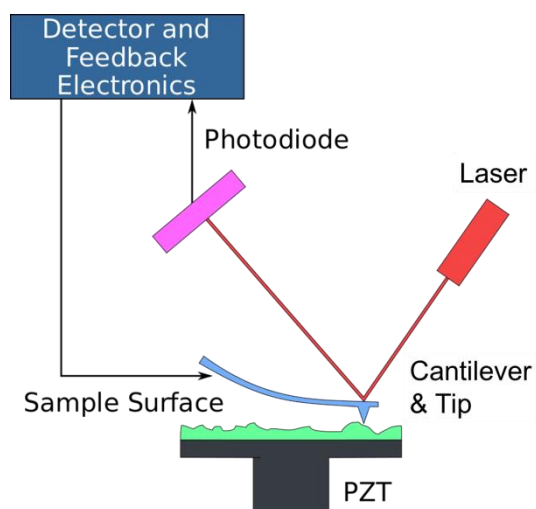


Figure 2.6 Diagram of the basic principle of an AFM [9].

2.3.3 X-ray photoelectron spectroscopy

X-ray photoelectron spectroscopy (XPS) is a surface-sensitive quantitative spectroscopic technique. The spectra are obtained by analyzing the kinetic energy and number of electrons from the sample stimulated by an X-ray beam. The energy of the emitted electrons are characteristic of the material. XPS spectra can reflect the information from the material surface including elemental composition, chemical/electronic state of each element, and empirical formula. In this project, XPS was acquired using a SPECS PHOIBOS 100 Analyser installed in a high-vacuum chamber with pressure $< 10^{-8}$ mbar. X-ray excitation was provided by Al K α radiation with photon energy of 1486.6 eV at a voltage of 12 V and a power of 120 W. XPS data analysis and peak fitting were carried out by applying CasaXPS 2.3.16 software.

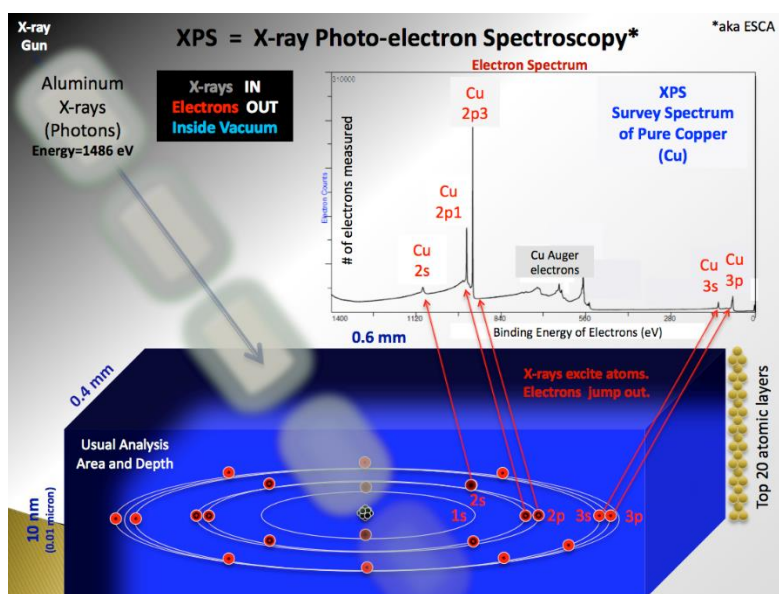


Figure 2.7 Schematic of XPS physics [10].

2.3.4 X-ray diffraction

In X-ray diffraction (XRD), the X-ray beam directed is incident on the materials surface and interacts with the atoms in the crystal. A portion of the X-ray beam will

then be scattered/diffracted due to the interaction within the crystal structure, at a well-defined angle (2θ) with the incident beam. The diffraction pattern for an element or compound is unique, which is related to the crystal structure. The average spacing d between layers or rows of atoms can also be determined by the incident X-ray wavelength λ and angle θ , following Bragg's Law:

$$n\lambda = 2d\sin\theta \quad (2.1)$$

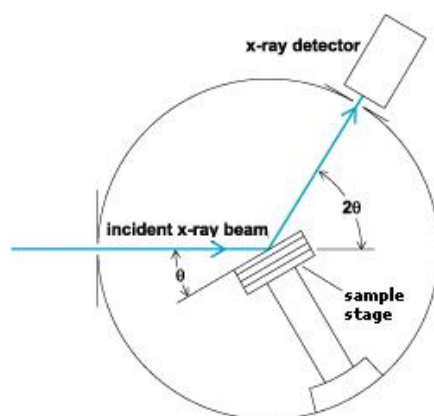


Figure 2.8 Representation of the X-ray diffraction principle.

XRD was applied by use of a GBC MMA XRD at a scanning rate of 2° min^{-1} in a 2θ range of 5-80, using Cu $K\alpha$ X-ray ($\lambda = 1.54 \text{ \AA}$).

2.3.5 Raman spectroscopy

Raman spectroscopy is a spectroscopic technique used to investigate vibrational, rotational modes in materials. It relies on Raman scattering from a laser in visible, near infrared or near ultraviolet range. The laser light interacts with molecular vibrations, phonons or other excitations, resulting in the energy of the laser photons being shifted down or up. Raman spectroscopy yields similar but complementary information as infrared (IR) spectroscopy. The absorbance spectra containing different types of

vibrations are characteristic of each molecule. In this study, Raman spectroscopy was measured by a Jobin-Yvon Horbia 800 using 632.81 nm laser.

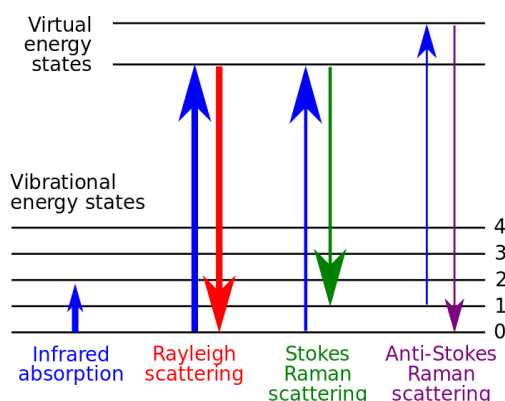


Figure 2.9 Energy-level diagram showing the states involved in Raman signals [11].

2.3.6 Thermogravimetric analysis (TGA)

Thermogravimetric analysis (TGA) is performed on samples to determine changes in weight in relation to temperature change. It can provide information about chemisorption, dehydration, decomposition, etc. Measurements related to this thesis were conducted using a Q500 TGA analyzer, at a ramp rate of $5\text{ }^{\circ}\text{C min}^{-1}$ under nitrogen atmosphere between room temperature to $600\text{ }^{\circ}\text{C}$. The samples were dried in vacuum at $70\text{ }^{\circ}\text{C}$ overnight prior to the measurements.

2.3.7 Zeta potential measurement

Zeta potential measurement is used to determine the surface charge of the particles suspended in a liquid. The zeta potential is the potential difference between the dispersion medium and the stationary layer of fluid attached to the dispersed particles. Small particles do not form agglomerates when there are large mutually repulsive electrostatic charges, so the zeta potential is highly related to the stability of colloidal

suspensions. The threshold region of either coagulation or dispersion exists from about ± 14 mV to ± 30 mV. Values more electronegative or electropositive than 30 mV generally represent sufficient mutual repulsion to result in stable dispersions. In our thesis, zeta potential measurements were carried out by use of a Zetasizer (Malvern Instruments Ltd., UK).

2.3.8 Ultraviolet-visible spectroscopy

Ultraviolet-visible spectroscopy (UV-vis) is routinely used for the quantitative determination of transition metal ions, highly conjugated organic compounds, and biological macromolecules. Molecules containing π -electrons or non-bonding electrons (n-electrons) can absorb the energy in the form of ultraviolet or visible light to excite these electrons to higher anti-bonding molecular orbitals. UV-vis measures such transitions from ground state to excited states. Following the Lambert-Beer law, the UV-vis spectra can be used to determine the concentration of solutions. By definition of the Lambert-Beer law, the absorbance of material sample A is related to the concentration of the solution c (mol L^{-1}) of sample and the length of the light path l (cm).

$$A = \log \frac{I_0}{I} = \epsilon cl \quad (2.2)$$

The constant ϵ ($\text{L mol}^{-1} \text{cm}^{-1}$) is called the molar absorptivity or molar extinction coefficient. Our UV-vis spectra were recorded with a UV spectrophotometer (UV-1800, Shimadzu).

2.3.9 Conductivity measurement

The conductivity of graphene films/papers were measured by a Jandel Model RM3 four probe system. A four probe system uses separate pairs of current-carrying and voltage-sensing electrodes to eliminate the lead and contact resistance from the measurement. It provides more accurate measurements than the two-terminal sensing. As shown in Figure 2.10, current is applied via connections 1 and 4, whilst the sheet resistance is determined from the measured voltage between connections 2 and 3. The conductivity of films σ (S cm^{-1} or S m^{-1}) can be calculated from the sheet resistance R (Ω) using Equation 2.3:

$$\sigma = \frac{1}{Rl} \quad (2.3)$$

where l (cm or m) is the thickness of the film.

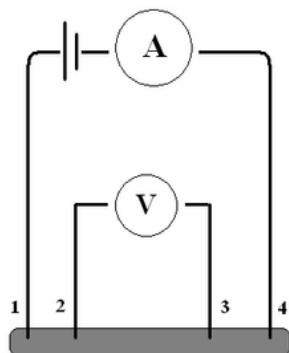


Figure 2.10 Schematic of a four-point resistance measurement [12].

2.4 Electrochemical Properties Characterization Techniques

2.4.1 Cyclic voltammetry

Cyclic voltammetry (CV) is a potentiodynamic electrochemical measurement, which can investigate the kinetics of electron transfer in an electrochemical reaction at the interface of working electrode. It measures the resulting current developed in an

electrochemical cell by cycling the potential of a working electrode. The applied potential ramps linearly versus time. The potential change as a function of time is called scan rate.

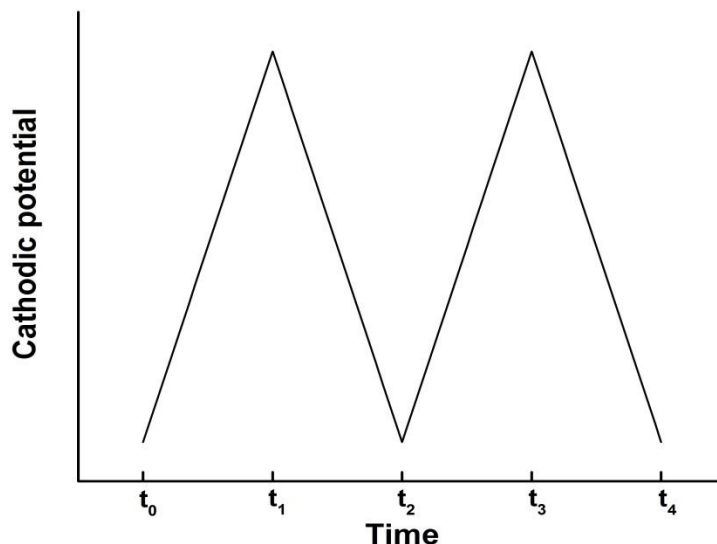


Figure 2.11 A classical triangular waveform used in cyclic voltammetry.

When the potential reaches the point where a reaction occurs, the current will increase and form a peak. In a redox reaction, pairs of peaks appear when the potential is scanned in different directions. The oxidation and reduction potentials can be estimated from the peak position, and the peak area allows quantification of the charge passed during oxidation and reduction. Moreover, the potential difference between the peaks of oxidation and reduction provides an assessment of the reversibility of an electrochemical reaction.

In this study, CV was mainly used to study the electrochemical redox processes or capacitive properties of the electrode materials or devices. The measurement for lithium-ion coin cells was performed using a SI1287 Electrochemical Interface (Solartron analytical, USA). For supercapacitor evaluation, the CV tests were conducted by use of a CHI 650D (CH Instruments, Inc).

2.4.2 Galvanostatic charge/discharge

The galvanostatic charge/discharge test is a kind of chronopotentiometry method, which measures the resulting potential as a function of time with constant current applied to the working electrode. In a galvanostatic charge/discharge test, the constant anodic/cathodic current applied causes the electroactive species to be oxidized/reduced. It can be used to characterize the capacity/capacitance and cycle performance of the materials. In this thesis, the charge/discharge for supercapacitors were measured by using a BTS3000 battery test system (Neware Electronic Co.). The capacity and cycle performance of lithium-ion battery electrodes were tested by use of a Land battery test system (Wuhan Jingnuo, China).

2.4.3 Electrochemical impedance spectroscopy

Electrochemical impedance spectroscopy (EIS) measures the impedance of a system with a small AC potential applied over a range of frequencies. It can reveal the electrochemical processes in an electrode material such as electron transfer and mass transport. Data obtained by EIS can be expressed graphically in a Bode plot or a Nyquist plot. The Nyquist plot is obtained by plotting the real part of impedance on the X-axis and the imaginary part on the Y-axis of a chart. Another data presentation method, Bode Plot, is plotted with the logarithmic value of frequency on the X-axis and the absolute values of the impedance and/or phase shift on the Y-axis. In this study, EIS was performed using a Gamry EIS 3000 system, and the frequency range spanned from 100 kHz to 0.01 Hz with an AC amplitude of 10 mV at open circuit potential. The EIS results were analyzed by using Zview software.

2.5 References

- [1] W.S. Hummers, R.E. Offeman, Preparation of Graphitic Oxide, *Journal of the American Chemical Society*, 80 (1958) 1339-1339.
- [2] M.D. Stoller, S.J. Park, Y.W. Zhu, J.H. An, R.S. Ruoff, Graphene-Based Ultracapacitors, *Nano Letters*, 8 (2008) 3498-3502.
- [3] D. Li, M.B. Muller, S. Gilje, R.B. Kaner, G.G. Wallace, Processable Aqueous Dispersions of Graphene Nanosheets, *Nat Nano*, 3 (2008) 101-105.
- [4] H. Chen, M.B. Mueller, K.J. Gilmore, G.G. Wallace, D. Li, Mechanically Strong, Electrically Conductive, and Biocompatible Graphene Paper, *Advanced Materials*, 20 (2008) 3557-3561.
- [5] D.A. Dikin, S. Stankovich, E.J. Zimney, R.D. Piner, G.H.B. Dommett, G. Evmenenko, S.T. Nguyen, R.S. Ruoff, Preparation and Characterization of Graphene Oxide Paper, *Nature*, 448 (2007) 457-460.
- [6] X. Yang, L. Qiu, C. Cheng, Y. Wu, Z.-F. Ma, D. Li, Ordered Gelation of Chemically Converted Graphene for Next-Generation Electroconductive Hydrogel Films, *Angewandte Chemie International Edition*, 50 (2011) 7325-7328.
- [7] X. Yang, J. Zhu, L. Qiu, D. Li, Bioinspired Effective Prevention of Restacking in Multilayered Graphene Films: Towards the Next Generation of High-Performance Supercapacitors, *Advanced Materials*, 23 (2011) 2833-2838.
- [8] "How Scanning Electron Microscopes Work." from <http://science.howstuffworks.com/scanning-electron-microscope2.htm>.
- [9] "Nanotechnology Tomorrow." from <http://nanotekimorgen.weebly.com/nanomikroskopi.html>.
- [10] "Wikipedia--X-ray Photoelectron Spectroscopy." from http://en.wikipedia.org/wiki/X-ray_photoelectron_spectroscopy.
- [11] "Wikipedia--Raman Spectroscopy." from http://en.wikipedia.org/wiki/Raman_spectroscopy.
- [12] "Wikipedia--Four-terminal Sensing." from http://en.wikipedia.org/wiki/Four-terminal_sensing.

3 Graphene Cryogel Paper with Enhanced Mechanical Strength for High Performance Lithium-ion Battery.

This chapter is adapted from the research article entitled “*Graphene cryogel papers with enhanced mechanical strength for high performance lithium battery anodes*” by Shu, K.; Wang, C.; Wang, M.; Zhao, C.; Wallace, G. G. in *Journal of Materials Chemistry A* **2014**, *2* (5), 1325-1331. (link: <http://pubs.rsc.org/en/content/articlelanding/2014/ta/c3ta13660d>). Reproduced by permission of The Royal Society of Chemistry.

3.1 Introduction

Graphene possesses the advantages of high specific surface area and excellent electronic transport properties. It has been extensively investigated as battery or supercapacitor material, offering excellent electrochemical properties, high energy and power densities [1-4]. The flexible graphene or graphene oxide (GO) paper can also be easily fabricated by flow-directed graphene nanosheets assembly [5, 6]. Superior electrochemical properties are expected as that from the graphene powder [1-3, 7, 8]. However, its performance was far from satisfactory. It delivered a low reversible discharge capacity of 84 mAh g⁻¹ at a current density of 50 mA g⁻¹, but the reversible capacity increased to 301 mAh g⁻¹ after removing some oxygen containing functional groups in our previous report [9]. It can be explained that the aggregation or restacking of the graphene nanosheets due to the strong π - π stacking, which limits the available surface area, retards its electrochemical properties.

To obtain a porous/non-compact graphene paper with high charge capacity, several strategies such as leavening, template-directed assembly and cavitation-chemical oxidation are applied [10-12]. The “wet” graphene paper, with solvents as the spacer preventing the graphene nanosheets restacking [13], delivered a specific capacitance of 156.5 F g^{-1} at an ultrafast charge-discharge rate of 1080 A g^{-1} . Graphene paper with open pores can also be formed, with cavities due to gas release during the chemical reduction of GO paper. Such paper delivered a greatly improved specific capacitance of 110 F g^{-1} at 0.5 A g^{-1} in comparison with that of 17 F g^{-1} for highly packed graphene paper [10]. By using polymer microspheres as the template, a macroporous graphene paper with controlled pore size was fabricated by flow-directed self-assembly method. The macroporous graphene paper exhibits a capacitance of 49.2 F g^{-1} at 3.0 A g^{-1} [12].

More recently, a folded structure graphene paper was made from a freeze-dried GO cryogel and subsequent thermal reduction. It presented significantly improved performance in lithium batteries compared to the graphene paper by filtration, which can maintain a reversible capacity of 568 mAh g^{-1} at 100 mA g^{-1} after 100 cycles [14]. However, this paper was brittle and fragile due to its loose-packed layered structure. The thermal reduction of such GO cryogel paper further deteriorates its mechanical properties.

In this work, chemically reduced graphene (CRG) was introduced into the GO dispersion as the precursor solution for making the graphene cryogel. CRG possesses much less functional groups than GO. The introduction of CRG can decrease the entrapped water content associated with H-bonding in the formed graphene cryogel, which are expected to result in cryogel with better mechanical properties. The rationale is that the mechanical properties of graphene paper were essentially controlled by H-

bond networks which strength can be enhanced with decreased water content within the interlayer cavities [15]. Our results clearly demonstrate that the mechanical properties of the graphene paper are remarkably enhanced with the increasing ratio of CRG. In addition, those CRG/GO hybrid papers all display excellent performance as anode in lithium ion battery, especially at high current densities.

3.2 Experimental Specific to This Chapter

3.2.1 Synthesis of graphene oxide (GO) and CRG dispersion

The synthesis of GO and CRG dispersion was described in Chapter 2 (Experimental). The dispersion was diluted to the required concentration for testing and paper fabrication.

3.2.2 Fabrication of Graphene Cryogel Paper and Coin Cell Assembly

Table 3.1 Recipe for precursor solution with different CRG/GO ratio

	Ratio CRG/GO	Recipe for precursor solution
GO	---	10 mL 2.4 mg mL ⁻¹ GO
GO-CRG-5	1:5	3.3 mL 6 mg mL ⁻¹ GO+ 10 mL 0.4 mg mL ⁻¹ CRG
GO-CRG-2	1:2	2.7 mL 6 mg mL ⁻¹ GO+ 20 mL 0.4 mg mL ⁻¹ CRG
GO-CRG-0.5	2:1	1.3 mL 6 mg mL ⁻¹ GO+ 16 mL 1 mg mL ⁻¹ CRG

The as-prepared CRG solution was diluted to give a concentration of 1 mg mL⁻¹ and 0.4 mg mL⁻¹. The CRG/GO precursor hybrid solution was obtained by directly stirring the GO and CRG solution. The CRG/GO mass ratios used in this work were 1:5, 1:2 and 2:1. The detailed information is listed in Table 3.1. The resultant hybrid solution was transferred into a 50 ml beaker and subjected to a freezing-drying process to form a cryogel, which included an 8 h freezing at -30°C and a 36 h freeze-drying. The hybrid (CRG/GO) papers were obtained by pressing the cryogels at 20 MPa, and named as GO-CRG-0.5, GO-CRG-2 and GO-CRG-5 according to the mass ratio of GO to CRG. The reduced graphene (rGO) papers were obtained using thermal reduction of the GO or hybrid papers at 220°C in air for 2h. Correspondingly, they are named as rGO-CRG-0.5, rGO-CRG-2 and rGO-CRG-5, respectively. A pure rGO paper was also prepared using the same method for comparison. In addition, graphene paper was also prepared by filtration of 0.4 mg mL⁻¹ CRG solution (60 mL). The graphene papers were assembled into LR 2032 type coin cells coupled with lithium metal anode for electrochemical properties testing including CV, charge/discharge and EIS. The electrolyte used was 1 M LiPF₆ in 1:1 (v/v) ethylene carbonate/dimethyl carbonate.

3.2.3 Characterization techniques

Conductivity measurements were carried out on a Jandel RM3 Conductivity Meter using a four-point probe method. The morphology was investigated using a field-emission scanning electron microscope (FESEM, JEOL JSM7500FA). XRD measurements were performed on an Australian GBC Scientific X-ray diffractometer (Cu K_{α} radiation, $\lambda=1.5418 \text{ \AA}$) at a scan rate of $2^{\circ} \text{ min}^{-1}$. The thermal properties were characterized by TGA (Q500, TA instruments). The measurements were tested under nitrogen at a ramp rate of $5^{\circ}\text{C min}^{-1}$. Zeta potential measurements were carried out by Zetasizer (Malvern Instruments Ltd., UK). Uniaxial in-plane tensile tests were studied using a Shimadzu EZ mechanical tester. The samples with a dimension of approximately $3 \times 15 \text{ mm}^2$ were used for mechanical testing at a cross head speed of 1 mm min^{-1} . Galvanostatic charge/discharge tests were performed using a LAND CT2001A battery test system (Wuhan Jinnuo Electronics Co. Ltd.) over a potential range of 0.005–3.0 V (vs. Li/Li⁺). Cyclic voltammetry of the cells was tested using a Solartron SI 1287 and scanned between 0.0 to 3.0 V (vs. Li/Li⁺) at a rate of 0.1 mV s^{-1} . Electrochemical impedance spectroscopy (EIS) measurements were performed using a Gamry EIS 3000 system, and the frequency range spanned from 100 kHz to 0.01 Hz with an amplitude of 10 mV at open circuit potential.

3.3 Results and Discussion

3.3.1 Characterization of chemically reduced graphene dispersion

The UV-vis spectra are used to evidence the reduction of GO. After reduction, the absorbance peak shifted from 270 nm (GO) to 230 nm (CRG) (Figure 3.1a). This

blueshift is caused by the recovery of conjugation structure upon hydrazine reduction [16]. It is believed that the formation of stable graphene colloid dispersion is attributed to the electrostatic repulsion, which relies on the surface charge of particles. So the surface charge of GO and the obtained CRG was examined through zeta potential measurements. As it is well known from colloidal science, zeta potential values over 30 mV are generally considered to ensure the stability of a colloidal dispersion [17]. Our GO colloidal dispersion was highly negatively charged, with a zeta potential of -42.7 mV. Equivalent zeta potential of -42.2 mV was acquired from the CRG dispersion, showing it was also a stable colloid dispersion with highly negative charge after reduction. Such stable CRG dispersions were able to remain thus over weeks. AFM images of CRG are shown in Figure 3.1b. The sample was prepared by drop-casting the diluted CRG dispersion onto a silicon wafer. From the AFM images, single graphene sheets which were several hundred nanometres in size and around 2~3 nm in thickness could be easily found, indicating successful exfoliation.

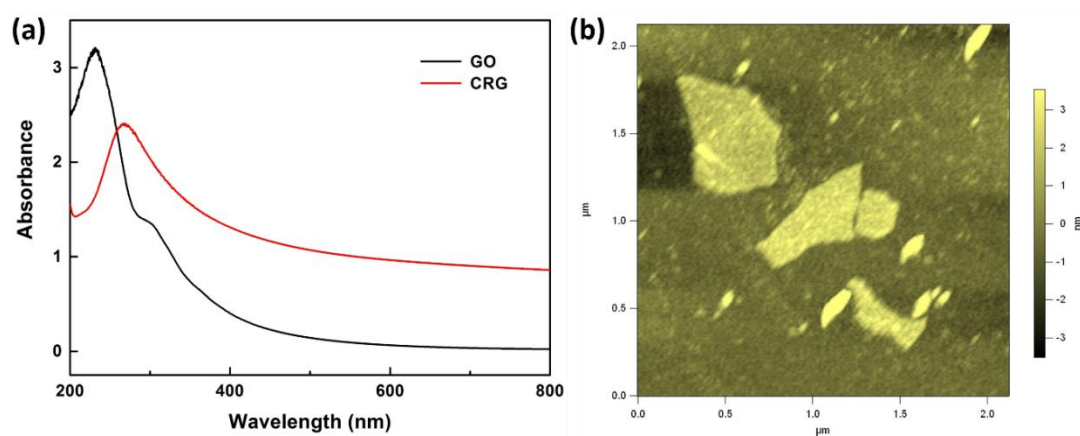


Figure 3.1 (a) UV-vis spectra of GO and CRG dispersion; (b) AFM images of CRG.

3.3.2 Characterization of graphene cryogel paper

The as-prepared cryogel shows an interconnected three-dimensional porous network (Figure 3.2) with the pore wall composed of graphene sheets. The pores are formed due to the sublimation of ice crystal during the freeze drying process, and its size is in the range of tens of micrometres to sub-millimetres [9]. The graphene cryogel paper can be easily obtained by pressing the cryogel at 20 MPa, followed by thermal annealing at 220°C for 2h in air. Figure 3.2e, f are the photographs of the cryogel and pressed paper respectively. Such cryogel paper afforded good flexibility as demonstrated in Figure 3.2f. The thickness of all the graphene papers was around 20 μm with a conductivity of approximately 2-5 S cm^{-1} .

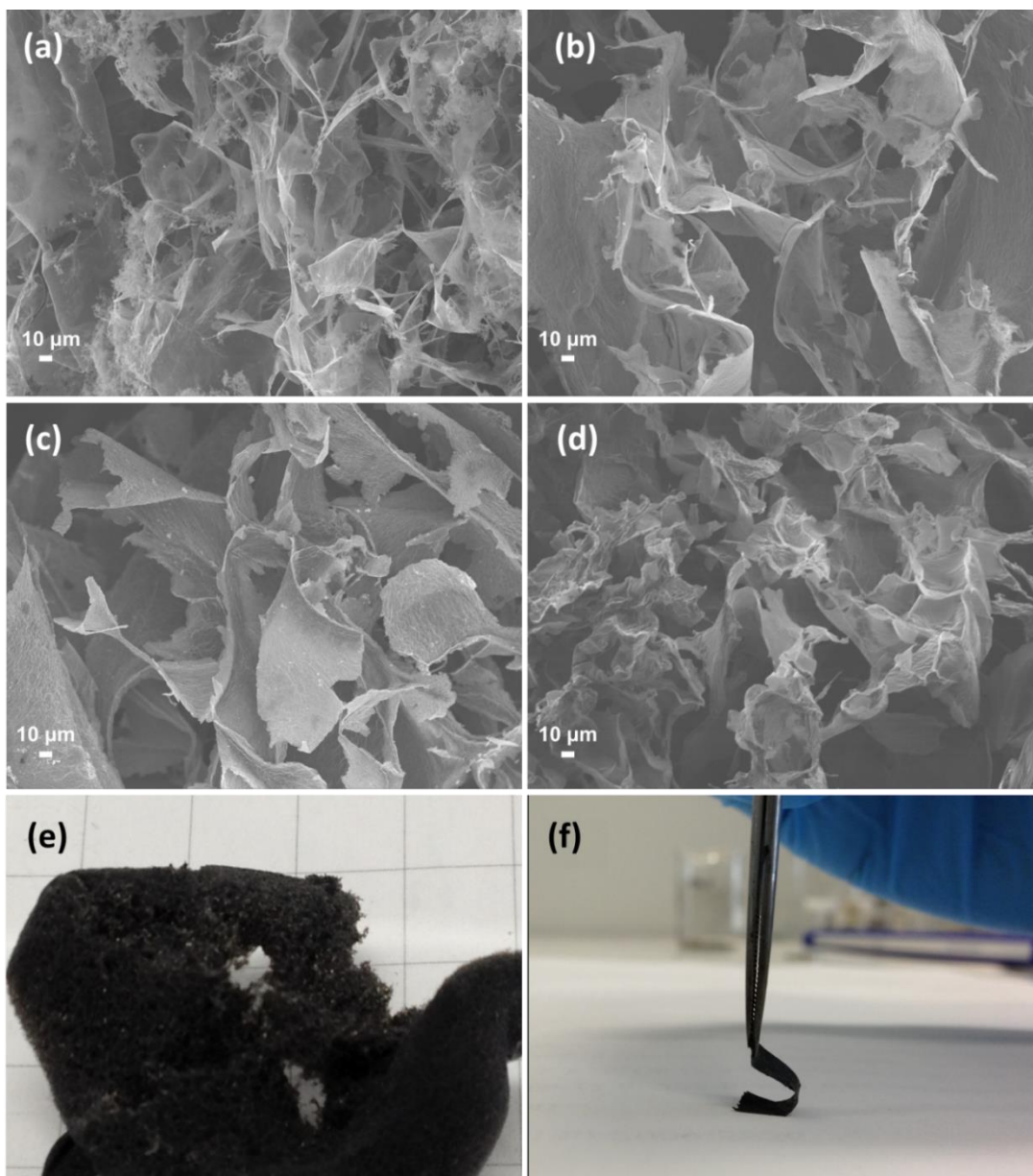


Figure 3.2 SEM images of (a) rGO-CRG-0.5, (b) rGO-CRG-2, (c) rGO-CRG-5 and (d) rGO cryogels. Photograph of (e) rGO-CRG-0.5 cryogel and (f) rGO-CRG-0.5 paper.

Figure 3.3 shows the surface and cross-section morphology of the graphene cryogel paper. The graphene paper exhibits a rough surface containing graphene folds with uniform size (Figure 3.3a), quite different from the smooth surface of that graphene paper fabricated by flow-directed filtration (Figure 3.3c). A loosely-packed layered structure can be observed through the cross-sectional view of the graphene

paper (Figure 3.3b), in comparison with the compacted graphene layers structures for graphene paper formed by filtration (Figure 3.3d).

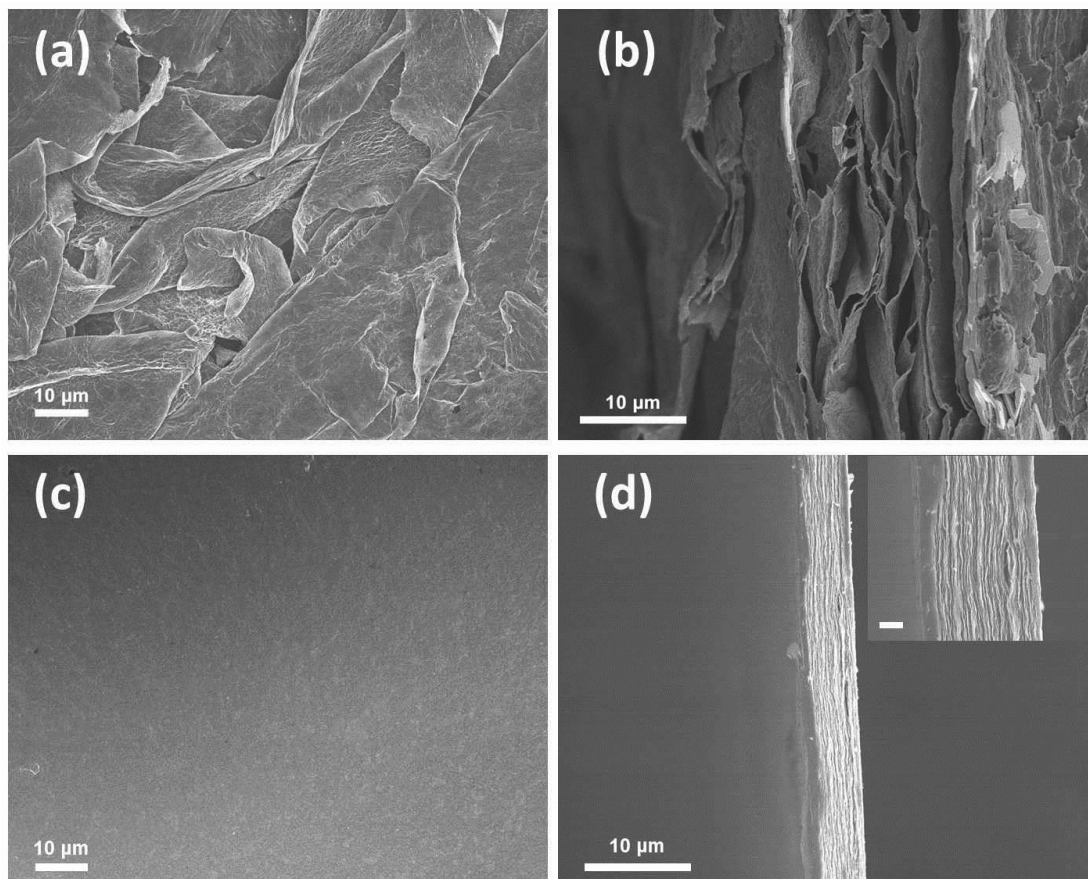


Figure 3.3 SEM images of the surface morphology and cross section of rGO-CRG-0.5 paper (a, b) and CRG paper by filtration (c, d). (f inset: cross section of CRG by filtration at higher magnification, scale bar, 1 μm)

X-ray diffraction (XRD) patterns of the hybrid paper and GO paper before and after reduction are shown in Figure 3.4a. GO paper displayed a strong and sharp peak at 9.8° (2θ), same as that reported for GO solids and GO paper [18, 19]. This strong diffraction is derived from the interspacing between the stacking layers of GO sheets, which corresponds to a d-spacing of ~ 0.91 nm. After thermal reduction, a broad peak at

24° (2θ) is presented for rGO paper, which corresponds to an average interlayer spacing of 0.37 nm [20]. Compared to GO paper, the hybrid papers displayed two peaks, close to 10° and 24°. The former belongs to (0 0 2) diffraction of GO, and the latter can be ascribed to (0 0 2) diffraction of rGO. The (0 0 2) peak intensity decreased correspondingly with the decreased GO content in this hybrid. For GO-CRG-5 paper, there is no pronounced rGO peak due to its low content.

The TGA curves of the graphene paper with different CRG/GO ratio are shown in Figure 3.4b. The weight loss below 100 °C can be attributed to the evaporation of absorbed water. The hydrophilic GO paper demonstrated a substantial loss of approximately 10% in this temperature range. The major weight loss of GO paper occurred near 150°C, which may be caused by pyrolysis of oxygen-containing groups [19]. The temperature range between 100-200°C is mainly where the decomposition of oxygen-containing groups on GO in these hybrid papers occurred. The weight losses were 25%, 17%, 13% and 7% for GO, GO-CRG-5, GO-CRG-2, GO-CRG-0.5 respectively. The decreasing weight loss in that temperature range indicates the ratio change of GO in the hybrid papers. For all of the papers, the weight loss in the temperature range between 200 °C and 500 °C was about 10%, which was probably due to the decomposition of some residual oxygen-containing groups [6]. The total weight losses between 100°C to 600°C for rGO, GO-CRG-0.5, GO-CRG-2, GO-CRG-5 and rGO were 9%, 14%, 30%, 35% and 53% respectively.

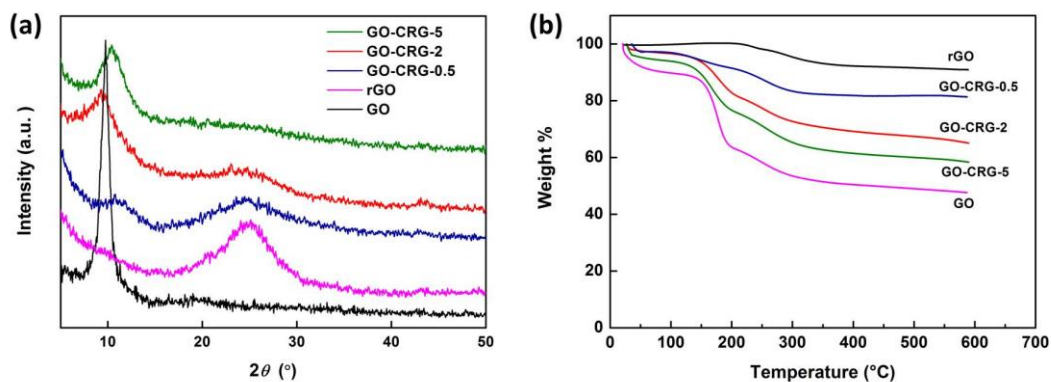


Figure 3.4 (a) XRD patterns of GO and hybrid papers; (b) TGA curves of graphene papers with different CRG/GO ratio.

The mechanical properties were tested in uniaxial tension of the graphene strips. The stress-strain responses of graphene papers with different CRG/GO ratios are shown in Figure 3.5. These curves show a straightening behaviour at the beginning followed by roughly linear behaviour and then plastic deformation behaviour, similar to that for graphene paper fabricated by a filtration method [5]. The ultimate tensile strain for the hybrid graphene papers was 1.5 %, twice as much as the value of rGO paper (0.75 %). The Young's modulus can be calculated from the initial slope of the stress strain curve, and it was 58, 92, 179 and 510 MPa for rGO, rGO-CRG-5, rGO-CRG-2 and rGO-CRG-0.5, respectively. It can be clearly seen that the mechanical properties of the graphene papers were improved with the increasing ratio of CRG. It is believed that lower water content in graphene papers lead to better H-bond networks making the graphene paper stiffer [15]. The increase of mechanical strength resulted from the lower water content of the hydrophobic CRG sheets compared to hydrophilic GO sheets. In addition, the hybrid paper with higher GO content may also have suffered from the structural destruction caused by pyrolysis of oxygen-containing groups during the

thermal reduction, resulting in poorer mechanical properties. It should also be pointed out that these graphene papers presented much lower modulus compared to the flow-directed assembled graphene paper [5], which can be ascribed to their loosely packed structure.

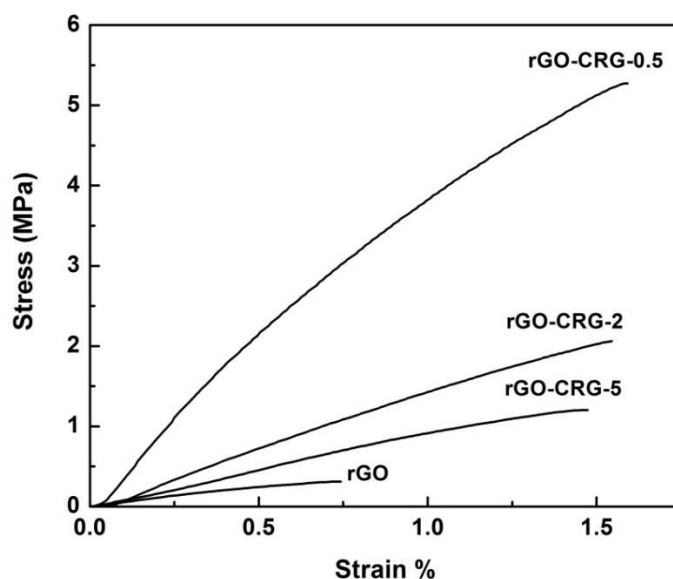


Figure 3.5 Stress-strain curves of graphene papers with different CRG/GO ratio.

3.3.3 Electrochemical performances as a LIB anode

The electrochemical properties of these graphene papers as binder-free electrode for lithium batteries were evaluated by galvanostatic charge/discharge in the potential range from 0.005 to 3.0 V. The first and second cycle charge/discharge profiles of these graphene paper electrodes with different CRG/GO ratios at a current density of 50 mA g^{-1} are shown in Figure 3.6. The irreversible capacity around 0.75 V can be associated with the formation of solid electrolyte interface (SEI) layer in the first cycle. The reversible capacity below 0.5 V should be due to lithium binding on the basal plane of the graphene sheets. The capacity between 0.5-1.5 V may be ascribed to the faradic

capacitance on the surface or on the edge sites of graphene sheets [4]. All of the graphene cryogel papers exhibited much similar performance, with discharge capacities varying from 900 to 1100 mAh g⁻¹. They all presented an irreversible capacity between the first and second discharge cycle. Take rGO-CRG-0.5 paper as an example, it delivered a first discharge capacity of 903 mAh g⁻¹, then the discharge capacity dropped to 642 mAh g⁻¹ at the second cycle (Figure 3.6d). The hybrid graphene cryogel paper exhibited a much higher reversible capacity compared to that graphene paper obtained by filtration, which showed a capacity of 229 mAh g⁻¹ only in the second discharge at the same current density (Figure 3.6e). The Coulombic efficiency of these graphene cryogel papers was about 60-70% during the initial discharge/charge cycle. This high Coulombic efficiency and high reversible capacity could be attributed to the increased active sites provided by the porous and loose-packed structure in graphene cryogel papers [14]. In the compact graphene paper, the compact stacked graphite-like structure could possibly reduce the number of active sites and also hinder the electrolyte penetration, result in low coulombic efficiency (<30%) during the first discharge/charge cycle [9, 18, 21]. The rGO-CRG-0.5 paper showed equivalent performance to that of rGO cryogel paper (Figure 3.6c), which had a second discharge capacity of 600 mAh g⁻¹, indicating that the electrochemical performance of the cryogel paper was not affected by introduction of CRG.

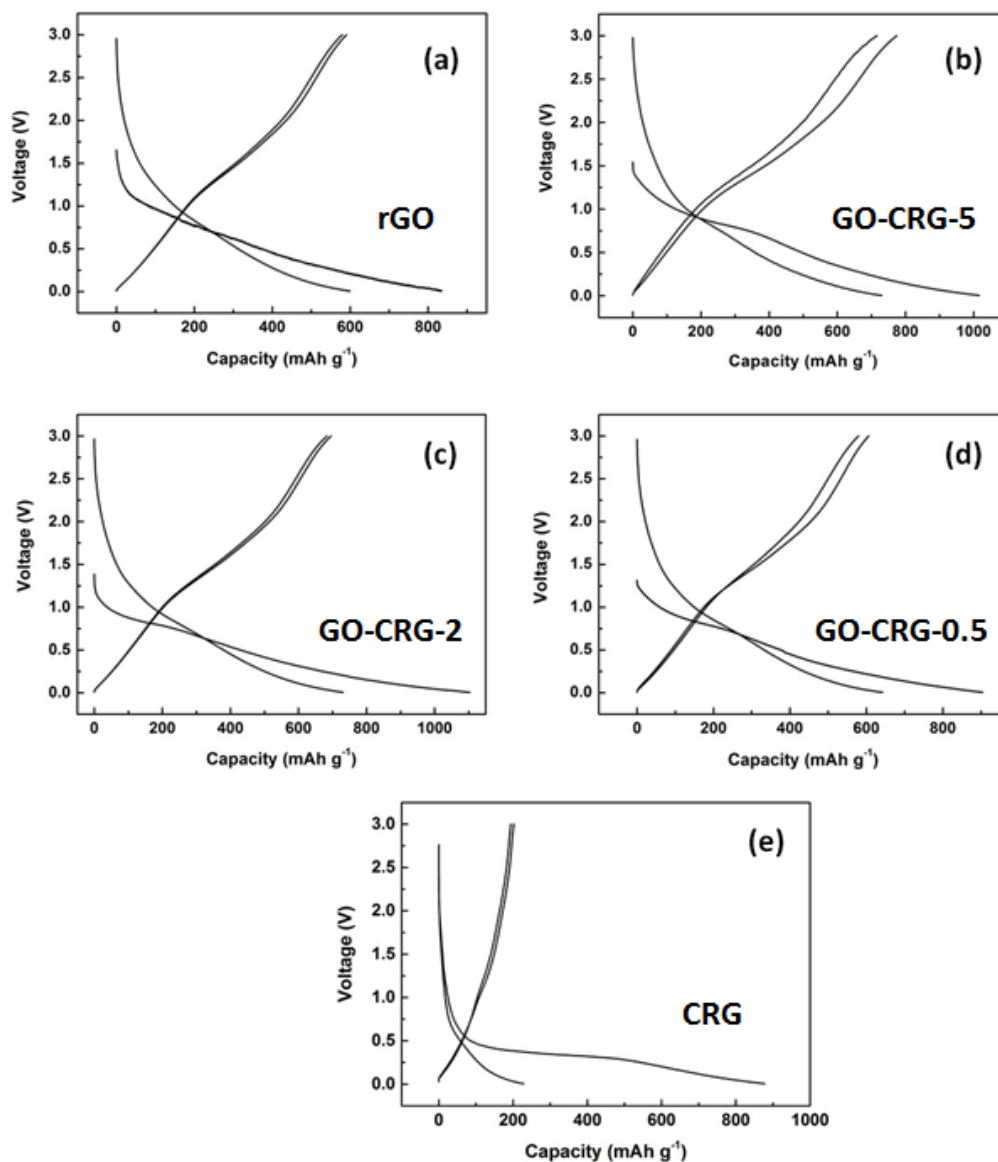


Figure 3.6 The first and second discharge/charge curves of graphene papers: (a) rGO, (b) GO-CRG-5 (c), GO-CRG-2, (d) GO-CRG-0.5 and (e) CRG.

The cyclic voltammograms (CV) of the graphene cryogel paper and CRG paper are shown in Figure 3.7. They all exhibit much similar current response over the electrochemical window of 0.0 V to 3.0 V (versus Li/Li⁺). A large cathodic peak corresponding to lithium intercalation appeared around 0.0 V, and became weaker after the first cycle due to the lithium intercalation reaction being partially reversible. The

cathodic peak around 0.75 V indicates the formation of SEI. The cathodic peak at about 1.5 V can be attributed to lithium interactions with the residual functional groups on the surface or on the edge sites of graphene sheets. The shape of the CV curves matches well with the discharge/charge profiles.

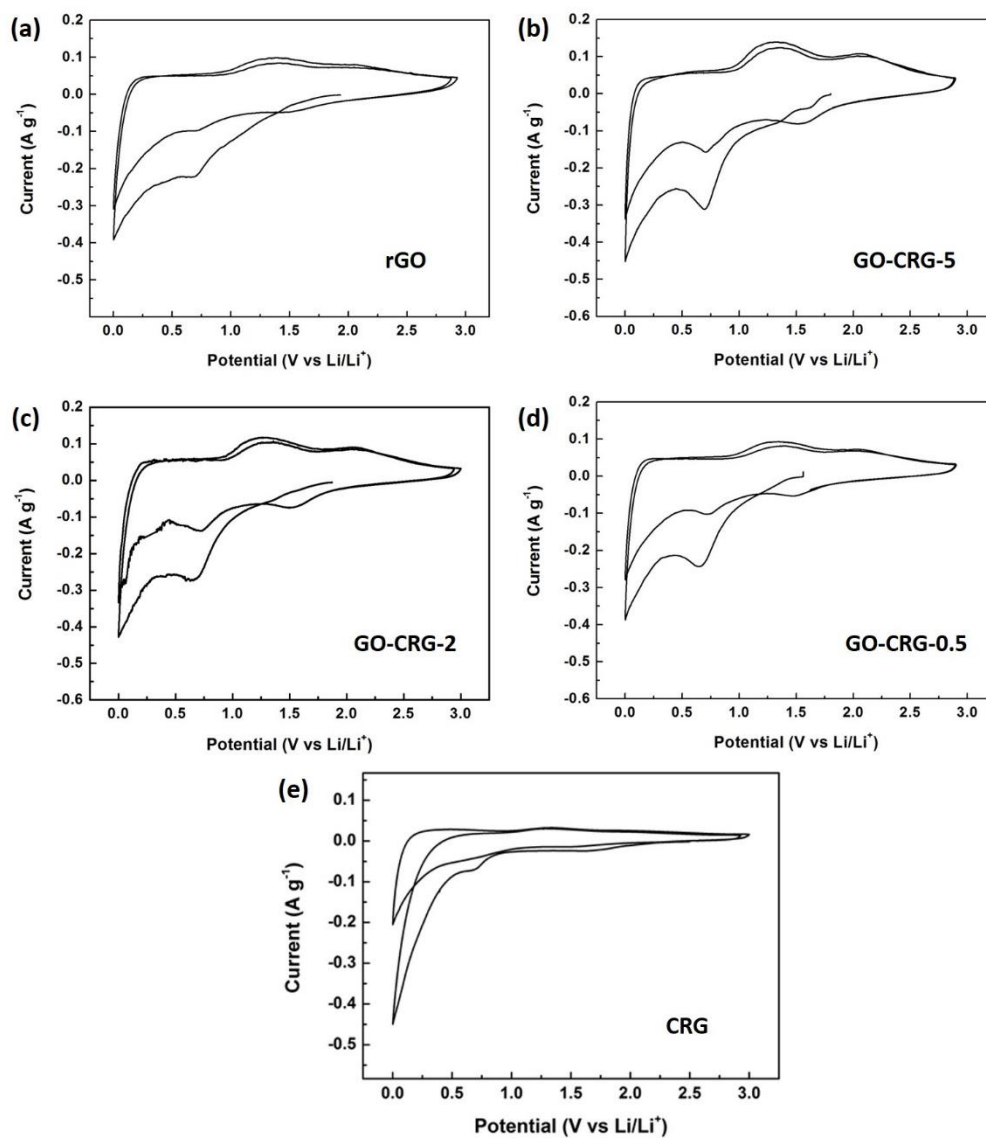


Figure 3.7 Cyclic voltammograms obtained for graphene papers at a scan rate of 0.1 mV s⁻¹: (a) rGO, (b) GO-CRG-5, (c) GO-CRG-2, (d) GO-CRG-0.5 and (e) CRG.

Figure 3.8a, b present the charge/discharge profiles of graphene cryogel papers at higher current densities. The performance of CRG paper (filtration) electrode at higher current densities is not shown here due to its very low discharge capacity even at a low discharge current density of 50 mA g^{-1} . As can be clearly seen, such graphene papers possessed high rate discharge/charge capability. For a rGO-CRG-0.5 paper (Figure 3.9b), at current densities of 200, 500, 1000, 2000 and 3000 mA g^{-1} , the corresponding reversible capacities can reach 622, 557, 485, 405 and 355 mAh g^{-1} , respectively. The performance of rGO-CRG-0.5 is very close to that of rGO paper, which showed a reversible capacity of 596, 537, 471, 403 and 357 mAh g^{-1} , respectively (Figure 3.9a). The high rate discharge/charge properties likely originate from enhanced diffusion of lithium ions into the host sites of graphene sheets due to the folded and porous structure of the graphene paper. They also displayed a good cyclic performance and reversibility (Figure 3.9c, d). After 100 cycles at a high current density of 2000 mA g^{-1} , the rGO-CRG-0.5 paper and rGO paper still maintained a specific capacity of 395 mAh g^{-1} and 394 mAh g^{-1} , 98.7% and 98.9% of the initial capacity respectively.

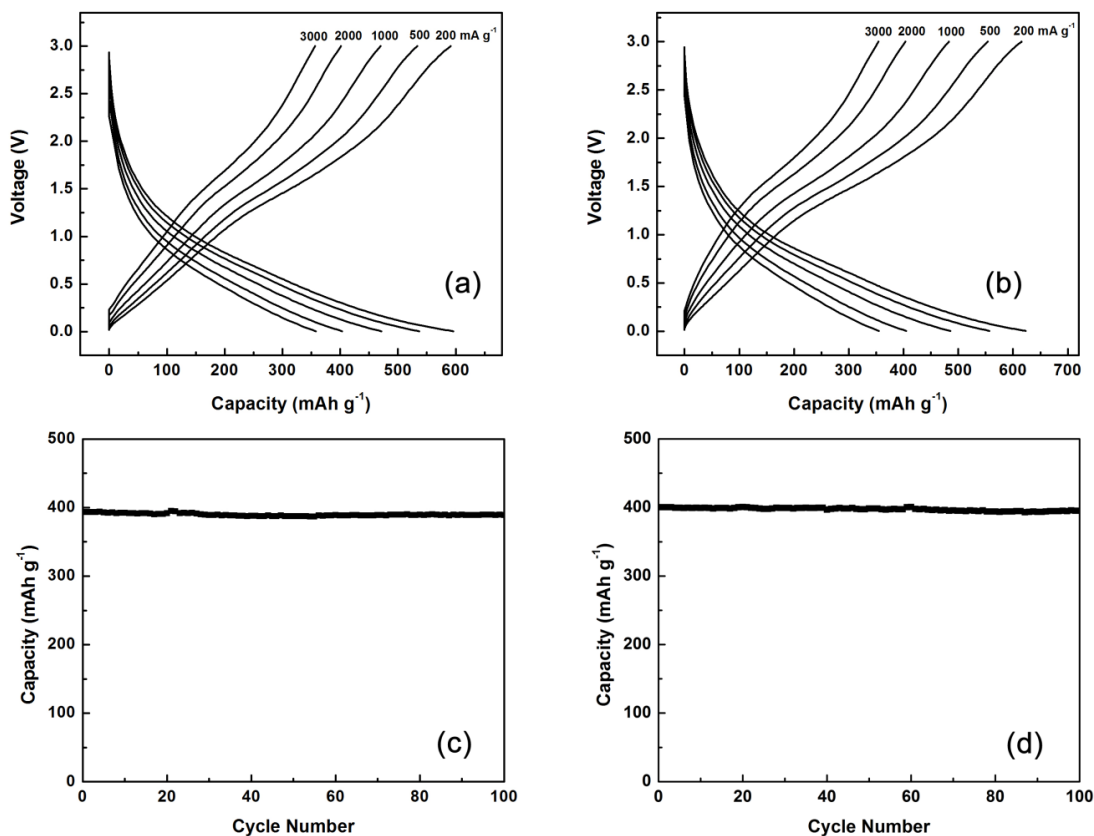


Figure 3.8 Charge/discharge curves of graphene papers at different current densities: (a) rGO, (b) GO-CRG-0.5. Capacity versus cycle number at a current density of 2000 mA g⁻¹: (c) rGO, (d) GO-CRG-0.5.

The electrochemical impedance of filtrated graphene paper and graphene cryogel paper electrodes was measured after 100 cycles, and the Nyquist plot is shown in Figure 3.9. The semicircle in the medium to high frequency region is related to the charge-transfer reaction of lithium intercalation, and the inclined line with an approximate 45° angle to the real axis in the low frequency region corresponds to the lithium-diffusion process within carbon electrodes [22]. It can be clearly seen from the EIS curves that the diameter of the semicircle of the graphene cryogel papers is significantly reduced compared to that for the graphene paper by filtration, indicative of a lower charge-transfer resistance in the graphene cryogel papers. It matches the results

that graphene cryogel papers deliver an excellent performance in LIBs. The reduced charge transfer resistance might be associated with the easy accessibility and transportation of Li ions and electrolyte due to the wrinkles and folds in these graphene cryogel papers.

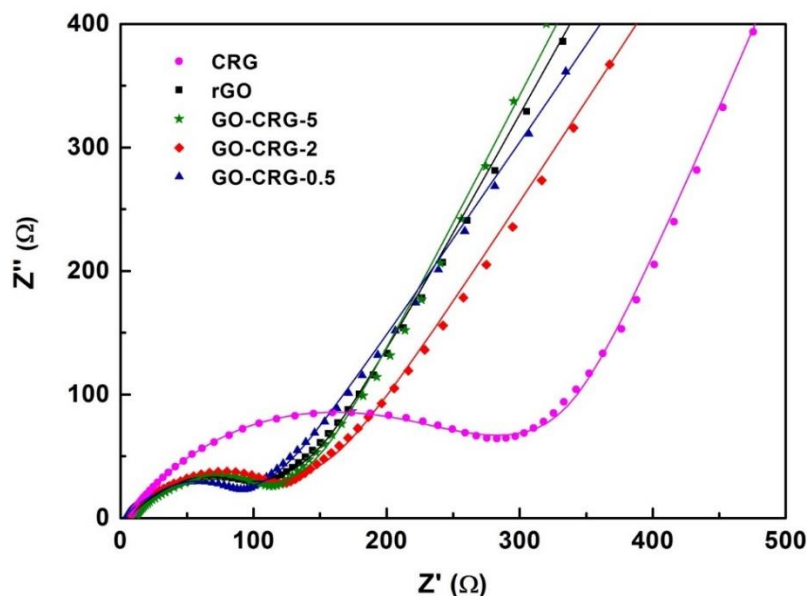


Figure 3.9 Nyquist plots of graphene cryogel papers and the CRG papers.

3.4 Conclusion

In summary, flexible graphene paper with porous structure has been fabricated by mechanically pressing a graphene cryogel, which was made from precursor solution with different CRG/GO ratios. The mechanical properties of such graphene paper can be significantly enhanced with the increase of CRG/GO ratio in the precursor solution. The introduction of CRG in the precursor solution resulted in a strong graphene paper without sacrificing its electrochemical performance. They all exhibit enhanced electrochemical properties compared to that graphene paper fabricated by filtration, i.e. high discharge capacity, good rate capability and cycling stability. The improved

performance is originated from the easy accessibility and transportation of lithium ions in the folded and porous structure. These graphene papers show promise as a new class of flexible electrodes for wearable or rolling-up devices.

3.5 References

- [1] A. Peigney, C. Laurent, E. Flahaut, R.R. Bacsa, A. Rousset, Specific Surface Area of Carbon nanotubes and Bundles of Carbon nanotubes, *Carbon*, 39 (2001) 507-514.
- [2] S.V. Morozov, K.S. Novoselov, M.I. Katsnelson, F. Schedin, D.C. Elias, J.A. Jaszczak, A.K. Geim, Giant Intrinsic Carrier Mobilities in Graphene and Its Bilayer, *Physical Review Letters*, 100 (2008) 016602 (1-4).
- [3] M.D. Stoller, S.J. Park, Y.W. Zhu, J.H. An, R.S. Ruoff, Graphene-Based Ultracapacitors, *Nano Letters*, 8 (2008) 3498-3502.
- [4] E. Yoo, J. Kim, E. Hosono, H. Zhou, T. Kudo, I. Honma, Large Reversible Li Storage of Graphene Nanosheet Families for use in Rechargeable Lithium ion Batteries, *Nano Letters*, 8 (2008) 2277-2282.
- [5] D.A. Dikin, S. Stankovich, E.J. Zimney, R.D. Piner, G.H.B. Dommett, G. Evmenenko, S.T. Nguyen, R.S. Ruoff, Preparation and Characterization of Graphene Oxide Paper, *Nature*, 448 (2007) 457-460.
- [6] H. Chen, M.B. Mueller, K.J. Gilmore, G.G. Wallace, D. Li, Mechanically Strong, Electrically Conductive, and Biocompatible Graphene Paper, *Advanced Materials*, 20 (2008) 3557-3561.
- [7] S. Park, K.-S. Lee, G. Bozoklu, W. Cai, S.T. Nguyen, R.S. Ruoff, Graphene Oxide Papers Modified by Divalent Ions—Enhancing Mechanical Properties via Chemical Cross-Linking, *ACS Nano*, 2 (2008) 572-578.
- [8] E. Yoo, J. Kim, E. Hosono, H.-s. Zhou, T. Kudo, I. Honma, Large Reversible Li Storage of Graphene Nanosheet Families for Use in Rechargeable Lithium Ion Batteries, *Nano Letters*, 8 (2008) 2277-2282.
- [9] C. Wang, D. Li, C.O. Too, G.G. Wallace, Electrochemical Properties of Graphene Paper Electrodes Used in Lithium Batteries, *Chemistry of Materials*, 21 (2009) 2604-2606.
- [10] Z. Niu, J. Chen, H.H. Hng, J. Ma, X. Chen, A Leavening Strategy to Prepare Reduced Graphene Oxide Foams, *Advanced Materials*, 24 (2012) 4144-4150.
- [11] X. Zhao, C.M. Hayner, M.C. Kung, H.H. Kung, Flexible Holey Graphene Paper Electrodes with Enhanced Rate Capability for Energy Storage Applications, *Acs Nano*, 5 (2011) 8739-8749.

- [12] Y.-C. Yong, X.-C. Dong, M.B. Chan-Park, H. Song, P. Chen, Macroporous and Monolithic Anode Based on Polyaniline Hybridized Three-Dimensional Graphene for High-Performance Microbial Fuel Cells, *ACS Nano*, 6 (2012) 2394-2400.
- [13] X. Yang, J. Zhu, L. Qiu, D. Li, Bioinspired Effective Prevention of Restacking in Multilayered Graphene Films: Towards the Next Generation of High-Performance Supercapacitors, *Advanced Materials*, 23 (2011) 2833-2838.
- [14] F. Liu, S. Song, D. Xue, H. Zhang, Folded Structured Graphene Paper for High Performance Electrode Materials, *Advanced Materials*, 24 (2012) 1089-1094.
- [15] N.V. Medhekar, A. Ramasubramaniam, R.S. Ruoff, V.B. Shenoy, Hydrogen Bond Networks in Graphene Oxide Composite Paper: Structure and Mechanical Properties, *Acs Nano*, 4 (2010) 2300-2306.
- [16] D. Li, M.B. Muller, S. Gilje, R.B. Kaner, G.G. Wallace, Processable Aqueous Dispersions of Graphene Nanosheets, *Nat Nano*, 3 (2008) 101-105.
- [17] T. Cosgrove, *Colloid Science : Principles, Methods and Applications* (2nd Edition), Wiley-Blackwell, Hoboken, NJ, USA, 2010.
- [18] A. Abouimrane, O.C. Compton, K. Amine, S.T. Nguyen, Non-Annealed Graphene Paper as a Binder-Free Anode for Lithium-Ion Batteries, *Journal of Physical Chemistry C*, 114 (2010) 12800-12804.
- [19] O.C. Compton, D.A. Dikin, K.W. Putz, L.C. Brinson, S.T. Nguyen, Electrically Conductive "Alkylated" Graphene Paper via Chemical Reduction of Amine-Functionalized Graphene Oxide Paper, *Advanced Materials*, 22 (2010) 892-896.
- [20] S. Stankovich, R.D. Piner, X. Chen, N. Wu, S.T. Nguyen, R.S. Ruoff, Stable Aqueous Dispersions of Graphitic Nanoplatelets via the Reduction of Exfoliated Graphite Oxide in the Presence of Poly(sodium 4-styrenesulfonate), *Journal of Materials Chemistry*, 16 (2006).
- [21] O.C. Compton, B. Jain, D.A. Dikin, A. Abouimrane, K. Amine, S.T. Nguyen, Chemically Active Reduced Graphene Oxide with Tunable C/O Ratios, *Acs Nano*, 5 (2011) 4380-4391.
- [22] T. Piao, S.M. Park, C.H. Doh, S.I. Moon, Intercalation of Lithium Ions into Graphite Electrodes Studied by AC Impedance Measurements, *Journal of The Electrochemical Society*, 146 (1999) 2794-2798.

4 Flexible Free-standing Graphene Paper with Interconnected Porous Structure for Energy Storage

This chapter is adapted from the research article entitled “Flexible free-standing graphene paper with interconnected porous structure for energy storage” by Shu, K.; Wang, C.; Li, S.; Zhao, C.; Yang, Y.; Liu, H.; Wallace, G. in *Journal of Materials Chemistry A* **2015**, *3* (8), 4428-4434. (link: <http://pubs.rsc.org/en/content/articlelanding/2015/ta/c4ta04324c>). Reproduced by permission of The Royal Society of Chemistry.

4.1 Introduction

Flexible binder-free graphene or graphene composite electrodes can be easily fabricated due to the large aspect ratio of graphene sheets. These electrodes have found applications in flexible batteries/supercapacitors [1-4]. The restacking of graphene sheets due to strong $\pi - \pi$ interactions during the fabrication process deteriorates the performance as the accessible surface area is decreased limiting the electrochemical properties. Thus prevention of aggregation of graphene sheets becomes a vital challenge in constructing such macroscopic structures. Several strategies have been developed to inhibit the restacking of graphene sheets. The incorporation of spacers can enable the graphene sheets to remain largely separated in the bulk graphene paper materials. Spacers used can be surfactants, polymers, nanoparticles and even water [5-8]. An alternative strategy is to create graphene macroscopic materials with three-dimensional porous networks with increased accessible surface area and enhanced ion diffusion. The

approaches to construct such porous graphene macroassembly include: hydrothermal [9], template-directed CVD, organic sol-gel [10, 11] and freeze drying [12-14].

Freeze-drying is a simple, versatile, low-cost and environmentally friendly fabrication technique for porous structures [15]. In this process, solutions are frozen in a cold trap, and followed by removal of the frozen solvents via sublimation under vacuum, leading to the formation of porous structures. This technology has been widely used to fabricate porous structure for tissue engineering and biological applications [16]. Recently, freeze casting has been utilized to create porous graphene structures. An aqueous dispersion of polymer stabilized graphene was used to fabricate highly-ordered three-dimensional architecture with microchannels oriented along the freezing direction via directional freeze casting [12]. By quickly freezing the graphene dispersion, followed by a freeze casting process, ultralight graphene based aerogels with monolith three-dimensional framework can be prepared [14]. The graphene monoliths can be made superelastic via tuning the reduction level of the graphene precursor and controlling the freeze casting conditions [13]. However, such produced macroscopic graphene aerogel generally possesses large pore sizes (over 150 μm), ultra-low density and mechanical fragility.

In the previous chapter (Chapter 3), a mechanical pressing procedure was applied to graphene aerogel, forming paper-like electrodes. Unfortunately, the porous structure was partly lost [17]. Therefore, attention was turned to preparing porous graphene paper without the need for pressing. This work is the topic considered in this chapter. Consideration was given to the development of a very simple freeze casting method to prepare graphene paper with uniform porous structure. Using wet graphene “gel” with certain water content as precursor, a novel porous graphene (PG) paper can be prepared via a freeze casting process. Such PG paper can be used as binder-free

electrodes for lithium battery and all-solid-state supercapacitors. This PG paper displayed excellent performance as either an anode in lithium ion battery or an electrode in all-solid-state supercapacitor.

4.2 Experimental Specific to This Chapter

4.2.1 Fabrication of porous graphene paper

Graphite oxide was synthesized from natural graphite flakes by the modified Hummer's method, as described in Chapter 2. The obtained graphite oxide was subjected to ultrasonication using a Branson Digital Sonifier (S450D, 30% amplitude, 2s on, 1s off) for 30 min to obtain graphene oxide (GO). Graphene wet "gel" was formed by vacuum assisted filtration (using 0.22 μm polycarbonate membrane filters) of 1 mg mL⁻¹ GO dispersion. The resultant filter cake was quickly frozen by liquid nitrogen when it was still "wet". The water content in the wet "gel" was measured by thermogravimetric analysis. The frozen graphene gel was then subjected to freeze-drying overnight in a freeze drier (Christ Alpha 1-2 LD plus). The as-prepared GO paper was thermally reduced at 220°C in air for 2h, followed by further reduction with 5% ascorbic acid solution for 6h at 60 °C. Two types of wet "gel" precursor, containing 92% and 87% water, were used in this work. The resultant graphene paper was named G-92, G-87, respectively. For comparison, graphene paper from air dried wet "gel" was also prepared. It was named as G-air paper.

4.2.2 Device assembly

Solid-state polymer electrolyte was prepared by a solvent casting method. PVA was dissolved in Milli-Q water to form ~10 wt% solution at 90°C under vigorous

stirring until the solution became clear, then an appropriate amount of H_2SO_4 (PVA- H_2SO_4 weight ratio 1:1) was added into the hot solution and stirred at room temperature overnight. For lithium battery tests, PG, G-87 and G-air paper was assembled into coin cells coupled with lithium metal. To assemble flexible all-solid-state supercapacitor, PG paper was firstly pasted onto a gold-coated PET substrate. The polymer electrolyte was poured onto the as-prepared electrode and dried at room temperature for 12 h. Two such electrodes were assembled together using polymer electrolyte as the glue (Figure 4.1).

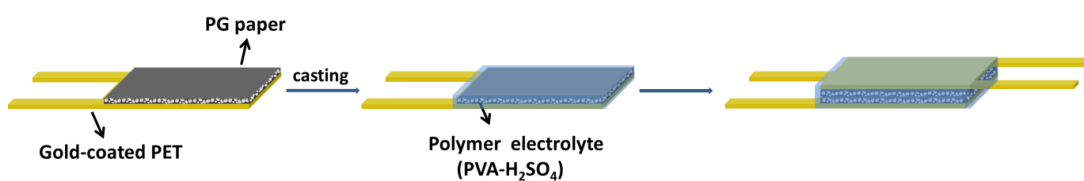


Figure 4.1 Schematic procedure to fabricate a flexible all solid-state supercapacitor.

4.3 Results and Discussion

4.3.1 Characterization of graphene oxide

The prepared graphene oxide was firstly analysed by X-Ray photoelectron spectroscopy (XPS). Typically, the C1s spectrum of graphene oxide consists of four components reflecting carbon atoms at different chemical states (Figure 4.2a) [18]. The non-oxygenated ring C (C-C), C in C-O bonds, carbonyl C (C=O) and carboxylate C (O-C=O) appeared at 284.8 eV, 286.8 eV, 287.8 eV and 288.6 eV, respectively [19]. The carbon/oxygen (atomic) ratio obtained from XPS was 7:3, indicating a considerable degree of oxidation. Atomic force microscopy showed that the evaporated graphene oxide dispersion casted on silicon wafer consisted of isolated graphene sheets. Although the theoretical thickness of one single layered graphene sheet is ~ 0.34 nm, the graphene

oxide sheets especially hydrated GO sheets are expected to be thicker (around 1 nm) due to the presence of functional groups and absorbed water molecular [18]. Our graphene nanosheets are several hundred nanometres in lateral dimension and ~1.2 nm in thickness indicating the successful exfoliation of graphite oxide (Figure 4.2b).

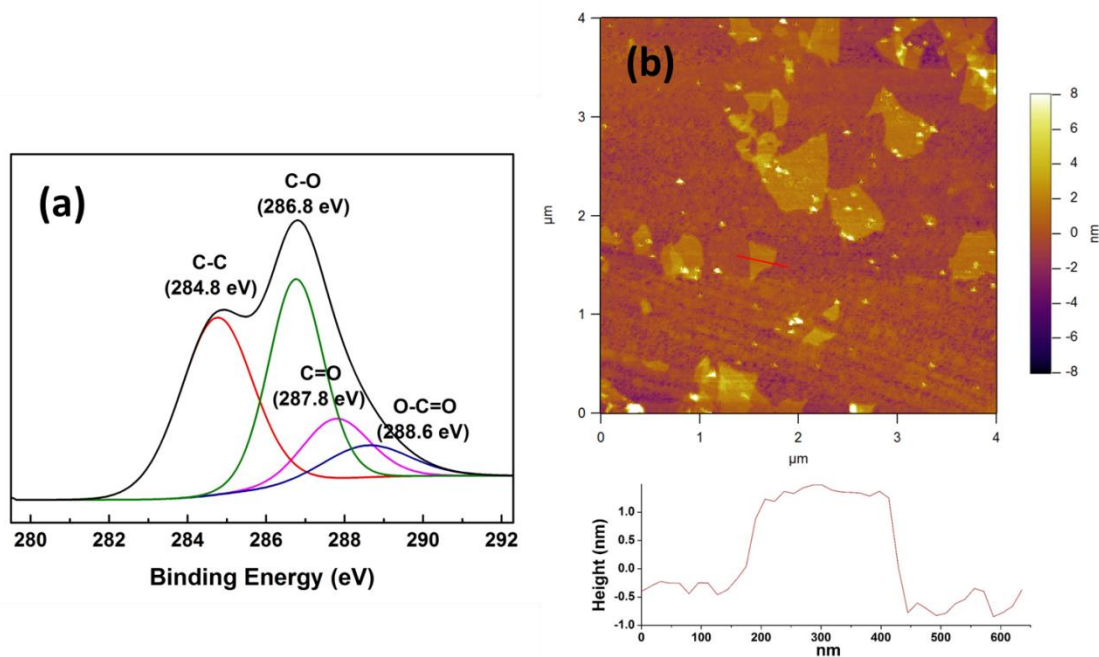


Figure 4.2 (a) XPS spectrum of graphene oxide; (b) AFM image and height profile of graphene oxide.

4.3.2 Physiochemical characterization of porous graphene paper

Figure 4.3a shows the morphology of the cross-section of PG, G-87 and G-air graphene paper (Figure 4.3). The G-92 paper exhibits a continuous porous network with pore size around several micrometres, quite similar to the freeze dried graphene foam [20]. To denote such porous structure, we label G-92 paper as PG. This PG paper demonstrates a porous structure after the thermal reduction and wet chemical reduction (Figure 4.3a). It is mechanical robust, as evidenced by the well-maintained structure integrity even after being constructed into a LIB and subjected to 100 charge/discharge

cycles (Inset of Figure 4.3a). G-87 paper displayed a loosely packed layered structure with micro-scale interspaces (Figure 4.3b), while the air dried graphene paper (G-air) presented a more compact layered structure with larger interspaces (Figure 4.3c). Due to its high porosity, the thickness of PG paper can be as high as approximately 150 μm . Not surprisingly, the formation of a layered structure resulted in thickness shrinkage. The thickness of G-87 paper and G-air paper was $\sim 15 \mu\text{m}$ and $\sim 10 \mu\text{m}$, respectively, only 1/10 and 1/15 of the PG paper's thickness. Interestingly, such highly porous graphene papers (PG, G-92) were still flexible (Figure 4.3d). The conductivity of the PG paper was $\sim 10 \text{ S m}^{-1}$.

The formation of porous structure is highly related to water content in the gel-like graphene precursor. When well dispersed in aqueous solution, GO is randomly distributed in an isotropic phase through hydrogen bonding with water molecules. The GO sheets begin to align as the concentration increases, forming a dense stacked GO film after drying due to π - π interactions [21, 22]. When the gel-like graphene oxide precursor with high water content is frozen by liquid nitrogen, the extremely low temperature leads to rapid formation of ice nuclei and growth of small ice crystals [23]. This prevents the GO sheets from restacking, thus hindering the formation of a layered structure. The sublimation of such ice crystals results in the formation of a continuous porous structure, as observed in the PG paper. If the water content in the precursor is decreased, the accumulation of graphene sheets caused by π - π interaction becomes more severe and hinders the formation of small ice crystals, leading to the partial formation of a layered structure. This could explain the loosely packed layered structure formed in G-87 paper. For G-air paper without freeze drying, the compact graphene layered structure was completely formed with the evaporation of water. The large interspaces between

layers of G-air paper were obtained just because of the release of gas during the thermal reduction process.

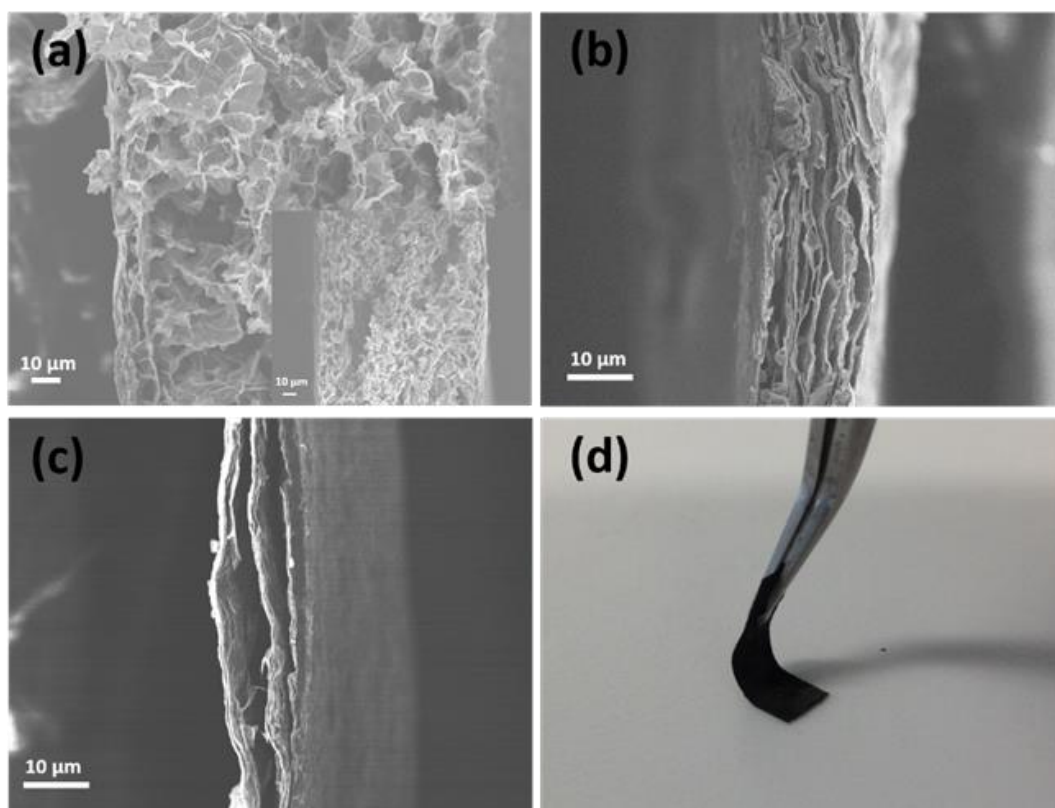


Figure 4.3 SEM images of the cross-section of (a) PG paper, (b) G-87 paper and (c) air dried graphene paper; Photograph of PG paper (d). (Figure 4.3a inset: SEM image of cycle PG paper.)

Figure 4.4a shows the XRD patterns of GO and PG paper. The GO paper shows a strong and sharp peak at 10.0° , corresponding to a d -spacing of 0.88 nm. The PG paper displays a broad and weak peak at around 24° . The d -spacing for PG paper decreased to 0.37 nm due to the removal of oxygen-containing functional groups between the interlayer of graphene sheets. Compared to that for filtrated graphene paper, the peak in PG paper is broader and weaker, indicating a less ordered state brought about by the porous structure [24]. The Raman spectra of GO and PG paper are

presented in Figure 4b. The G band corresponds to the first order scattering of the E_{2g} mode and D band can be attributed to the disordered structures. They appear at 1583 and 1334 cm^{-1} , respectively [25]. The D/G intensity ratio was 1.20 for GO, and 1.40 for PG. Such D/G ratio change can be attributed to the decrease in the average size of sp^2 domains upon the reduction process.

Figure 4c shows typical TGA curves of GO paper and PG paper which are similar to other GO and reduced GO materials. The hydrophilic GO paper demonstrated a ~10 % weight loss below 100 °C due to evaporation of absorbed water. The major weight loss of GO paper occurred between 100-200 °C, and it was ~30 %. This weight loss was caused by pyrolysis of oxygen-containing groups [26]. The negligible weight loss within this temperature range for PG paper indicates the successful reduction of GO paper. The weight loss of PG and GO paper in the temperature range of 200 °C to 500 °C is about 10%, which can be attributed to the decomposition of some residual oxygen-containing groups [27]. The Raman Spectra, TGA curves of G-87 and G-air paper are not shown here due to their similarity.

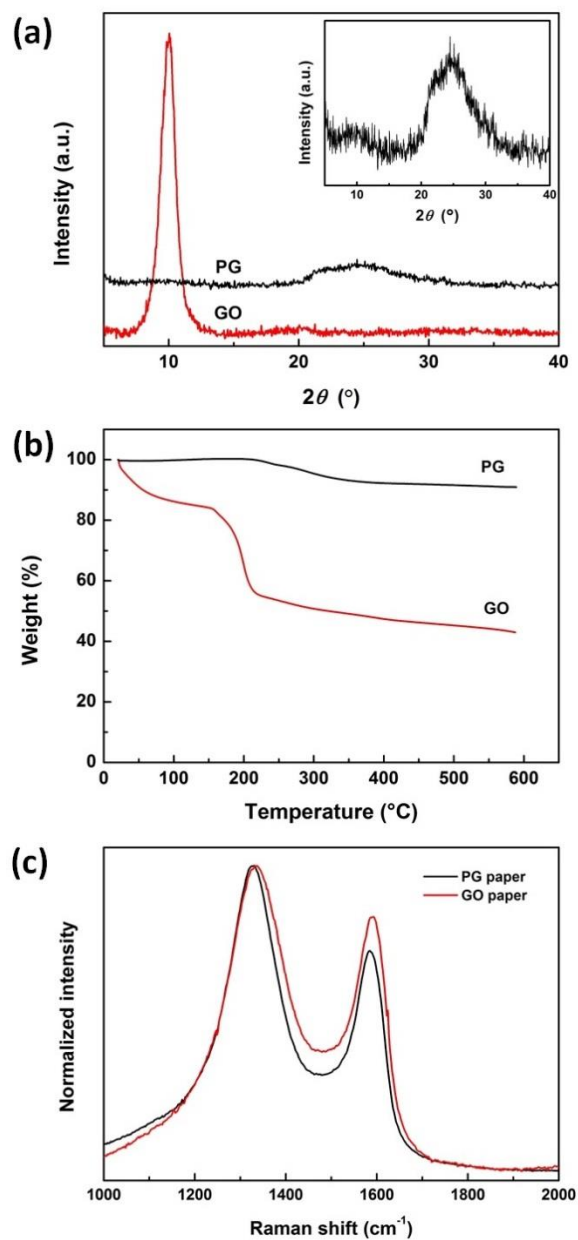


Figure 4.4 XRD patterns (a), Raman spectra (b), and TGA curves (c) of GO and PG papers [Figure 4a inset: expanded peak view for PG paper (5-40 $^\circ$)].

4.3.3 Electrochemical performance as a lithium-ion battery anode

The performance of PG paper as a binder-free electrode for lithium-ion batteries was studied by galvanostatic charge/discharge test in the potential range from 0.005 to 3.0V. The PG paper electrode shows a very high first discharge capacity of 1200 mAh

g^{-1} (Figure 4.5a). The value of the discharge capacity slightly decreases to 1056 mAh g^{-1} at the second cycle, 88% of the initial capacity is retained. The irreversible capacity loss around 0.75V at the first cycle could be attributed to the formation of solid electrolyte interface (SEI) layer and the reaction of lithium ions with residual oxygen-containing functional groups [28]. The interconnected three dimensional porous structures in our graphene paper can provide more lithium insertion active sites, thus lead to much higher reversible capacity compared to other graphene papers. The shape of the CV curves is in good agreement with the charge/discharge curves (Figure 4.5b). The lithium intercalation occurs in the potential range below 0.5 V , which became weaker after the first cycle due to the lithium intercalation reaction being partially reversible. The cathodic peak around 0.75V , which only appears in the first cycle, indicates the formation of SEI. The cathodic peak at about 1.5 V can be attributed to lithium interactions with the residual functional groups on the surface or at the edge sites of graphene sheets. The G-87 paper as an anode for lithium battery was used here for comparison, which only delivered a first discharge capacity of 1260 mAh g^{-1} and second discharge capacity of 841 mAh g^{-1} (Figure 4.5c). Much worse performance is presented by G-air paper, which shows a first charge capacity of 894 mAh g^{-1} and second discharge capacity of only 287 mAh g^{-1} (Figure 4.5d). The low coulombic efficiency ($<30\%$) of the G-air paper during the first discharge/charge cycle may be ascribed to the reduced active sites and limited electrolyte infiltration into the interior of the highly restacked graphene sheets, which has been discussed in Chapter 3.

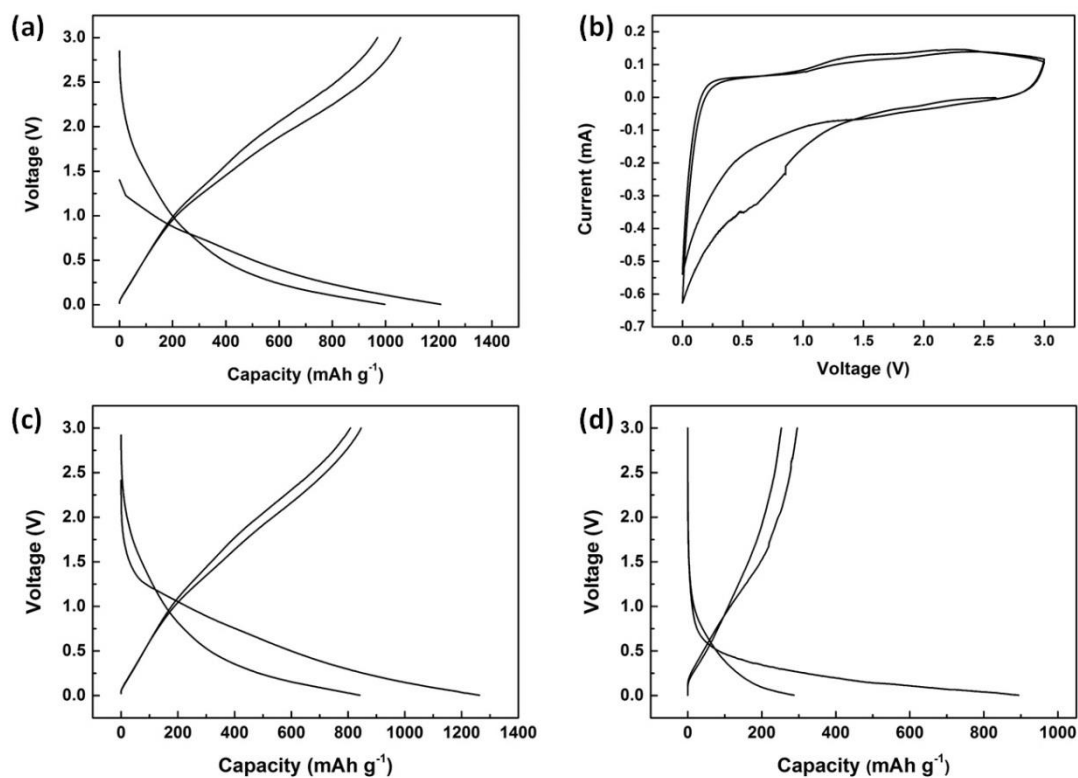


Figure 4.5 First and second charge/discharge curves of PG paper (a), G-87 papers (c) and G-air paper (d); (b) Cyclic voltammograms obtained for PG paper at a scan rate of 0.1 mV s^{-1} .

The porous structure of the graphene paper also leads to a good rate capability. As can be clearly seen from Figure 4.6a, these graphene papers possess high rate discharge/charge capability, which is likely due to the enhanced access of electrolyte benefited from the unique porous structure. At a current density of 200, 500, 1000 and 2000 mA g^{-1} , the corresponding reversible capacity can reach 683, 600, 518 and 428 mAh g^{-1} , respectively. The G-87 paper presents much worse rate performance, with a capacity of 394, 314, 257 and 199 mAh g^{-1} at the same current densities.

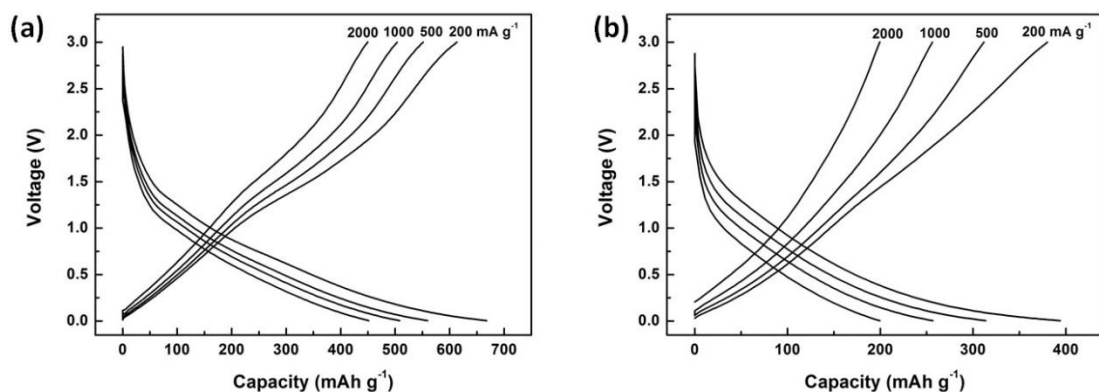


Figure 4.6 Charge/discharge curves of PG paper (a) and G-87 paper (b) at different current densities.

The PG paper demonstrated a good cyclic performance and reversibility (Figure 4.7a). After 100 cycles, our PG paper electrodes still maintained a specific capacity of 420 mAh g⁻¹ at a current density of 2000 mA g⁻¹. Meanwhile, the specific capacity retained of G-87 paper was only 189 mAh g⁻¹ under the same conditions. Figure 4.7b shows the Nyquist plot of PG paper measured after 100 cycles. For the cycled lithium-ion battery, typically there's only one semicircle in the medium-high frequency region, representing charge-transfer impedance/resistance at the electrode/electrolyte interface. The inclined line at an approximate 45° angle to the real axis corresponds to the lithium-diffusion process within the carbon electrodes. This can be clearly seen from the EIS curves. The diameter of the semicircle at the medium frequency region of the PG papers is significantly reduced compared to the graphene paper obtained by filtration, indicative of a lower charge-transfer resistance. The reduced charge transfer resistance might be induced by the easy accessibility and transportation of electrolyte in the continuous porous structure.

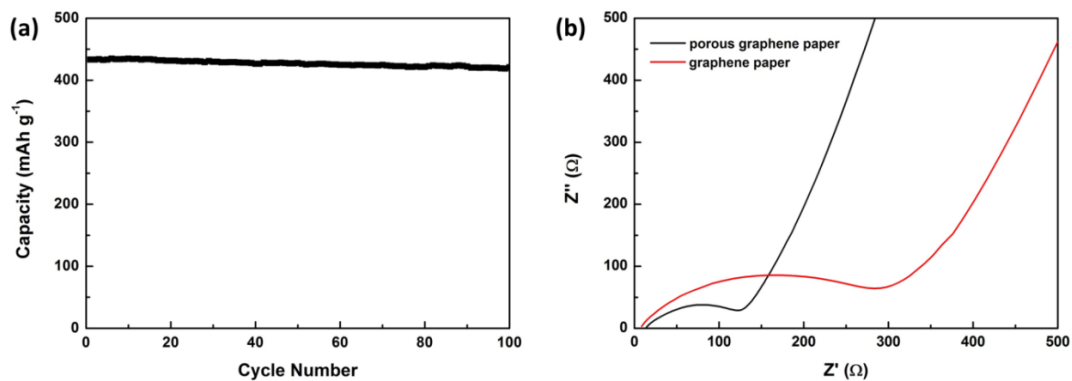


Figure 4.7 (a) Capacity versus cycle number for PG paper at 2000 mA g⁻¹. (b) Nyquist plots of PG paper and the graphene paper (filtration).

4.3.4 Graphene paper based flexible all-solid-state supercapacitor

The assembled PG paper based all-solid-state supercapacitor was tested by cyclic voltammetry and galvanostatic charge/discharge (Figure 4.8a). To study the correlation between the structure and performance, G-87 paper and G-air paper based supercapacitors were also evaluated for comparison (Figure 4.8b, c). The CV curve of PG based supercapacitor shows a near rectangular shape at a low scan rate of 10 mV s⁻¹. At a higher scan rate of 50 mV s⁻¹, a CV loop with a large oblique angle appears. The estimated specific capacitances for a single electrode calculated from the CV curves for PG paper was ~148 F g⁻¹ and ~74 F g⁻¹ at a scan rate of 10 mV s⁻¹ and 50 mV s⁻¹, respectively. A highly distorted CV shape was presented by G-87 paper, indicating its poor capacitive performance. A very low specific capacitance was presented by G-87 paper, which was only ~36 F g⁻¹ at 10 mV s⁻¹ (Figure 4.8b). For the G-air paper, the capacitance presented at 10 mV s⁻¹ was negligible (Figure 4.8c).

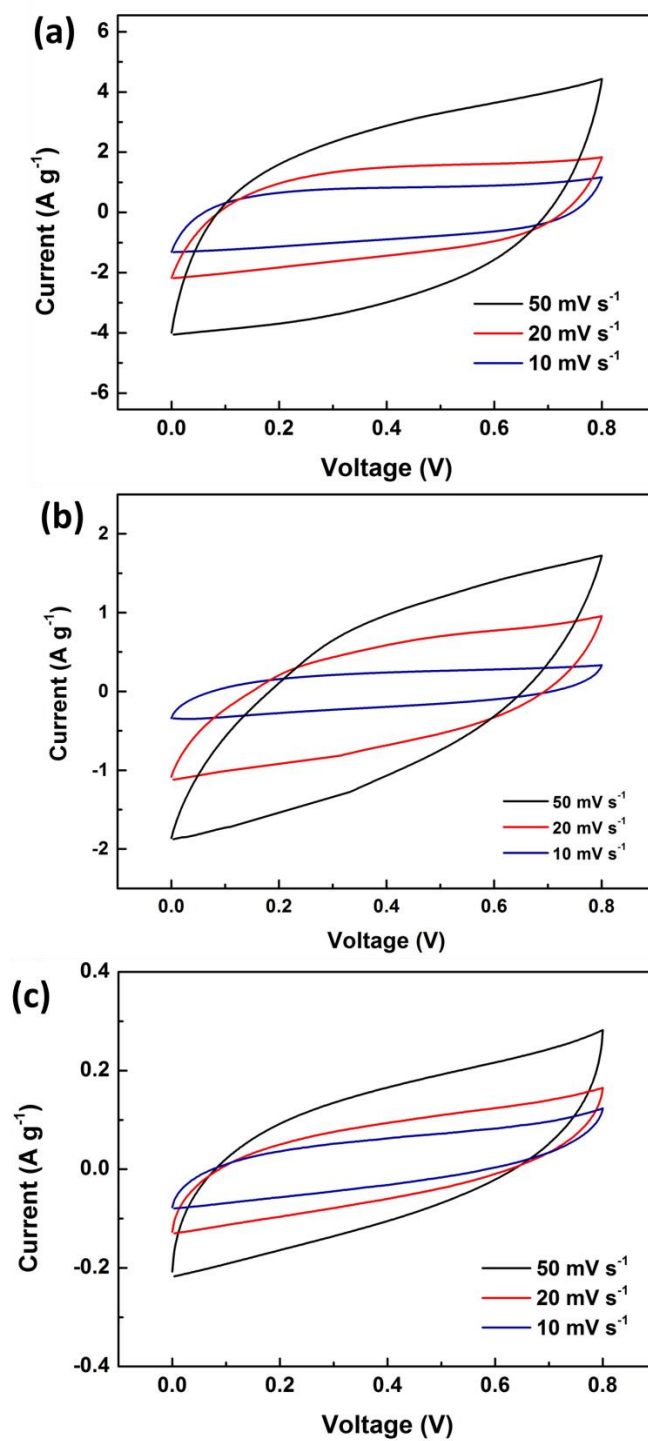


Figure 4.8 Cyclic voltammograms of PG paper (a), G-87 paper (b), and G-air paper (c) at different scan rates.

The PG paper presented a nearly straight discharge curve in the charge/discharge test, showing its good electrical double layer performance (Figure 4.9a). The calculated specific capacitance of the flexible PG supercapacitor was about 156 F g^{-1} at 0.5 A g^{-1} . The capacitance decreased to 105 F g^{-1} at a higher current density of 2 A g^{-1} . The PG paper based solid-state supercapacitor showed an equivalent performance compared to most of the previously reported carbon nanotube based solid-state devices and neat graphene paper/film based conventional supercapacitors [29-32]. G-87 paper and G-air paper based flexible supercapacitors were also tested for comparison. The respective specific capacitances presented by G-87 paper and G-air paper were only 30 F g^{-1} and 5 F g^{-1} at 0.5 A g^{-1} (Figure 4.9a, dotted line and dash line). The capacitance value was negligible when the current density increased to 2 A g^{-1} (Figure not shown here). The porous structure inside the PG paper offers enhanced access for polymer electrolyte, thus facilitating ionic transportation.

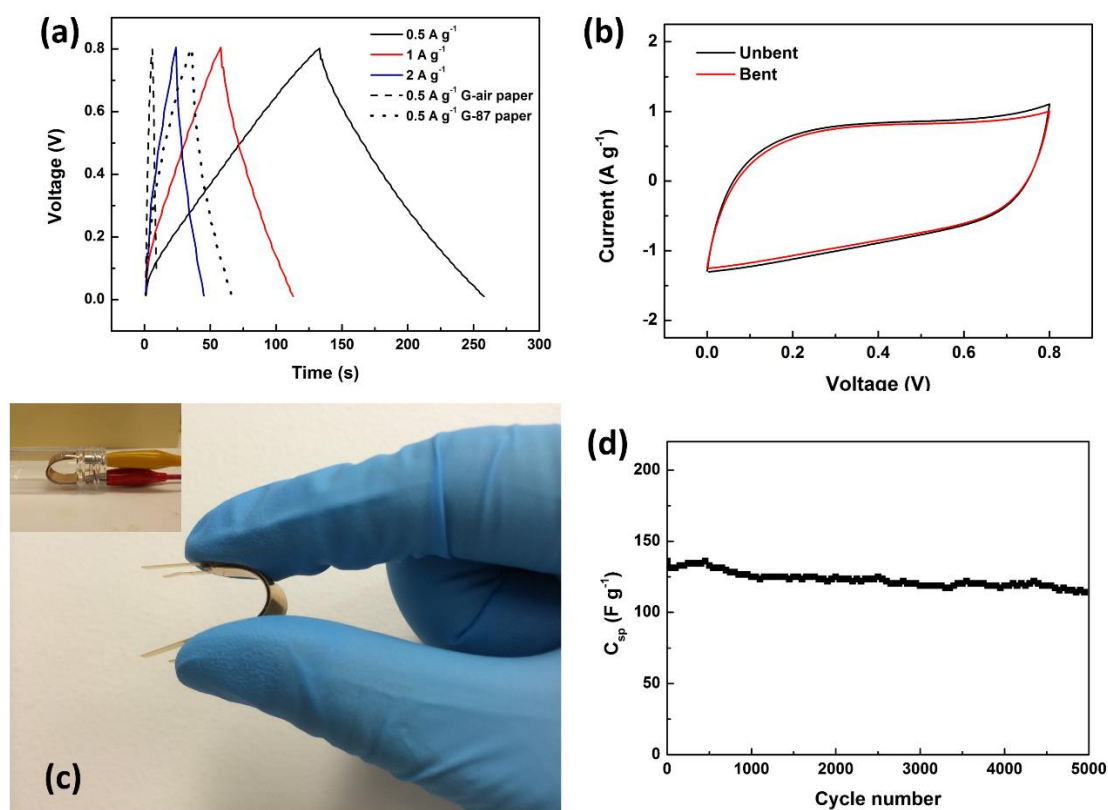


Figure 4.9 (a) Charge/discharge curves of PG paper (solid line), G-87 paper (dotted line) and G-air paper (dash line) based flexible supercapacitors; (b) CV curves of the bent and unbent device at a scan rate of 10 mV s^{-1} ; (c) Photograph of the bent flexible PG paper based supercapacitor; (d) Cycle stability of the PG paper device at a current density of 1 A g^{-1} .

This flexible supercapacitor also exhibited good mechanical robustness in the bending test. It could be repeatedly bent without causing any significant variations in the specific capacitance. The CV curves obtained at the bent and unbent status show nearly the same capacitive behaviour (Figure 4.9b), indicating that the change of electrochemical properties is negligible under bending. To further characterize the cycle stability of the solid-state device, galvanostatic charge/discharge tests were carried out up to 5000 cycles at a current density of 1 A g^{-1} . Remarkably, $\sim 81 \%$ of the initial

capacitance was retained, and the calculated Coulombic efficiency was always kept in the range of 98-100% throughout the testing cycles (Figure 4.9d).

The capacitive features of graphene papers were further studied by EIS. Figure 4.10 presents the Nyquist plots of PG, G-87 and G-air paper obtained in the frequency range between 0.01 and 100 kHz. The equivalent circuit model used to fit the impedance spectra is shown in Figure 4.10 as an inset, which includes solution resistance R_s , double layer resistance R_{dl} , imperfect double layer capacitance CPE_{dl} and Warburg element W_o . The equivalent series resistance (ESR) can be evaluated from the EIS test via linear interpolation of the low-frequency part of the Nyquist plot to $Z_{Im}=0$ [33]. The ESR for PG, G-87 and G-air paper was 26, 39 and 47 Ω , respectively, corresponding to their different capacitive performance. The linear part at low frequency region in Nyquist plot corresponds to the Warburg element W_o , which reflects ion diffusion between electrodes. More vertical the plot is, the capacitive performance of electrode is closer to the ideal model [34]. It can be found that among the electrodes, PG paper showed the most vertical curve, which indicates its better ion diffusion due to the porous structure. According to the previous report, an electrochemical approach named dynamic electrosorption analysis (DEA) can be used to standardize the ion adsorption and transport behaviour in bulk graphene materials. The capacitance against frequency plotted from EIS shown in Figure 4.10, can be viewed as a form of DEA. The relative ion-transport rate within a porous electrode can be characterised by the characteristic relaxation time constant τ_0 , which is the reciprocal of frequency at which the capacitance is 50% of its maximum value. The τ_0 of PG, G-87 and G-air paper was 0.63, 10 and 15.8 s, respectively. The PG paper has the smallest τ_0 among these three samples, which can be ascribed to the facilitated ionic transport induced by its porous structure.

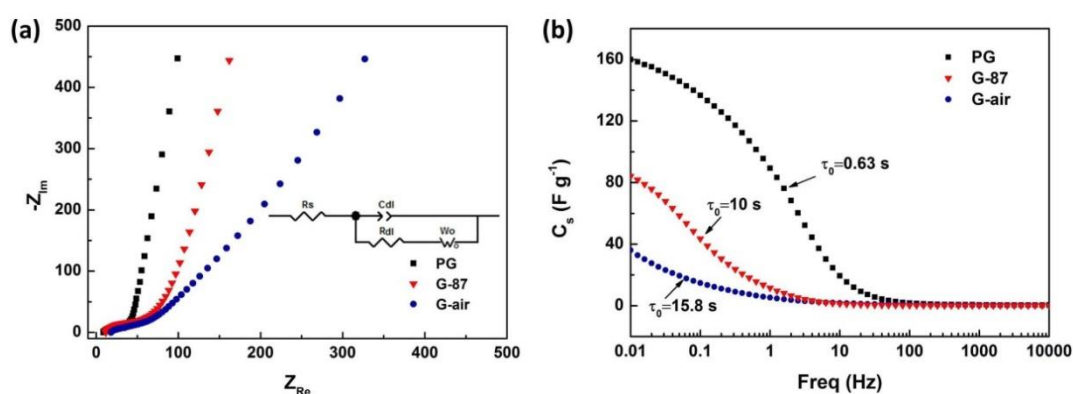


Figure 4.10 Nyquist plots (a) (scatter: experimental plots, line: fitting plots), and capacitance versus frequency (b) of PG, G-87 and G-air paper. (a inset: equivalent circuit model)

The ragone plot (Figure 4.11) compares the power and energy capability of PG paper with other all-solid-state graphene (or carbon nanotube) based supercapacitors. The energy and power density are calculated using the following equations: $E = C_s \Delta V^2 / 7200$, $P = 3600E/t$. The PG paper afforded a maximum energy density of 14 Wh kg⁻¹ at a power density of 0.32 kW kg⁻¹, while it maintained 7.1 Wh kg⁻¹ at an increased power density of 5.1 kW kg⁻¹. The PG paper electrode displayed higher energy density compared to the reported all-solid-state flexible supercapacitors based on graphene cellulose [35], flexible graphene hydrogel [32], folded graphene paper [20] and graphene/PEDOT:PSS film [36].

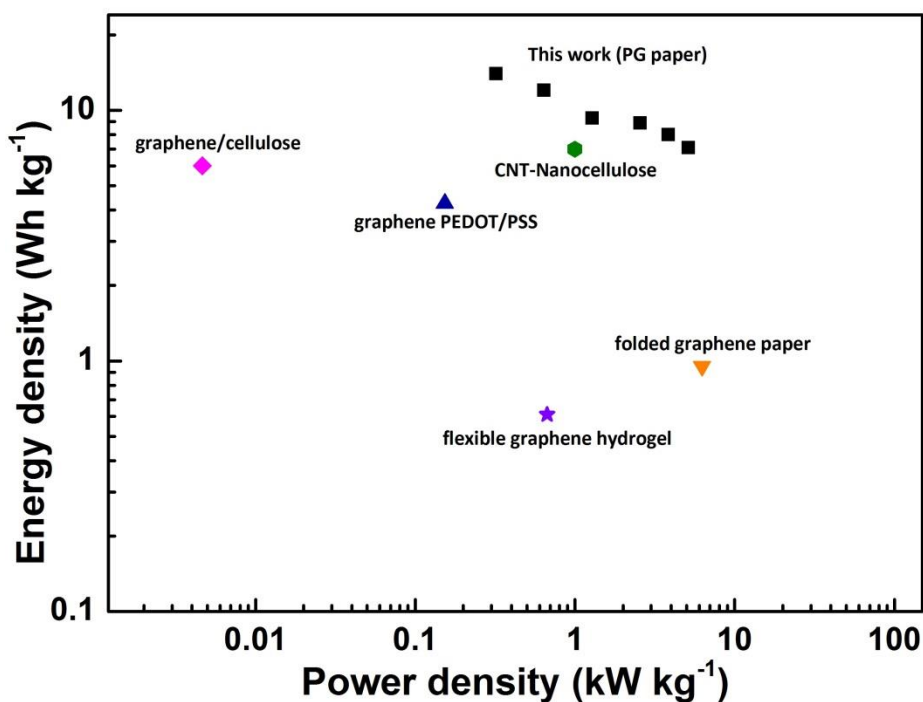


Figure 4.11 Ragone plot of PG papers in comparison with the reported graphene-based all-solid-state supercapacitors.

4.4 Conclusion

A novel graphene paper with a continuous porous structure was prepared using a graphene wet-gel as the precursor and a simple lyophilisation process. The water content in the precursor graphene oxide gel was used to prevent the restacking of graphene sheets. The structure formed could be tuned from a loosely packed layered structure to a continuous connected porous network by varying the water content in the gel precursor. The porous graphene (PG) paper displayed an enhanced electrochemical performance in lithium batteries and all-solid-state supercapacitors. The highly interconnected 3D structure allows fast charge transfer and rapid ion diffusion, thus enhancing its electrochemical performance. This PG paper is mechanically robust and flexible; making it a promising electrode for use in wearable or rolling-up devices. Also,

its open porous structure allows the fabrication of porous graphene-based composites via incorporation with other functional materials into the void space.

4.5 References

- [1] A. Sumboja, C.Y. Foo, X. Wang, P.S. Lee, Large Areal Mass, Flexible and Free-Standing Reduced Graphene Oxide/Manganese Dioxide Paper for Asymmetric Supercapacitor Device, *Adv. Mater.*, 25 (2013) 2809-2815.
- [2] H.-P. Cong, X.-C. Ren, P. Wang, S.-H. Yu, Flexible Graphene-polyaniline Composite Paper for High-performance Supercapacitor, *Energy & Environmental Science*, 6 (2013) 1185-1191.
- [3] N. Jung, S. Kwon, D. Lee, D.-M. Yoon, Y.M. Park, A. Benayad, J.-Y. Choi, J.S. Park, Synthesis of Chemically Bonded Graphene/Carbon Nanotube Composites and their Application in Large Volumetric Capacitance Supercapacitors, *Adv. Mater.*, 25 (2013) 6854-6858.
- [4] C. Wang, D. Li, C.O. Too, G.G. Wallace, Electrochemical Properties of Graphene Paper Electrodes Used in Lithium Batteries, *Chemistry of Materials*, 21 (2009) 2604-2606.
- [5] S. Park, N. Mohanty, J.W. Suk, A. Nagaraja, J.H. An, R.D. Piner, W.W. Cai, D.R. Dreyer, V. Berry, R.S. Ruoff, Biocompatible, Robust Free-Standing Paper Composed of a TWEEN/Graphene Composite, *Adv. Mater.*, 22 (2010) 1736-1740.
- [6] G.K. Wang, X. Sun, F.Y. Lu, H.T. Sun, M.P. Yu, W.L. Jiang, C.S. Liu, J. Lian, Flexible Pillared Graphene-Paper Electrodes for High-Performance Electrochemical Supercapacitors, *Small*, 8 (2012) 452-459.
- [7] X. Yang, J. Zhu, L. Qiu, D. Li, Bioinspired Effective Prevention of Restacking in Multilayered Graphene Films: Towards the Next Generation of High-Performance Supercapacitors, *Advanced Materials*, 23 (2011) 2833-2838.
- [8] G. Zhou, D.-W. Wang, F. Li, L. Zhang, N. Li, Z.-S. Wu, L. Wen, G.Q. Lu, H.-M. Cheng, Graphene-Wrapped Fe₃O₄ Anode Material with Improved Reversible Capacity and Cyclic Stability for Lithium Ion Batteries, *Chemistry of Materials*, 22 (2010) 5306-5313.
- [9] Y. Xu, K. Sheng, C. Li, G. Shi, Self-Assembled Graphene Hydrogel via a One-Step Hydrothermal Process, *ACS Nano*, 4 (2010) 4324-4330.
- [10] X. Yang, L. Qiu, C. Cheng, Y. Wu, Z.-F. Ma, D. Li, Ordered Gelation of Chemically Converted Graphene for Next-Generation Electroconductive Hydrogel Films, *Angewandte Chemie International Edition*, 50 (2011) 7325-7328.

- [11] M.A. Worsley, P.J. Pauzauskie, T.Y. Olson, J. Biener, J.H. Satcher, T.F. Baumann, Synthesis of Graphene Aerogel with High Electrical Conductivity, *Journal of the American Chemical Society*, 132 (2010) 14067-14069.
- [12] J.L. Vickery, A.J. Patil, S. Mann, Fabrication of Graphene-Polymer Nanocomposites With Higher-Order Three-Dimensional Architectures, *Adv. Mater.*, 21 (2009) 2180-2184.
- [13] L. Qiu, J.Z. Liu, S.L.Y. Chang, Y. Wu, D. Li, Biomimetic Superelastic Graphene-based Cellular Monoliths, *Nat Commun*, 3 (2012) 1241 (1-7).
- [14] H. Sun, Z. Xu, C. Gao, Multifunctional, Ultra-Flyweight, Synergistically Assembled Carbon Aerogels, *Adv. Mater.*, 25 (2013) 2554-2560.
- [15] H. Zhang, I. Hussain, M. Brust, M.F. Butler, S.P. Rannard, A.I. Cooper, Aligned Two- and Three-dimensional Structures by Directional Freezing of Polymers and Nanoparticles, *Nat Mater*, 4 (2005) 787-793.
- [16] S.V. Madihally, H.W.T. Matthew, Porous Chitosan Scaffolds for Tissue Engineering, *Biomaterials*, 20 (1999) 1133-1142.
- [17] K. Shu, C. Wang, M. Wang, C. Zhao, G.G. Wallace, Graphene Cryogel Papers with Enhanced Mechanical Strength for High Performance Lithium Battery Anodes, *Journal of Materials Chemistry A*, 2 (2014) 1325-1331.
- [18] S. Stankovich, D.A. Dikin, R.D. Piner, K.A. Kohlhaas, A. Kleinhammes, Y. Jia, Y. Wu, S.T. Nguyen, R.S. Ruoff, Synthesis of Graphene-based Nanosheets via Chemical Reduction of Exfoliated Graphite Oxide, *Carbon*, 45 (2007) 1558-1565.
- [19] S. Stankovich, R.D. Piner, X. Chen, N. Wu, S.T. Nguyen, R.S. Ruoff, Stable Aqueous Dispersions of Graphitic Nanoplatelets via the Reduction of Exfoliated Graphite Oxide in the Presence of Poly(sodium 4-styrenesulfonate), *Journal of Materials Chemistry*, 16 (2006).
- [20] F. Liu, S. Song, D. Xue, H. Zhang, Folded Structured Graphene Paper for High Performance Electrode Materials, *Advanced Materials*, 24 (2012) 1089-1094.
- [21] W.F. Chen, L.F. Yan, Centimeter-Sized Dried Foam Films of Graphene: Preparation, Mechanical and Electronic Properties, *Adv. Mater.*, 24 (2012) 6229-6233.
- [22] J.I. Paredes, S. Villar-Rodil, A. Martinez-Alonso, J.M.D. Tascon, Graphene Oxide Dispersions in Organic Solvents, *Langmuir*, 24 (2008) 10560-10564.

- [23] L. Qian, H. Zhang, Controlled Freezing and Freeze drying: A Versatile Route for Porous and Micro-/nano-structured Materials, *Journal of Chemical Technology & Biotechnology*, 86 (2011) 172-184.
- [24] A. Abouimrane, O.C. Compton, K. Amine, S.T. Nguyen, Non-Annealed Graphene Paper as a Binder-Free Anode for Lithium-Ion Batteries, *The Journal of Physical Chemistry C*, 114 (2010) 12800-12804.
- [25] F. Tuinstra, J.L. Koenig, Raman Spectrum of Graphite, *The Journal of Chemical Physics*, 53 (1970) 1126-1130.
- [26] O.C. Compton, D.A. Dikin, K.W. Putz, L.C. Brinson, S.T. Nguyen, Electrically Conductive “Alkylated” Graphene Paper via Chemical Reduction of Amine-Functionalized Graphene Oxide Paper, *Adv. Mater.*, 22 (2010) 892-896.
- [27] H. Chen, M.B. Mueller, K.J. Gilmore, G.G. Wallace, D. Li, Mechanically Strong, Electrically Conductive, and Biocompatible Graphene Paper, *Adv. Mater.*, 20 (2008) 3557-3561.
- [28] E. Yoo, J. Kim, E. Hosono, H. Zhou, T. Kudo, I. Honma, Large Reversible Li Storage of Graphene Nanosheet Families for use in Rechargeable Lithium ion Batteries, *Nano Letters*, 8 (2008) 2277-2282.
- [29] B.G. Choi, J. Hong, W.H. Hong, P.T. Hammond, H. Park, Facilitated Ion Transport in All-Solid-State Flexible Supercapacitors, *ACS Nano*, 5 (2011) 7205-7213.
- [30] Z. Weng, Y. Su, D.-W. Wang, F. Li, J. Du, H.-M. Cheng, Graphene–Cellulose Paper Flexible Supercapacitors, *Advanced Energy Materials*, 1 (2011) 917-922.
- [31] Y.J. Kang, S.-J. Chun, S.-S. Lee, B.-Y. Kim, J.H. Kim, H. Chung, S.-Y. Lee, W. Kim, All-Solid-State Flexible Supercapacitors Fabricated with Bacterial Nanocellulose Papers, Carbon Nanotubes, and Triblock-Copolymer Ion Gels, *ACS Nano*, 6 (2012) 6400-6406.
- [32] Y. Xu, Z. Lin, X. Huang, Y. Liu, Y. Huang, X. Duan, Flexible Solid-State Supercapacitors Based on Three-Dimensional Graphene Hydrogel Films, *ACS Nano*, 7 (2013) 4042-4049.
- [33] S. Zhang, N. Pan, Supercapacitors Performance Evaluation, *Advanced Energy Materials*, 5 (2015) 1401401 (1-19).
- [34] J. Gamby, P.L. Taberna, P. Simon, J.F. Fauvarque, M. Chesneau, Studies and Characterisations of Various Activated Carbons used for Carbon/carbon Supercapacitors, *Journal of Power Sources*, 101 (2001) 109-116.

- [35] K. Gao, Z. Shao, J. Li, X. Wang, X. Peng, W. Wang, F. Wang, Cellulose nanofiber-graphene All Solid-state Flexible Supercapacitors, *Journal of Materials Chemistry A*, 1 (2013) 63-67.
- [36] Y. Liu, B. Weng, J.M. Razal, Q. Xu, C. Zhao, Y. Hou, S. Seyedin, R. Jalili, G.G. Wallace, J. Chen, High-Performance Flexible All-Solid-State Supercapacitor from Large Free-Standing Graphene-PEDOT/PSS Films, *Scientific Reports*, 5 (2015) 17045 (1-11).

5 Free-standing Graphene-Polypyrrole Hybrid Paper via Electropolymerization with an Enhanced Areal Capacitance

5.1 Introduction

Supercapacitors, due to their high power density and excellent cycling stability, are an important class of energy storage devices [1, 2]. An ideal flexible supercapacitor should hold a combination of excellent mechanical strength and large electrochemical capacitance. Due to their excellent electrical conductivity, chemical stability and high specific surface area, graphene based films or paper electrodes have shown remarkable flexibility with a high gravimetric capacitance in the range of 138 to 210 F g⁻¹ [3-5]. Although these graphene based flexible electrodes present promising gravimetric capacitance, they normally deliver a very low areal capacitance in the range of 57 to 94.5 mF cm⁻² due to their low areal mass loading (< 1 mg cm⁻²) [6, 7]. For practical usage, it is suggested that the areal mass loading should be at least 5 mg cm⁻² and the electrode thickness between 50-200 μm [8, 9]. One effective way to improve the areal capacitance is to introduce metal oxides with high theoretical capacitance. However, graphene/metal oxide hybrid electrodes normally suffer from poor conductivity. Excellent performance was achieved only at low scan rates. A MnO₂/carbon nanotube/textile nanostructure afforded a large areal capacitance of 2.8 F cm⁻² at a scan rate of 0.05 mV s⁻¹, but dropped sharply to 120 mF cm⁻² when the scan rate increased to 50 mV s⁻¹ [10].

Integration of electrically conducting polymers (ECPs) with graphene is an alternative way to achieve high areal capacitance. In addition, ECPs can be regarded as sustainable materials that can be derived from biomass, and meet the challenges of

energy sustainability for the future. In ECPs/graphene composites, ECPs can provide high pseudocapacitance, while graphene can provide a conductive network to overcome the poor cycling stability of ECPs. Polypyrrole (PPy) is one of the most widely used ECPs due to its good conductivity, facile synthesis, low cost and high charge storage [5, 11]. Flexible electrodes based on graphene/PPy composites present a high gravimetric capacitance ranging from 92 to 345 F g⁻¹ [12-14] and an areal capacitance from 152 to 175 mF cm⁻² [15, 16].

The graphene based flexible electrodes, prepared by the freeze drying method described in Chapter 4, present promising gravimetric capacitance, but unfortunately deliver a low areal capacitance due to their low areal loading mass. Therefore, further work was done to address this problem, as reported in this chapter.

In this work, a novel flexible PPy/chemically reduced graphene (CRG) hybrid paper with an enhanced areal capacitance was developed. PPy was incorporated into a paper-like graphene hydrogel via electropolymerization forming a layered structured CRG/PPy hybrid paper. The CRG-PPy paper with 3 times increased thickness can still maintain an equivalent gravimetric capacitance compared with that of neat CRG paper. It delivered a much higher areal capacitance of 440 mF cm⁻² at 0.5 A g⁻¹, in sharp contrast to 185 mF cm⁻² by neat CRG at the same current density. The capacitance slightly decreased to 356 mF cm⁻² when the current density increased to 6 A g⁻¹, indicating the excellent rate capability. Compared to the previously reported free-standing graphene-PPy materials, these flexible free-standing CRG-PPy hybrid paper presented higher areal capacitance and better rate performance.

5.2 Experimental Specific to This Chapter

5.2.1 Preparation of CRG-PPy paper

Paper-like graphene gel was formed via vacuum filtration of CRG solution. This CRG wet gel was peeled off and immersed in water for 6h to remove the impurities. Prior to PPy electropolymerization, CRG gel was immersed in an aqueous solution of 0.1 M pyrrole and 0.1M sodium *p*-toluenesulfonate (pTS) overnight at 4 °C. Subsequently, pyrrole was electropolymerized galvanostatically onto the CRG gel directly at a current density of 1 mA cm⁻² for 20, 40 or 60 min. The obtained CRG-PPy hybrid papers was rinsed with deionized water for several times and then soaked in water overnight to remove the excess monomer or dopant before drying in air.

5.2.2 Assembly of device and characterization

CRG or CRG-PPy paper were assembled into a Swagelok[®]-type two electrode testing cell (X2 Labwares Pte Ltd.) to construct a symmetric supercapacitor device. The electrolyte was 1 M H₂SO₄. Cyclic voltammetry of the cells was tested using a CHI 650D (CH Instruments, Inc.) and scanned over a range of 0.0 to 1.0 V. Galvanostatic charge/discharge tests were performed using a BTS3000 battery test system (Neware Electronic Co.) over a potential range of 0.001-1.0 V. Electrochemical impedance spectroscopy (EIS) measurements were performed using a Gamry EIS 3000 system, and the frequency range used spanned from 100 kHz to 0.01 Hz with an amplitude of 10 mV at open circuit potential.

5.3 Results and Discussion

5.3.1 Preparation of CRG-PPy paper

The fabrication procedure of CRG-PPy paper is shown in Figure 5.1a. With the assistance of vacuum filtration, the self-gelation of CRG occurred due to the intersheet π - π attractions, forming a lamellar structured graphene wet gel [17]. This gel was then soaked into pyrrole solution overnight to allow the monomer and dopant to infiltrate into the gel before performing the electropolymerization. The polymerization of PPy occurred both on the surface and throughout the gel interior, creating a layered graphene-PPy hybrid structure. The CRG-PPy hybrid papers were named as CRG-PPy20, CRG-PPy40 and CRG-PPy60 according to the deposition time of 20, 40 or 60 min. Their areal masses were 1.80, 2.36 and 2.70 mg cm⁻², respectively; whereas it was 1.13 mg cm⁻² for the control sample, CRG paper. Longer deposition time was not necessary since PPy growth tended to saturate after 60 min. The obtained CRG-PPy was flexible, as demonstrated in Figure 5.1b. It can be directly used as binder-free electrode.

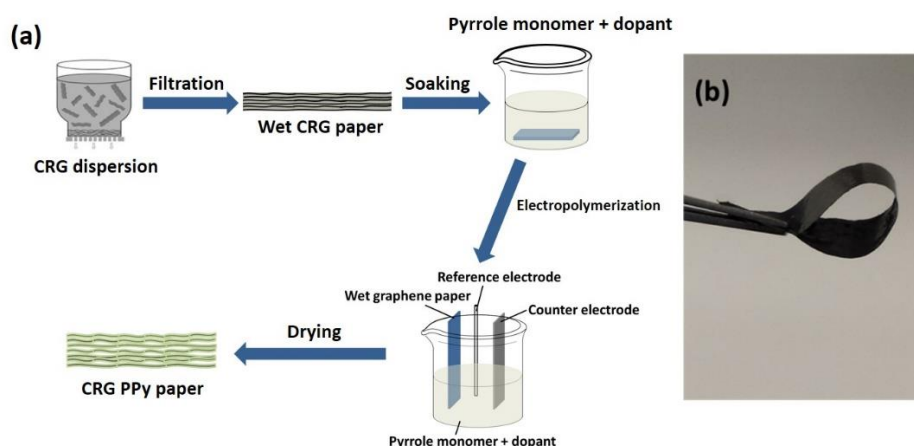


Figure 5.1 Schematic procedure to fabricate a CRG-PPy paper that includes the following steps (a): formation of wet CRG paper via filtration, soaking the wet paper in

pyrrole monomer solution, PPy electropolymerization and drying. Digital image of a CRG-PPy40 paper (b)

5.3.2 Physicochemical characterization of CRG-PPy paper

The cross-sectional view of CRG paper and CRG-PPy hybrid papers are shown in Figure 5.2a-c. CRG paper presents a typical compact layered structure with a thickness of $\sim 3.7 \mu\text{m}$, due to the strong π - π interaction between graphene sheets (Figure 5.2a). CRG-PPy paper displays an expanded layered structure with an increased thickness of over $10 \mu\text{m}$ (Figure 5.2b, c, d). PPy acts as spacer between CRG sheets, leading to the enlarged thickness in the range of 12 to $15 \mu\text{m}$. After 60 min deposition, the thickness was enlarged by ~ 3 times. Since all the CRG-PPy papers display similar structure, only the SEM image of CRG-PPy40 at higher magnification is shown (Figure 5.2f, h). It clearly shows a lamellar structure with nodule-like PPy coated onto graphene layers (Figure 5.2f). CRG-PPy paper displays a surface morphology with more wrinkles, lumps or islands (Figure 5.2h) compared to a smoother surface for CRG paper (Figure 5.2g).

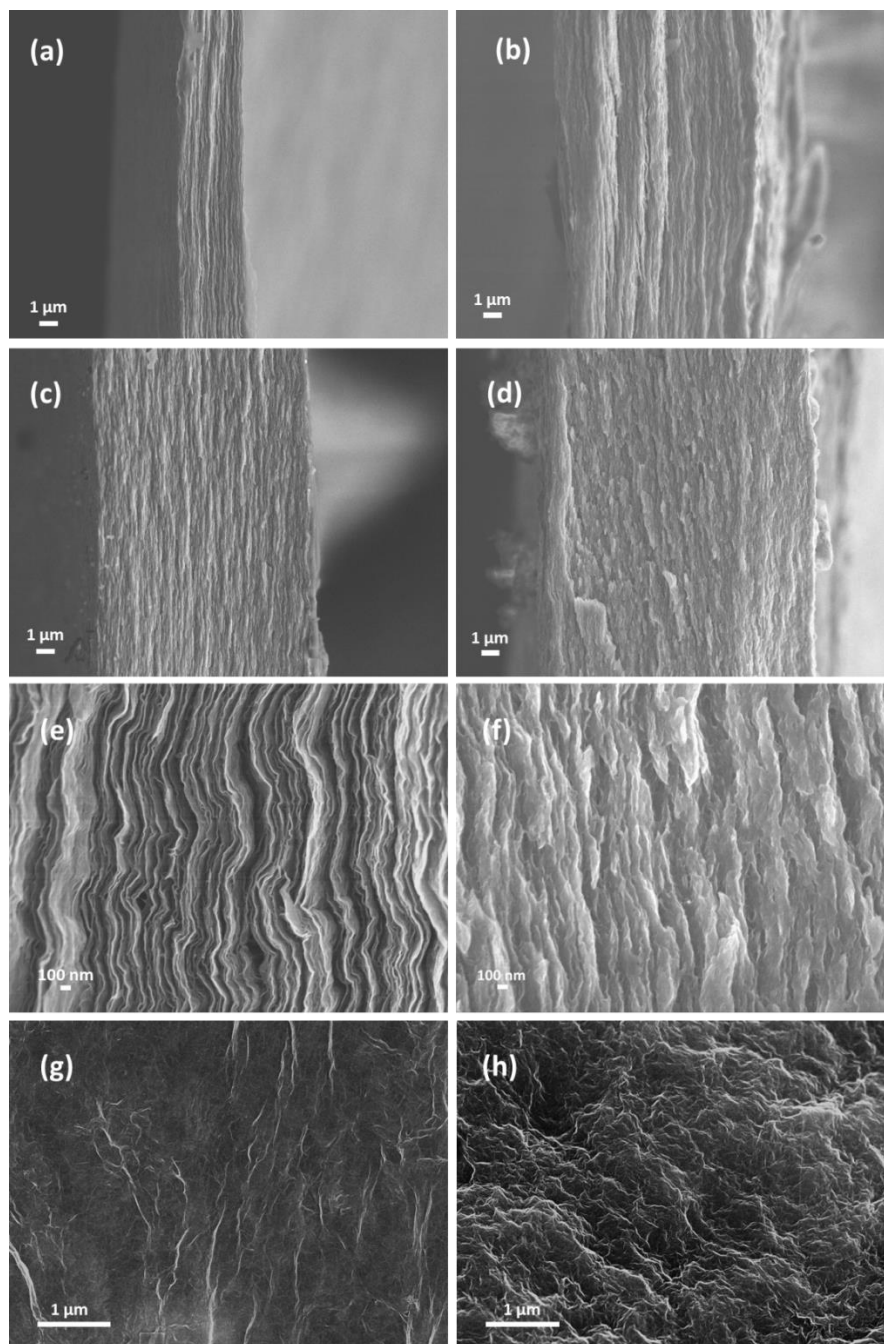


Figure 5.2 SEM images of the cross-section of a neat CRG (a), CRG-PPy20 (b), CRG-PPy40 (c) and CRG-PPy60 paper (d); Surface morphology and cross-sectional view of a neat CRG (e, g) and CRG-PPy40 paper (f, h) at higher magnification.

The elemental analysis of the CRG-PPy40 paper surface was detected by the EDX module associated with the SEM as shown in Figure 5.3. Only carbon and oxygen elements can be detected on the surface of neat CRG paper (Figure 5.3a, b). The

existence of sulphur and nitrogen (originating from PPy/pTS) apart from elements of C and O proves the existence of PPy on the hybrid paper surface (Figure 5.3c, d). The distribution of sulphur element in the cross-section of neat CRG or CRG-PPy40 paper was also compared. Very weak sulphur element signal was detected for neat CRG paper, and it was distributed discretely even at the background area (Figure 5.3f). Thus the existence of S can be excluded. In contrast, CRG-PPy40 paper displays a clear image of sulphur element distribution, clear evidence of the existence of S (Figure 5.3h). These results clearly prove that PPy was successfully grown not only on the surface but also onto the interior graphene layers of the CRG paper. A clear image of nitrogen mapping for CRG-PPy40 could not be obtained, which may be due to the weak signal of N and the signal disturbance due to the uneven cross-section.

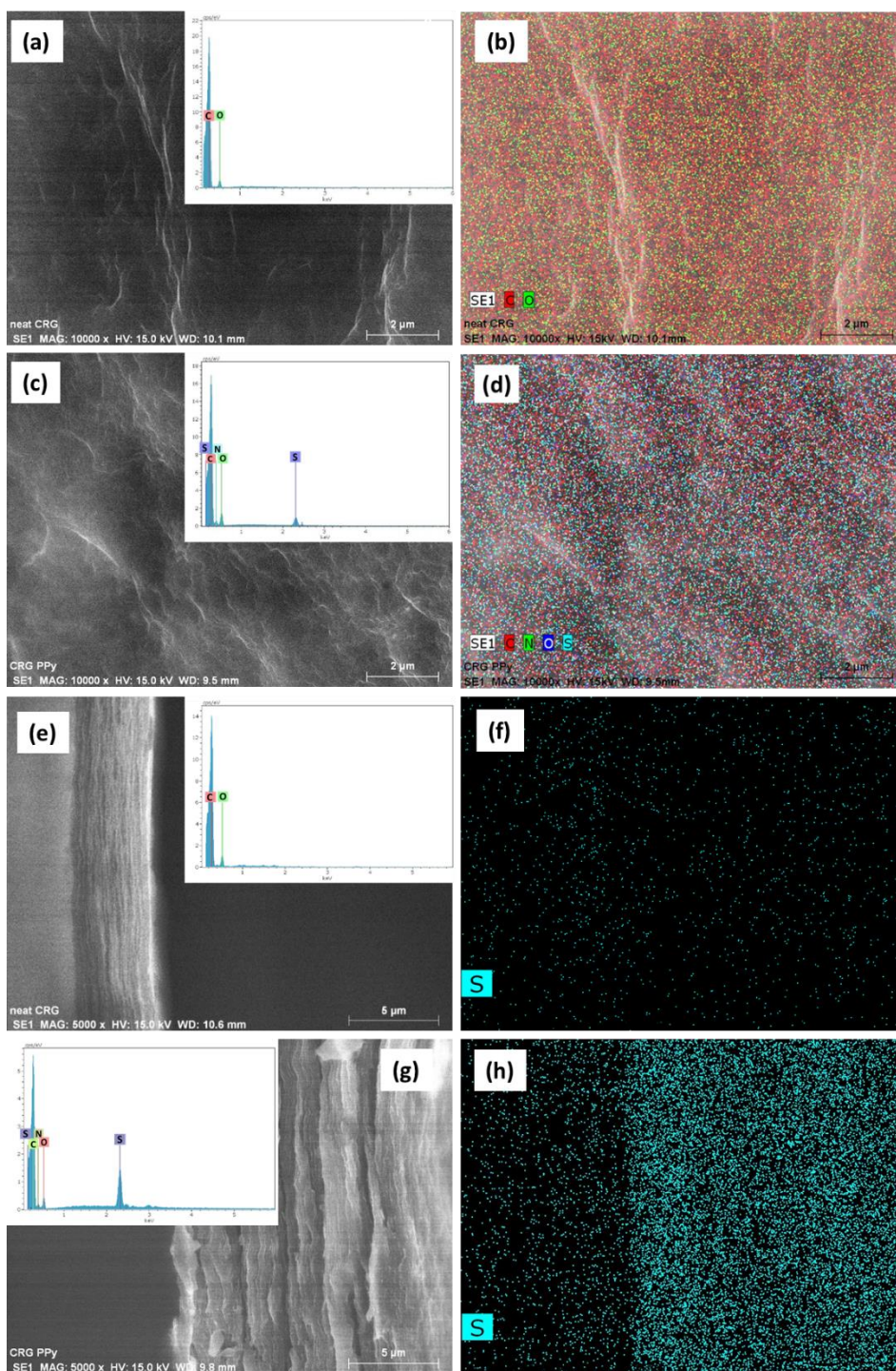


Figure 5.3 Elemental analysis of a neat CRG (a, surface; e, cross-section) and CRG-PPy40 paper (c, surface; g, cross-section). Elemental mapping of the surface of neat CRG (b), CRG-PPy40 (d), and the cross-section of CRG (f) and CRG-PPy40 (h).

The successful deposition of PPy can also be confirmed by Raman spectra (Figure 5.4a). There are only two peaks in the range of 1000-2000 cm^{-1} for neat CRG paper. The peak at around 1333 cm^{-1} (D band) is related to the defects and disorder structure in graphene. The peak at 1593 cm^{-1} (G band) is ascribed to the doubly degenerate zone centre E_{2g} mode [18, 19]. Three new peaks can be observed for CRG-PPy paper. The peaks at 928 cm^{-1} and 971 cm^{-1} can be assigned to C-H out of plane deformation and PPy ring deformation, respectively. The tiny peak at 1047 cm^{-1} represents C-H in plane deformation. PPy has characteristic peaks at 1335 cm^{-1} , 1372 cm^{-1} and 1590 cm^{-1} , which reflect the ring stretching and C=C backbone stretching [20]. Similar to the previously reported graphene/PPy composite materials, they are overlapped with the D-band and G-band of graphene [21]. CRG-PPy20 and CRG-PPy60 have similar Raman spectra as CRG-PPy40 paper, and so they are not shown here.

X-ray photoelectron spectroscopy was performed to further investigate the structure of CRG-PPy paper. Figure 5.4c, d show the deconvoluted C_{1s} spectra of neat CRG and CRG-PPy 40 respectively. The C_{1s} of neat CRG (Figure 5.4c) could fit into four component peaks, corresponding to different chemical states of carbon. The dominant peak appears at 284.7 eV. It is attributed to the collective effect of sp^2 and sp^3 hybridized carbon [22]. Peaks at 287.9 eV and 291.0 eV are assigned to oxygen bounded carbon species, C=O and O-C=O [23]. The peak at around 286 eV in CRG-PPy C_{1s} (Figure 5.4d) corresponds to C-N, C-S and C-O contributions [22]. The relative intensity of the peak at 286 eV for CRG-PPy increased remarkably compared to that for neat CRG. It may be ascribed to the C-N backbone bonding in PPy. The N_{1s} core level spectra of CRG-PPy (Figure 5.4e) is dominated by a main peak at 399.6 eV, which can be assigned to the quinoid imine (=N-) in PPy. The peaks at a higher binding energy of

401.1 eV can be ascribed to the positively charged protonated nitrogen species [22, 24]. In addition, the S_{2p} peak arises at 168 eV, which corresponds to the sulfonated group in dopant pTS (Figure 5.4f) [22].

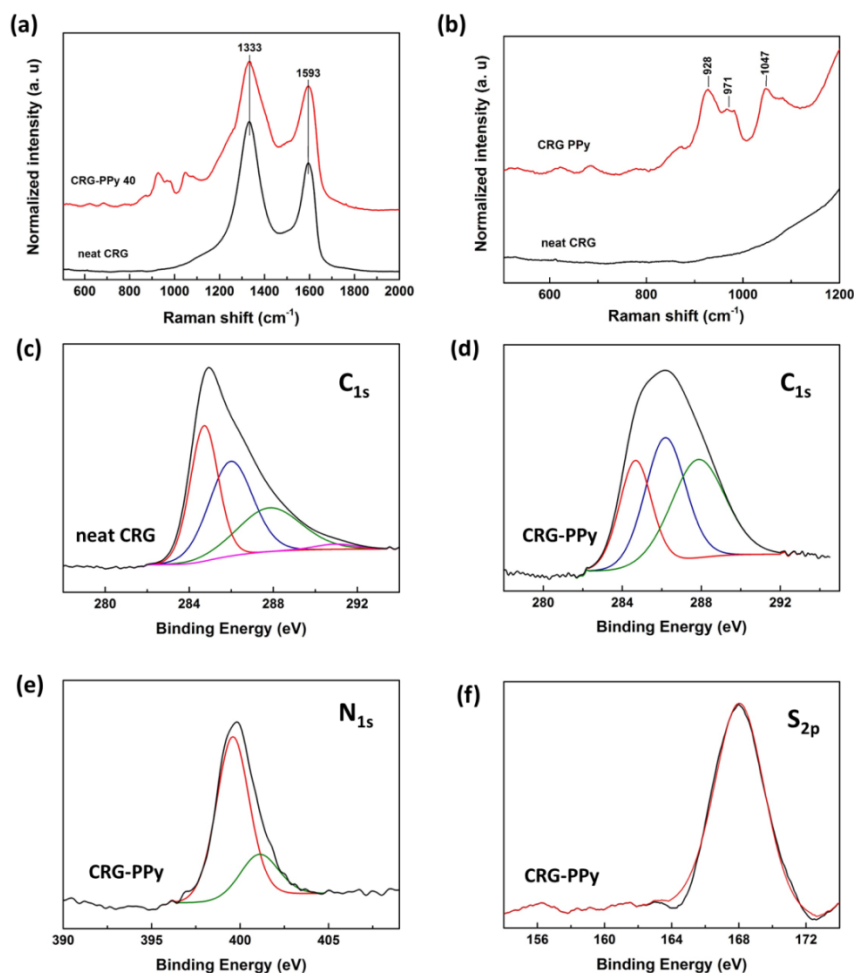


Figure 5.4 Raman spectra of a neat CRG or CRG-PPy40 paper (a) and the expanded view over 500~1200 cm^{-1} (b); XPS spectra of C_{1s} in neat CRG (c), C_{1s} in CRG-PPy (d), N_{1s} in CRG-PPy40 (e) and S_{2p} in CRG-PPy (f). (black line, experimental data; colour line: fitting line)

5.3.3 Electrochemical performance for supercapacitor

To study the pseudocapacitive performance of PPy in the composite paper, the cyclic voltammetry (CV) of CRG and CRG-PPy60 paper electrode in a three electrode

system was studied (Figure 5.5). The CRG paper displayed a nearly rectangular CV shape over the potential range of $-0.5 \sim 0.5$ V (vs. Ag/AgCl) (Figure 5.5a), indicating a nearly ideal electric double-layer capacitive behaviour. In contrast, the CRG-PPy60 paper electrode presented features of a pseudocapacitive activity, with redox peaks observed at around -0.2 V and 0.2 V (Figure 5.5b) [25].

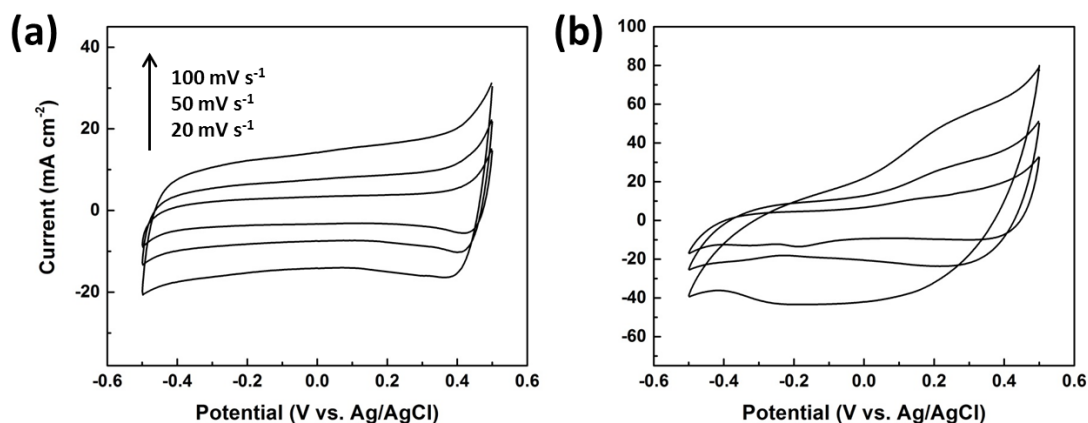


Figure 5.5 Cyclic voltammograms of a CRG (a), or CRG-PPy60 (b) paper in 1 M H₂SO₄ between -0.5 to 0.5 V (vs. Ag/AgCl) at scan rates of 20, 50, 100 mV s⁻¹.

The CRG-PPy paper based symmetric supercapacitor did not show the remarkable redox peaks from PPy in the CV curves (Figure 5.6). This is typical of a two-electrode cell system, since one electrode was oxidized while its symmetric electrode was reduced, resulting in negligible redox peaks [8, 26]. Over the scan rate range from 20 to 100 mV s⁻¹, all the CRG-PPy papers display nearly rectangular CV curves even for that with a high areal mass loading of 2.7 mg cm⁻². All these reveal their ideal capacitive behaviour. This result is in sharp contrast to that of MnO₂-graphene paper electrode with similar areal mass loading but presented a highly distorted CV curve at the same scan rate [27, 28]. The areal capacitance at 20 mV s⁻¹ was 298, 349 and 410 mF cm⁻² for CRG-PPy20, CRG-PPy40 and CRG-PPy60, respectively. CRG-

PPy60 paper delivers the highest current response, which is over 2 times that of neat CRG paper (174 mF cm^{-2} at 20 mV s^{-1}). Our CRG-PPy papers offer much higher areal capacitances than those of the previously reported graphene-PPy film/membrane electrodes, which delivered capacitances of $151\sim 175 \text{ mF cm}^{-2}$ at a low scan rate of 10 mV s^{-1} [15, 16, 29].

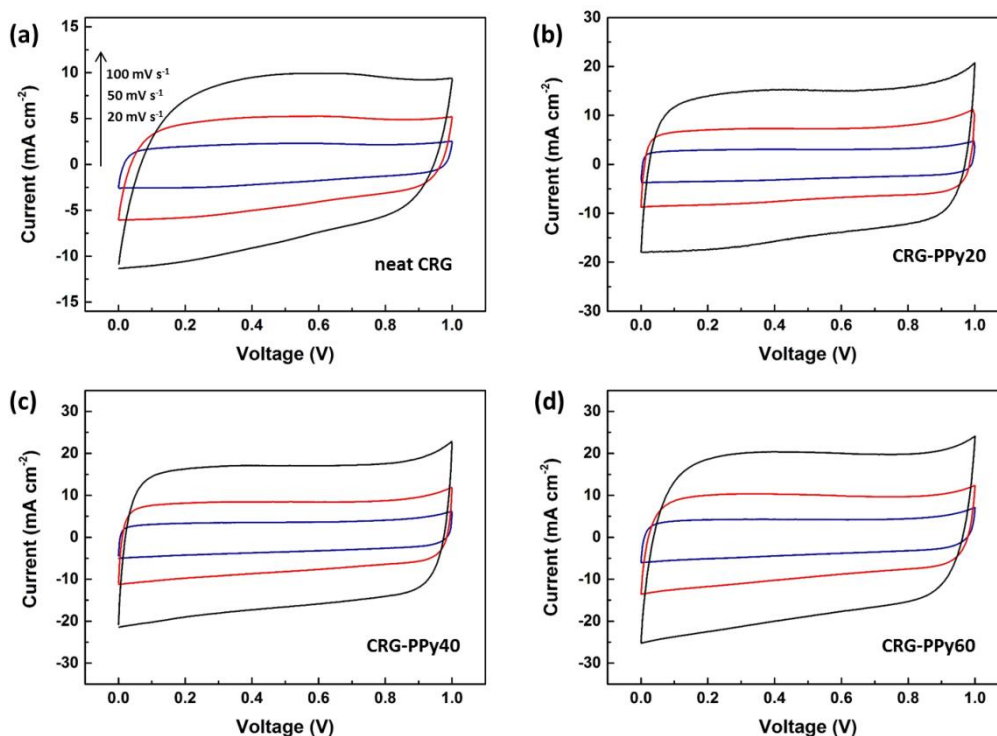


Figure 5.6 Cyclic voltammograms of a CRG (a), CRG-PPy20 (b), CRG-PPy40 (c) or CRG-PPy60 (d) paper in $1 \text{ M H}_2\text{SO}_4$ at a scan rate $20, 50, 100 \text{ mV s}^{-1}$.

Charge/discharge tests were performed and the results are shown in Figure 5.7. Neat CRG delivered a gravimetric capacitance of 164 F g^{-1} at 0.5 A g^{-1} . It slightly decreased to 156 F g^{-1} at 2 A g^{-1} . CRG-PPy20 paper shows the highest gravimetric capacitance among these hybrid papers, 190 F g^{-1} at 0.5 A g^{-1} and 165 F g^{-1} at 2 A g^{-1} . CRG-PPy 40 and CRG-PPy 60 paper deliver slightly decreased gravimetric capacitances of 163 F g^{-1} and 161 F g^{-1} respectively at 0.5 A g^{-1} , but are still comparable

to the CRG papers in this work and the previously reported ones [3, 4, 11]. Benefiting from the unique layered structure, CRG-PPy paper with 3 times thickness and much higher mass loading still maintains a similar gravimetric capacitance compared with neat CRG paper.

The areal capacitance of neat CRG and CRG-PPy hybrid papers can be calculated from their gravimetric capacitance and areal mass. The areal capacitance of CRG-PPy hybrid paper increases with prolonged electrodeposition time. The CRG-PPy60 paper gave the highest areal capacitance of 440 mF cm^{-2} at 0.5 A g^{-1} , which is 2.4 times higher than that 185 mF cm^{-2} of CRG paper. The results are 380, 342 mF cm^{-2} for CRG-PPy40 and CRG-PPy20 paper, respectively. It should be pointed out that the current of 0.5 A g^{-1} applied was equal to that of 1.35, 1.18, 0.9, 0.57 mA cm^{-2} in terms of an areal unit for CRG-PPy60, CRG-PPy40, CRG-PPy20 and CRG paper, respectively. The areal capacitance delivered from our CRG-PPy paper is higher than that for flexible graphene/PPy fibre electrode (107 mF cm^{-2} at 0.24 mA cm^{-2}) [30] and carbon fibre/PPy paper electrode (198.5 mF cm^{-2} at 1 mA cm^{-2}) [31]. At a high current density of 6 A g^{-1} ($\sim 16 \text{ mA cm}^{-2}$), over 300 mF cm^{-2} was retained for CRG-PPy60 paper, 81 % of the capacitance obtained at 0.5 A g^{-1} (Figure 5.7e). Our CRG-PPy papers present better rate capability compared with the carbon fibre/PPy paper electrode, which demonstrated a capacity retention of only 66% when the current rate increased from 1 to 10 mA cm^{-2} . [31] The unique PPy coated graphene layered structure also ensured excellent rate performance of CRG-PPy hybrid paper.

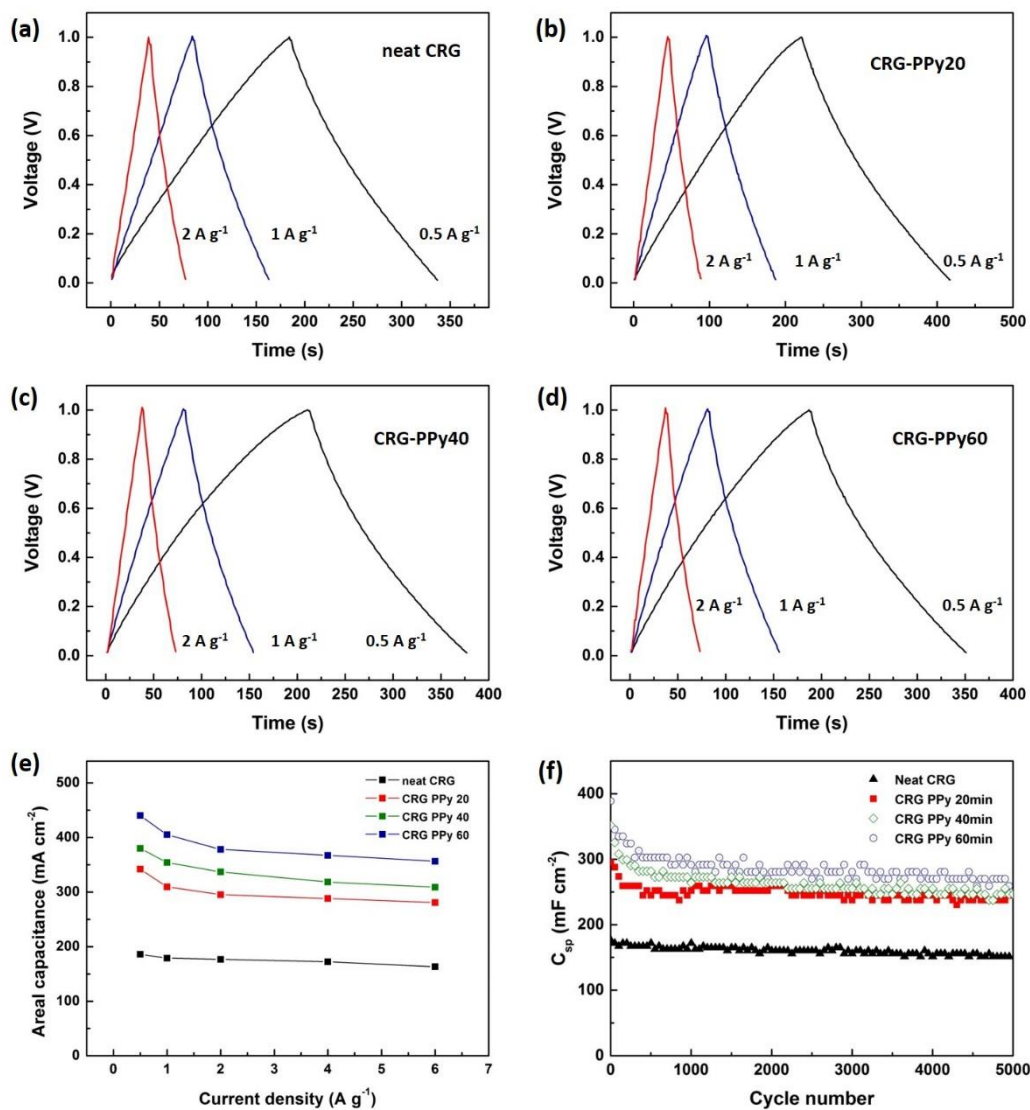


Figure 5.7 Electrochemical performance of the symmetric supercapacitors using CRG, CRG-PPy 20, CRG-PPy40 or CRG-PPy60 paper electrodes in 1M H₂SO₄. (a-d) Charge/discharge curves; (e) Areal capacitance versus current densities; (f) Cycle stability at a current density of 2 A g⁻¹.

The cycle stability of CRG-PPy hybrid papers and neat CRG paper were tested at a current density of 2 A g⁻¹ (Figure 5.7f). A capacitance retention of 75%, 78%, 85% and 92% was shown during the first 1000 cycles for CRG-PPy60, CRG-PPy40, CRG-PPy20 and CRG, respectively. A lower retention rate with the increased PPy ratio may

be attributed to the decreased pseudocapacitance contribution from PPy. PPy suffers from physical changes associated with the doping/de-doping of ions during cycling [32, 33]. The repeated redox cycles can damage the PPy molecular structure and promote PPy degradation, leading to capacitance decay. It should be pointed out that these CRG-PPy hybrid papers can still retain 71-80 % of the initial capacitance after 5000 cycles, comparable to or higher than that 56~87% retention of the previously reported results for PPy or carbon-PPy based electrodes [34-37].

The areal energy density and power density of neat CRG and CRG-PPy papers in the Ragone plot (Figure 5.8) are calculated using the following equations: $E = C_s \Delta V^2 / 7200$, $P = 3600E/t$. CRG-PPy60 paper presents a maximum energy density of $61.3 \mu\text{Wh cm}^{-2}$ at a power density of 1.2 mW cm^{-2} , while it maintains $49.5 \mu\text{Wh cm}^{-2}$ at 14.2 mW cm^{-2} . Our CRG-PPy paper displayed higher energy density compared to the reported results for graphene paper, graphene-PPy film, graphene-PANI paper [7, 16, 38], or even graphene-MnO₂ electrode [27]; especially at high power density.

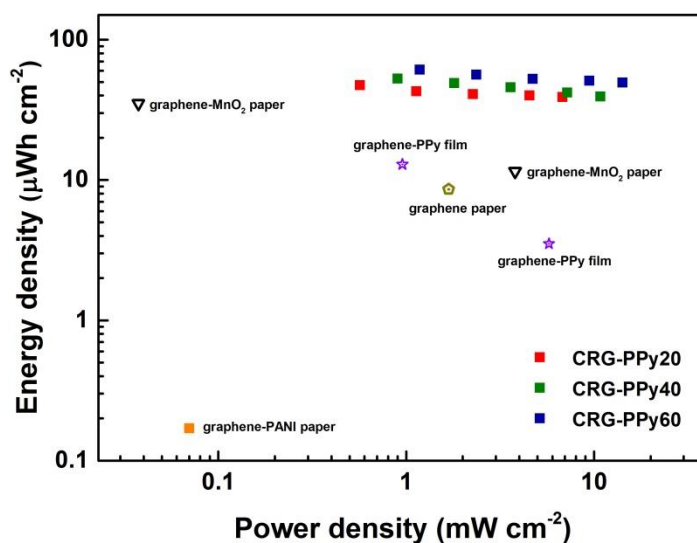


Figure 5.8 Ragone plot of CRG-PPy hybrid papers in comparison with the reported graphene-based paper materials.

The Nyquist plots of neat CRG or CRG-PPy paper electrode were obtained in the frequency range between 0.01 and 100 kHz, and are shown in Figure 5.9a. An equivalent circuit model is used to fit the impedance spectra (Figure 5.9a inset). The equivalent series resistance (ESR) includes the solution resistance R_s , electrode-electrolyte interfacial double layer resistance R_{dl} and charge transfer resistance R_{ct} [32, 39]. The semi-circle portion in the high frequency region represents two constant phase elements CPE_{dl} and CPE_f , accounting for the imperfect double layer capacitance and the faradic pseudocapacitance. The ESR of our CRG-PPy papers was around 3.5~5.5 Ω , close to that 2.2 Ω for CRG paper. At the low frequency region, a more vertical plot at low frequency region indicates more ideal capacitive performance [40]. All the CRG and CRG-PPy papers show nearly vertical lines in that region, indicating their good capacitive performances. CRG paper gives the most vertical plot among these papers, which can be ascribed to its faster ion and electron transportation due to having the

lowest thickness. The relative ion-transport rate within the electrode can be characterized by the relaxation time constant τ_0 , time taken to reach half of the saturated capacitance. The time constant can be calculated using equation $\tau_0 = 1/f_p$, f_p is the frequency at which the imaginary part of the capacitance reaches its peak value (Figure 5.9b) [41, 42]. The τ_0 of CRG-PPy papers is around 1.31 to 1.57 s, higher than that of neat CRG paper (0.63 s), which is due to their much larger thickness. Nevertheless, these CRG-PPy paper based devices offer lower time constant compared with the previously reported graphene paper based supercapacitors with a time constant in the range of 0.92 to 2.27 s [43].

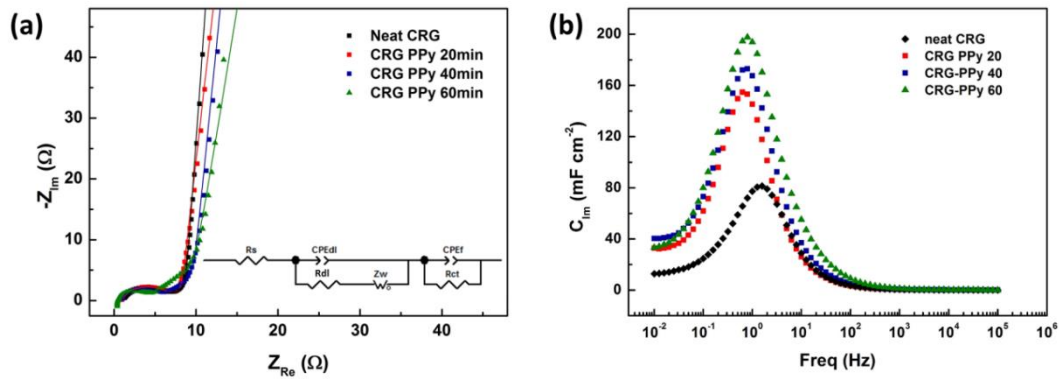


Figure 5.9 Nyquist plots (a) (scatter: experimental plots, line: fitting plots), and frequency response (b) of neat CRG or CRG-PPy papers based supercapacitor. (a inset: equivalent circuit model)

5.4 Conclusion

Wet graphene gel was used to prepare free standing graphene/PPy hybrid paper via electropolymerization. PPy was uniformly coated onto the surface and interior of the graphene gel, creating a layered graphene/PPy structure with an increased thickness.

The areal mass loading of the hybrid paper can be easily controlled by adjusting the deposition time. Benefiting from this unique structure, these hybrid papers with enlarged thickness showed a gravimetric capacitance comparable to graphene paper but with much higher areal capacitance. This hybrid paper also exhibited excellent rate performance. The high areal-normalized power density and relatively high energy density make such flexible hybrid paper promising materials for application in flexible energy storage devices.

5.5 References

- [1] M. Winter, R.J. Brodd, What Are Batteries, Fuel Cells, and Supercapacitors?, *Chemical Reviews*, 104 (2004) 4245-4270.
- [2] R. Kotz, M. Carlen, Principles and Applications of Electrochemical Capacitors, *Electrochimica Acta*, 45 (2000) 2483-2498.
- [3] M.F. El-Kady, V. Strong, S. Dubin, R.B. Kaner, Laser Scribing of High-Performance and Flexible Graphene-Based Electrochemical Capacitors, *Science*, 335 (2012) 1326-1330.
- [4] X. Yang, C. Cheng, Y. Wang, L. Qiu, D. Li, Liquid-Mediated Dense Integration of Graphene Materials for Compact Capacitive Energy Storage, *Science*, 341 (2013) 534-537.
- [5] K. Shu, C. Wang, S. Li, C. Zhao, Y. Yang, H. Liu, G. Wallace, Flexible Free-standing Graphene Paper with Interconnected Porous Structure for Energy Storage, *Journal of Materials Chemistry A*, 3 (2015) 4428-4434.
- [6] X. Yang, J. Zhu, L. Qiu, D. Li, Bioinspired Effective Prevention of Restacking in Multilayered Graphene Films: Towards the Next Generation of High-Performance Supercapacitors, *Advanced Materials*, 23 (2011) 2833-2838.
- [7] G. Wang, X. Sun, F. Lu, H. Sun, M. Yu, W. Jiang, C. Liu, J. Lian, Flexible Pillared Graphene-Paper Electrodes for High-Performance Electrochemical Supercapacitors, *Small*, 8 (2012) 452-459.
- [8] M.D. Stoller, R.S. Ruoff, Best Practice Methods for Determining an Electrode Material's Performance for Ultracapacitors, *Energy & Environmental Science*, 3 (2010) 1294-1301.
- [9] S. Zhang, N. Pan, Supercapacitors Performance Evaluation, *Advanced Energy Materials*, (2014) 1401401(1401401-1401419).
- [10] L. Hu, W. Chen, X. Xie, N. Liu, Y. Yang, H. Wu, Y. Yao, M. Pasta, H.N. Alshareef, Y. Cui, Symmetrical MnO₂-Carbon Nanotube-Textile Nanostructures for Wearable Pseudocapacitors with High Mass Loading, *ACS Nano*, 5 (2011) 8904-8913.
- [11] F. Liu, S. Song, D. Xue, H. Zhang, Folded Structured Graphene Paper for High Performance Electrode Materials, *Advanced Materials*, 24 (2012) 1089-1094.
- [12] A. Davies, P. Audette, B. Farrow, F. Hassan, Z. Chen, J.-Y. Choi, A. Yu, Graphene-Based Flexible Supercapacitors: Pulse-Electropolymerization of Polypyrrole

on Free-Standing Graphene Films, *Journal of Physical Chemistry C*, 115 (2011) 17612-17620.

[13] H.P. de Oliveira, S.A. Sydlik, T.M. Swager, Supercapacitors from Free-Standing Polypyrrole/Graphene Nanocomposites, *The Journal of Physical Chemistry C*, 117 (2013) 10270-10276.

[14] L. Wu, W. Li, P. Li, S. Liao, S. Qiu, M. Chen, Y. Guo, Q. Li, C. Zhu, L. Liu, Powder, Paper and Foam of Few-Layer Graphene Prepared in High Yield by Electrochemical Intercalation Exfoliation of Expanded Graphite, *Small*, 10 (2014) 1421-1429.

[15] J. Zhang, P. Chen, B.H.L. Oh, M.B. Chan-Park, High Capacitive Performance of Flexible and Binder-free Graphene-polypyrrole Composite Membrane based on In situ Reduction of Graphene Oxide and Self-assembly, *Nanoscale*, 5 (2013) 9860-9866.

[16] H. Zhou, G. Han, Y. Xiao, Y. Chang, H.-J. Zhai, Facile Preparation of Polypyrrole/graphene Oxide Nanocomposites with Large Areal Capacitance Using Electrochemical Codeposition for Supercapacitors, *Journal of Power Sources*, 263 (2014) 259-267.

[17] X. Yang, L. Qiu, C. Cheng, Y. Wu, Z.-F. Ma, D. Li, Ordered Gelation of Chemically Converted Graphene for Next-Generation Electroconductive Hydrogel Films, *Angewandte Chemie International Edition*, 50 (2011) 7325-7328.

[18] A.C. Ferrari, J.C. Meyer, V. Scardaci, C. Casiraghi, M. Lazzeri, F. Mauri, S. Piscanec, D. Jiang, K.S. Novoselov, S. Roth, A.K. Geim, Raman Spectrum of Graphene and Graphene Layers, *Physical Review Letters*, 97 (2006) 187401.

[19] F. Tuinstra, J.L. Koenig, Raman Spectrum of Graphite, *The Journal of Chemical Physics*, 53 (1970) 1126-1130.

[20] Y.-C. Liu, B.-J. Hwang, W.-J. Jian, R. Santhanam, In situ Cyclic Voltammetry-surface-enhanced Raman Spectroscopy: Studies on the Doping-undoping of Polypyrrole Film, *Thin Solid Films*, 374 (2000) 85-91.

[21] Y. Yang, C.Y. Wang, B.B. Yue, S. Gambhir, C.O. Too, G.G. Wallace, Electrochemically Synthesized Polypyrrole/Graphene Composite Film for Lithium Batteries, *Advanced Energy Materials*, 2 (2012) 266-272.

[22] A. Kumar, R.K. Singh, H.K. Singh, P. Srivastava, R. Singh, Mechanism of Direct Current Electrical Charge Conduction in p-Toluenesulfonate Doped Polypyrrole/carbon Composites, *Journal of Applied Physics*, 115 (2014) 103702 (1-9).

- [23] P. Liu, Y. Huang, Synthesis of Reduced Graphene oxide-conducting polymers- Co_3O_4 Composites and Their Excellent Microwave Absorption Properties, *RSC Advances*, 3 (2013) 19033-19039.
- [24] S. Zhang, N. Pan, Supercapacitors Performance Evaluation, *Advanced Energy Materials*, 5 (2015) 1401401 (1-19).
- [25] Y. Tian, F. Yang, W. Yang, Redox behavior and stability of polypyrrole film in sulfuric acid, *Synthetic Metals*, 156 (2006) 1052-1056.
- [26] V. Khomenko, E. Frackowiak, F. Béguin, Determination of the Specific Capacitance of Conducting Polymer/nanotubes Composite Electrodes using Different Cell Configurations, *Electrochimica Acta*, 50 (2005) 2499-2506.
- [27] A. Sumboja, C.Y. Foo, X. Wang, P.S. Lee, Large Areal Mass, Flexible and Free-Standing Reduced Graphene Oxide/Manganese Dioxide Paper for Asymmetric Supercapacitor Device, *Adv. Mater.*, 25 (2013) 2809-2815.
- [28] T. Zhai, F. Wang, M. Yu, S. Xie, C. Liang, C. Li, F. Xiao, R. Tang, Q. Wu, X. Lu, Y. Tong, 3D MnO_2 -Graphene Composites with Large Areal Capacitance for High-performance Asymmetric Supercapacitors, *Nanoscale*, 5 (2013) 6790-6796.
- [29] P.A. Mini, A. Balakrishnan, S.V. Nair, K.R.V. Subramanian, Highly Super Capacitive Electrodes Made of Graphene/poly(pyrrole), *Chemical Communications*, 47 (2011) 5753-5755.
- [30] X. Ding, Y. Zhao, C. Hu, Y. Hu, Z. Dong, N. Chen, Z. Zhang, L. Qu, Spinning Fabrication of Graphene/polypyrrole Composite Fibers for All-solid-state, Flexible Fibriform Supercapacitors, *Journal of Materials Chemistry A*, 2 (2014) 12355-12360.
- [31] C.Y. Yang, J.L. Shen, C.Y. Wang, H.J. Fei, H. Bao, G.C. Wang, All-solid-state Asymmetric Supercapacitor Based on Reduced Graphene oxide/carbon nanotube and Carbon fiber paper/polypyrrole Electrodes, *Journal of Materials Chemistry A*, 2 (2014) 1458-1464.
- [32] P. Delahay, G.G. Susbielles, Double-Layer Impedance of Electrodes with Charge-Transfer Reaction, *The Journal of Physical Chemistry*, 70 (1966) 3150-3157.
- [33] J. Wang, Y. Xu, J. Wang, J. Zhu, Y. Bai, L. Xiong, Study on Capacitance Evolving Mechanism of Polypyrrole during Prolonged Cycling, *The Journal of Physical Chemistry B*, 118 (2014) 1353-1362.

- [34] M. Beidaghi, C. Wang, Micro-supercapacitors Based on Three Dimensional Interdigital Polypyrrole/C-MEMS Electrodes, *Electrochimica Acta*, 56 (2011) 9508-9514.
- [35] C. Zhao, C. Wang, R. Gorkin Iii, S. Beirne, K. Shu, G.G. Wallace, Three Dimensional (3D) Printed Electrodes for Interdigitated Supercapacitors, *Electrochemistry Communications*, 41 (2014) 20-23.
- [36] F. Zhang, F. Xiao, Z.H. Dong, W. Shi, Synthesis of Polypyrrole Wrapped Graphene Hydrogels Composites as Supercapacitor Electrodes, *Electrochimica Acta*, 114 (2013) 125-132.
- [37] X. Lu, H. Dou, C. Yuan, S. Yang, L. Hao, F. Zhang, L. Shen, L. Zhang, X. Zhang, Polypyrrole/carbon nanotube Nanocomposite Enhanced the Electrochemical Capacitance of Flexible Graphene Film for Supercapacitors, *Journal of Power Sources*, 197 (2012) 319-324.
- [38] H. Wei, J. Zhu, S. Wu, S. Wei, Z. Guo, Electrochromic Polyaniline/graphite Oxide Nanocomposites with Endured Electrochemical Energy Storage, *Polymer*, 54 (2013) 1820-1831.
- [39] H. Fu, Z.-j. Du, W. Zou, H.-q. Li, C. Zhang, Carbon nanotube Reinforced Polypyrrole Nanowire Network as a High-performance Supercapacitor Electrode, *Journal of Materials Chemistry A*, 1 (2013) 14943-14950.
- [40] R. Kötz, M. Hahn, R. Gally, Temperature Behavior and Impedance Fundamentals of Supercapacitors, *Journal of Power Sources*, 154 (2006) 550-555.
- [41] P.L. Taberna, P. Simon, J.F. Fauvarque, Electrochemical Characteristics and Impedance Spectroscopy Studies of Carbon-carbon Supercapacitors, *Journal of the Electrochemical Society*, 150 (2003) A292-A300.
- [42] H. Kurig, A. Jaenes, E. Lust, Electrochemical Characteristics of Carbide-Derived Carbon vertical bar 1-Ethyl-3-methylimidazolium Tetrafluoroborate Supercapacitor Cells, *Journal of the Electrochemical Society*, 157 (2010) A272-A279.
- [43] J. Zhu, C. Cheng, X. Yang, Y. Wang, L. Qiu, D. Li, Dynamic Electrosorption Analysis as an Effective Means to Characterise the Structure of Bulk Graphene Assemblies, *Chemistry – A European Journal*, 19 (2013) 3082-3089.

6 Fabrication of Flexible Graphene/polypyrrole Film Directly from the Exfoliated Expanded Graphite and in-situ formed polypyrrole nanofibres for Supercapacitor Application

6.1 Introduction

The two-dimensional structure with high aspect ratio makes graphene sheets to be easily assembled into freestanding films with robust mechanical properties for flexible power sources. Among various graphene synthesis routes, wet chemical exfoliation is the most realistic approach to realize mass production of graphene. Currently, the most commonly used wet chemical method is the exfoliation of strongly oxidized graphite oxide followed by reduction [1, 2]. However, this method has several drawbacks, including great number of defects induced, toxic reagents used and time-consuming preparation procedure. Hence it is desirable to develop methods to prepare less defected graphene under a mild condition. A non-oxidized graphene, directly exfoliated graphene (DEG), can be formed by direct liquid-phase exfoliation (LPE) of graphite using organic solvent or aqueous surfactant solution [3, 4].

The starting graphite source for LPE can be either natural graphite, highly oriented pyrolytic graphite (HOPG) or expanded graphite. The worm-like expanded graphite (WG) can be mass produced by thermal treatment of commercially available expandable graphite flakes. WG has already been used in many applications such as adsorbent [5, 6], phase charge material [7], catalyst support [8], and battery [9]. Compared to natural graphite and HOPG, WG is expected to facilitate the exfoliation due to the pre-expanded structures [10]. Several attempts to produce graphene via LPE using WG have already been reported. WG was successfully exfoliated in aqueous

solution using rose Bengal [11], in DMSO with stabilizer tetracyanoquinodimethane [12] and in organic co-solvent [13]. Although the surfactant-assisted LPE method to fabricate graphene has been well studied, flexible electrodes based on such types of graphene were rarely reported. The surfactant adsorbed on the graphene can be difficult to be completely removed by rinsing, resulting in increased resistance and deteriorated electrochemical performance. Also, the lack of functional groups hindered the self-assembly of DEG into robust films or scaffolds as flexible electrodes.

With the above considerations in mind, an alternative strategy (a tandem strategy) was developed which is described in this chapter. In this work, advantage was taken of the surfactant cetyltrimethylammonium bromide (CTAB) in the graphene dispersion by using it as template for nanostructured polypyrrole fibre (PPyF) growth, instead of attempting to remove it. PPyF was prepared in the presence of DEG/CTAB. PPyF has demonstrated its excellent performances in supercapacitors, lithium-ion batteries and biocompatible batteries [14-17]. The incorporation of PPyF can provide large pseudocapacitance, and also serve as a reinforcement to enhance the mechanical properties of flexible PPyF/graphene film [18]. Such approach can effectively utilize the remained surfactant, minimizing its negative effects on the electrode's electrochemical properties. The free-standing and flexible graphene/PPyF film can be obtained by filtration of the obtained DEG/CTAB/PPyF dispersion. This film demonstrated good electrochemical performances with a specific capacitance of up to 160 F g^{-1} .

6.2 Experimental Specific to This Chapter

6.2.1 Exfoliation of worm-like expanded graphite

The expandable graphite flakes (3772, Asbury Graphite Mills USA) was thermally expanded at 500 °C for 15s to obtain worm-like expanded graphite (WG). The exfoliated graphene (DEG) was prepared by direct exfoliation of WG in the presence of surfactant cetyl trimethylammonium bromide (CTAB). WG was dispersed in CTAB aqueous solution (1 mg mL⁻¹) to give a 10 mg mL⁻¹ dispersion, then ultrasonicated for 4h with 60% amplitude (Branson Digital Sonifier). The supernatant was collected after 40 min centrifugation at 4400 rpm. The sediment can be recycled and reused. The content of DEG in the dispersion was confirmed by collecting DEG on polycarbonate filter membrane, followed by rinsing with water. The absorption coefficient α of DEG was determined by the UV absorbance at 660 nm at the given concentration [4]. So the concentration of DEG solution can be easily estimated from the absorbance at 660 nm.

6.2.2 Preparation of DEG-PPyF film

The DEG/CTAB dispersion was directly used to prepare DEG-PPyF film using the adsorbed CTAB on graphene sheets as the template. Pyrrole monomer (DEG:pyrrole = 1:4, 1:8 weight ratio) and concentrated hydrochloric acid (to give a 0.2 M HCl concentration) were added into the DEG/CTAB dispersion, followed by the slow addition of oxidant ammonium persulfate (APS) (APS: Py=2:1, by weight). The reaction was kept in an ice water bath under stirring for 6h. After completion, the resultant dispersion of DEG/CTAB/PPyF was filtered to form flexible DEG-PPyF film. In this work, according to the ratio of DEG to pyrrole, DEG-PPyF films are named as

DEG-PPyF1 (1:4), DEG-PPyF2 (1:8). PPy fibre film (PPyF) without DEG and DEG film without PPyF were also prepared for comparison. The total weight of DEG plus pyrrole monomer was controlled at around 36 mg for easy comparison.

6.3 Results and Discussion

6.3.1 Exfoliation of graphite

After thermal expansion, WG can be expanded over 80 times [19]. Such expansion structure is helpful for the complete exfoliation of graphite layers [20]. WG presents a typical worm-like structure that is loose and porous, which is composed of parallel sheets with pores over several micrometres of the structure (Figure 6.1a). The pore wall thickness is around ~80 nm, indicating that it consists of multiple layers of graphene sheets (Figure 6.1b inset). Through the transmission electron detector of the SEM (TED-SEM), transparent and wrinkled DEG sheets can be seen (Figure 6.1c). The successful exfoliation of WG was further confirmed by AFM. Figure 6.1d is the AFM image of a $1.5 \times 1.5 \mu\text{m}$ surface of silicon wafer with DEG deposited. Flakes with dimensions around 300-400 nm can be observed. Zoomed images show single flakes with ~400 nm in dimension and ~4 nm in height. The apparent height of graphene derived from wet chemical method is reported to be ~1.2 nm as measured by AFM [2]. It clearly suggests that most of the DEG obtained in this work consists of ~3-4 layers.

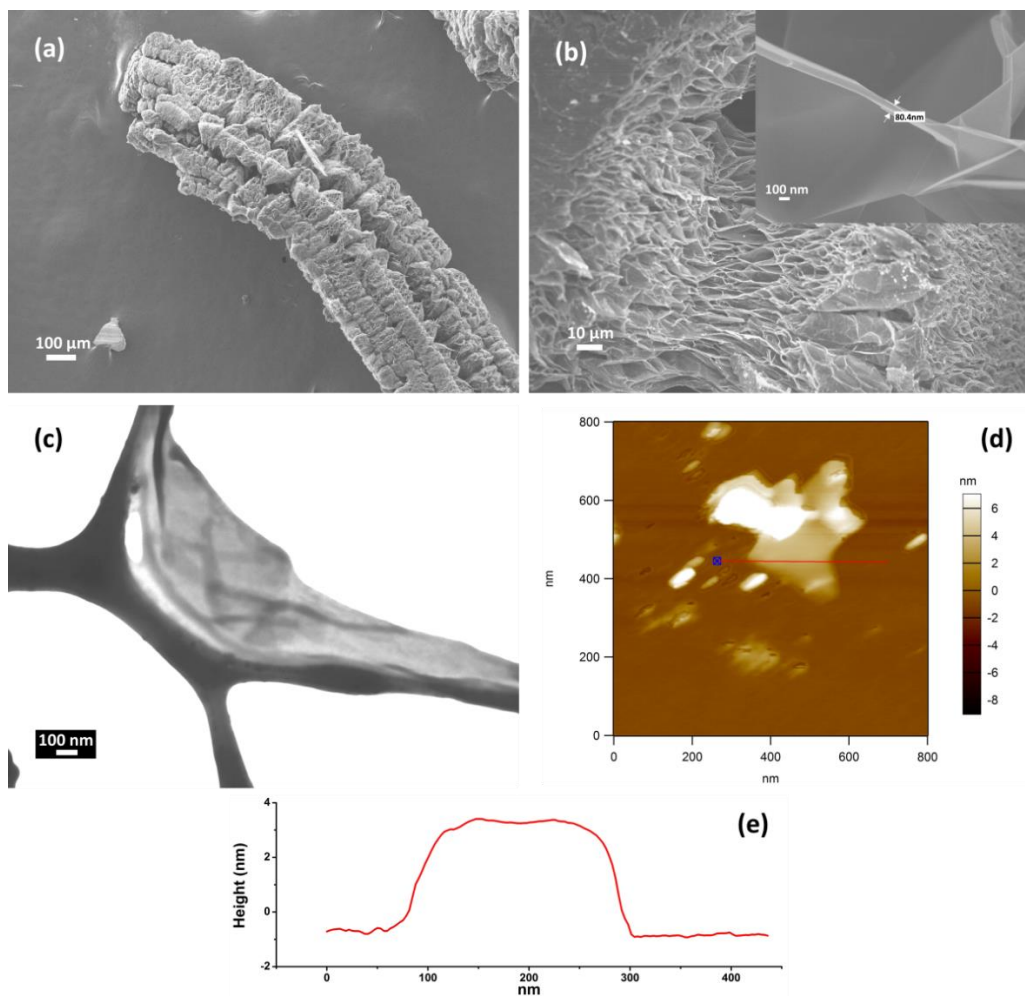


Figure 6.1 SEM images of worm-like expanded graphite (a-b), TED-SEM image of DEG (c) and AFM image (d) and height profile of DEG (e).

The Raman spectra of WG, DEG are shown in Figure 6.2. The chemically reduced graphene (CRG) paper prepared via graphite oxide exfoliation route is also shown for comparison. Its preparation method is described in the previous Chapter 2 (Experimental). G band, D band and 2D band are the three main features in the Raman spectra of graphite-related materials [21]. The G band refers to the first order scattering of E_{2g} mode. The D band is related to the first order of the zone-boundary phonons which reflects the structural defects of graphite materials. The 2D band is the second order of zone-boundary phonons, which can be used to distinguish single, double, few

and multi-layered graphene structure [22, 23]. It can be seen that WG and DEG display a prominent G band at 1581 cm^{-1} , similar to that of natural graphite powder. A tiny D band around 1333 cm^{-1} appears in WG, probably due to the structure defects caused by the intercalation and expansion process. The DEG displays a stronger D band than WG at 1333 cm^{-1} , indicating that more defects were created by the cracking of graphite sheets into small flakes during the exfoliation process. In CRG, the strong D band indicates large amounts of disorder formed during the caustic oxidation, exfoliation and reduction processes [2]. The 2D peak in WG appears at around 2700 cm^{-1} . It is clearly split into two peaks, similar to the bulk graphite, indicating its multilayered graphene structure. A broad, down-shifted 2D single peak with lower intensity was observed in the CRG spectrum. The broad and weak 2D peak in CRG is caused by the steric effects of oxygen moieties, partial amorphization and reduced sp^2 domains [24, 25]. For DEG, the 2D peak shows the characteristic feature of thin flakes composed of a few graphene layers (2~5) [4, 23, 26], similar to CTAB stabilized exfoliated graphene [27].

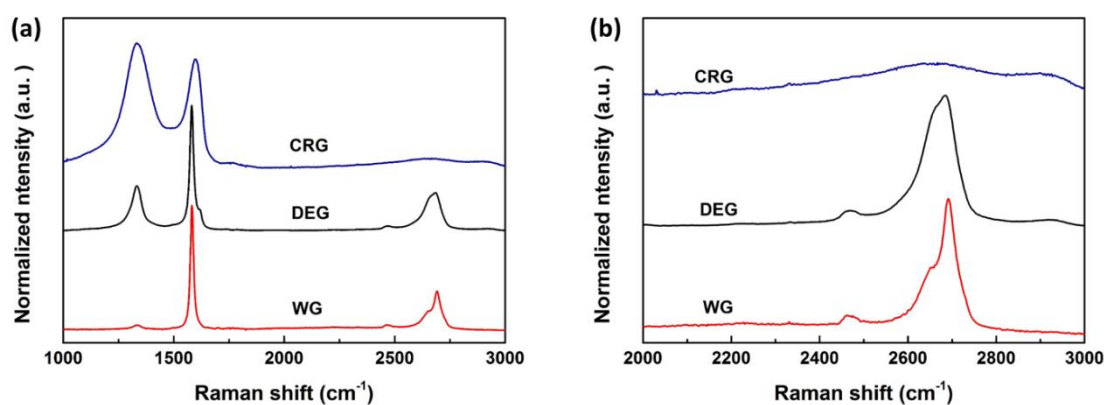


Figure 6.2 (a) Raman spectra of CCG, DEG and WG. (b) 2D peak of CCG, DEG and WG.

It is expected that DEG and WG give similar XPS spectra (Figure 6.4), for no chemical reaction occurred during the exfoliation process. After peak fitting, C1s spectrum of carbon materials generally shows three pronounced components corresponding to carbon atoms in different functional groups. The C1s of original WG shows three peaks at 285 eV, 285.9 eV and 287eV, assigned to non-oxygenated ring C (C-C), C in C-OH bonds and carbonyl C (C=O) respectively, which may be attributed to the residual oxygen containing groups after thermal expansion [28]. Those components can also be found in the C1s spectrum of DEG at 284.8 eV, 285.9 eV and 287 eV, respectively. The increased relative peak intensity at 285.9 eV in DEG may be caused by the adsorbed water/surfactant molecules during the exfoliation process [28]. A similar peak intensity increase can be found in graphene from the surfactant-assisted liquid exfoliation of expanded graphite [11]. The corresponding O1s peak confirms that oxygen atoms are bonded with carbon in two forms, C-OH at 532.5 eV and C=O at ~534 eV. The oxygen atomic ratio changed from 6% for WG to 17% for DEG, which may be caused by the adsorbed water/surfactant.

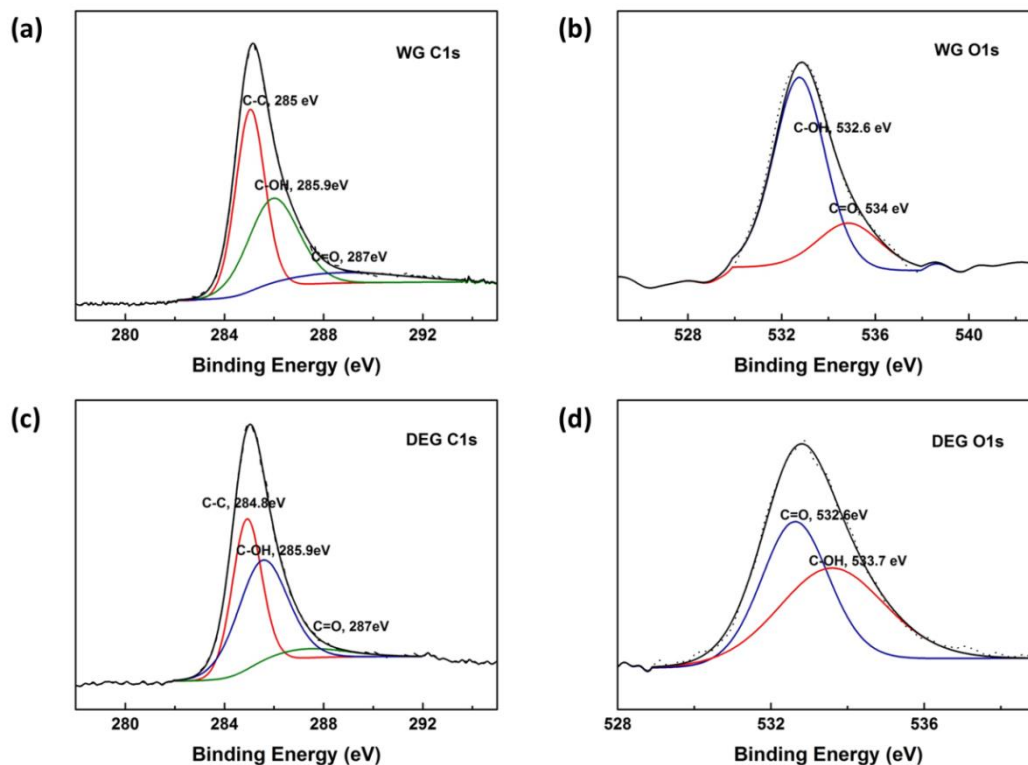


Figure 6.3 XPS spectra of WG C1s (a), WG O1s (b), DEG C1s (c), DEG O1s (d).

6.3.2 Physicochemical characterization of DEG-PPyF film

The DEG/CTAB dispersion was directly used to synthesize DEG-PPyF via an *in situ* chemical polymerization. At an appropriate concentration of monomer (10-30 mM), surfactant (2-12 cmc) and a monomer/oxidant ratio (1:2), a lamellar structure can be formed between the CTAB cations and APS anions resulting in the formation of fibre-like PPy nanostructure [29]. The PPy fibres were then interacted with DEG sheets, forming a flexible film after filtration (Figure 6.4a). It should be pointed out that the composite film at a higher DEG ratio (e.g. 1:1, 1:2) was fragile and easily crumbled into powder, thus were unsuitable as flexible electrodes (Figure 6.4b). For neat DEG, the obtained film cannot be peeled off from the filter membrane.

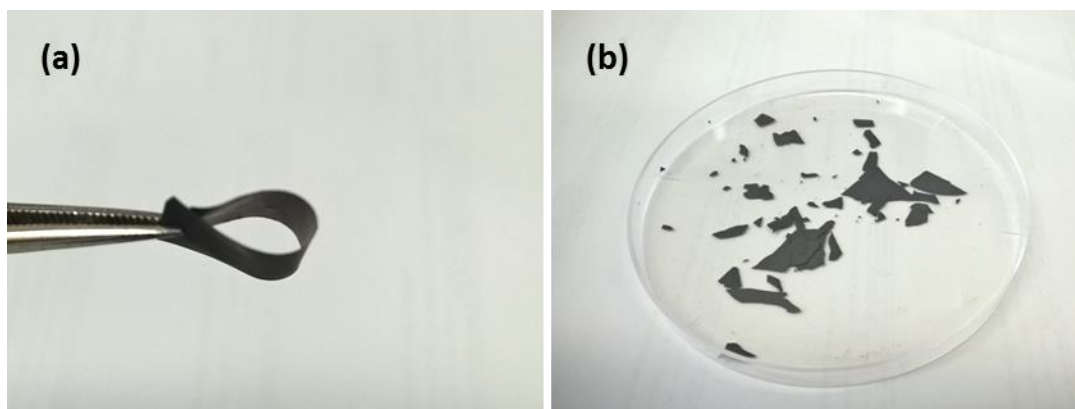


Figure 6.4 Digital image of DEG-PPyF1 flexible film (a), and film with a DEG:pyrrole ratio of 1:2 (b).

Figure 6.5 shows the SEM images of DEG-PPyF and neat PPyF films. The cross-sectional image (Figure 6.5d, g) of DEG-PPyF reveals that the film consists of entangled PPy nanofibres of several tens of nanometres in diameter (Figure 6.5a). The shape of PPyF can be seen more clearly in the surface image (Figure 6.5f, i). In DEG-PPyF film, PPyF was found to be sandwiched between nanometre-thick DEG sheets due to the interaction between PPy and graphene aromatic basal planes. Bound and entangled by PPy fibres, the DEG-PPyF composite film becomes free-standing and flexible. The $\sim 20 \mu\text{m}$ thick PPyF film exhibits a conductivity of 0.9 S cm^{-1} . An increased conductivity of 3.5 S cm^{-1} was presented by DEG-PPyF1 film with similar thickness.

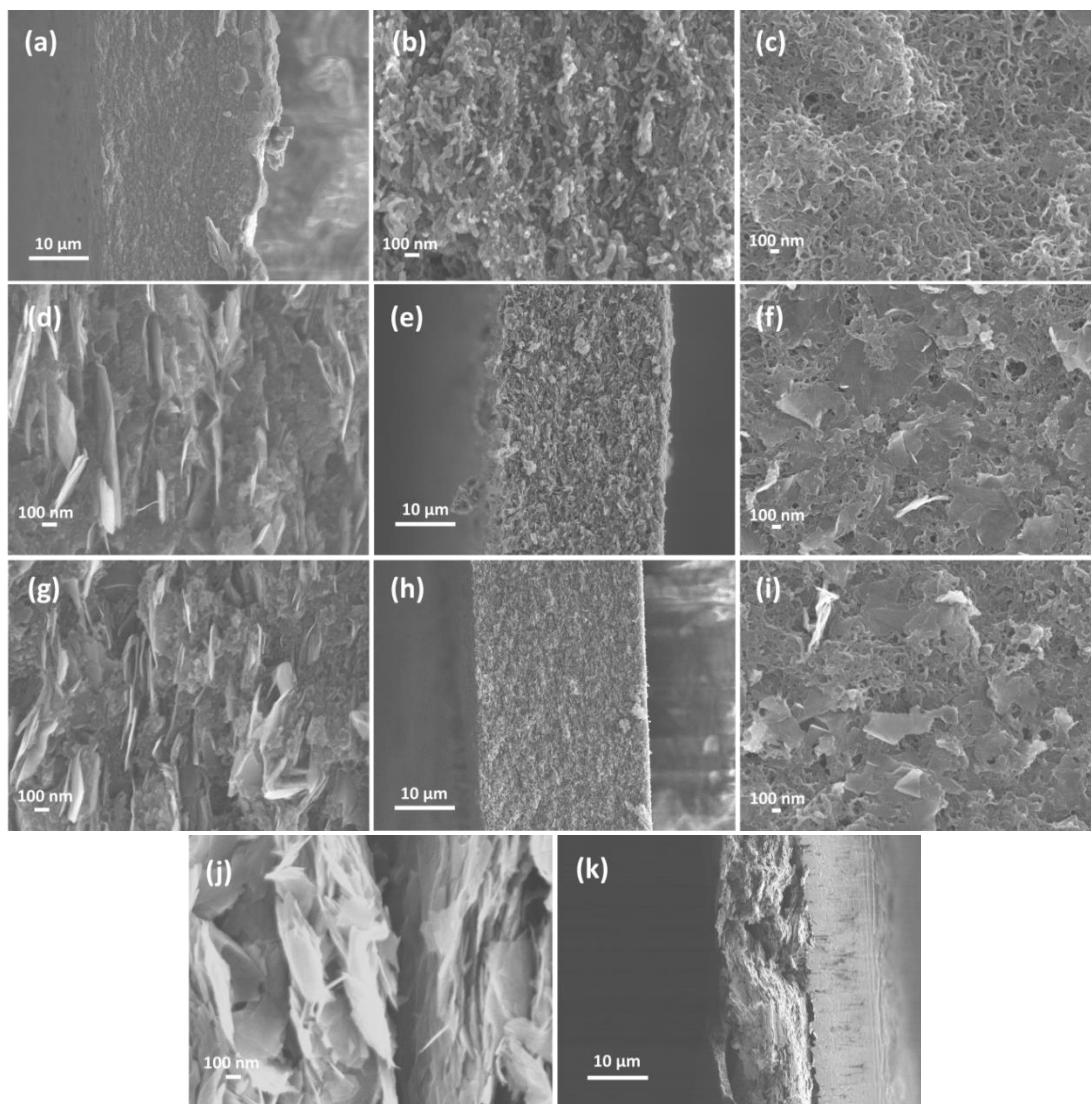


Figure 6.5 Cross-sectional view of PPyF film (a, b), DEG-PPyF1 film (d,e), DEG-PPyF2 film (g, h) and DEG film (j, k, on filter membrane); and surface morphology of PPyF film (c), DEG-PPyF1 film (f) and DEG-PPyF2 film (i)

The structural information of PPy, DEG, DEG-PPyF1 and DEG-PPyF2 films was studied by Raman spectroscopy (Figure 6.6a-e). Two characteristic peaks appear at 1345 cm^{-1} and 1539 cm^{-1} for PPyF film, which arises from the π -conjugated planar structure and ring stretching of polyrrole backbone, respectively [30]. Tiny peaks near 940 and 975 cm^{-1} can be assigned to the quinoid polaronic and bipolaronic structure

[14]. As described previously, there are three main peaks in DEG: D peak at 1333 cm^{-1} , G peak at 1581 cm^{-1} and 2D peak near 2700 cm^{-1} . In DEG-PPyF hybrid films, the evolution of these peaks was clearly observed due to the interactions between DEG and PPyF. The D band and G band were overlapped with two dominant peaks of PPyF, and became broader. The 2D peak became weaker with the decreased DEG ratio.

Figure 6.6f shows the TGA curves of DEG, PPyF and DEG-PPyF films. The weight loss of $\sim 3\%$ between $150\text{-}200^\circ\text{C}$ for DEG may be ascribed to the pyrolysis of residual oxygen-containing groups. It can hardly be observed in the DEG-PPyF films because of the relatively low DEG content. The weight loss at $200\text{-}300^\circ\text{C}$ ($\sim 10.5\%$) for PPyF containing films is caused by the decomposition of CTAB [31]. The decomposition of PPy polymer chain, starts at around 300°C [32]. The total weight loss in the whole temperature range ($0\text{-}600^\circ\text{C}$) for DEG, DEG-PPyF1, DEG-PPyF2 and PPyF is 10%, 35%, 44% and 56 % respectively.

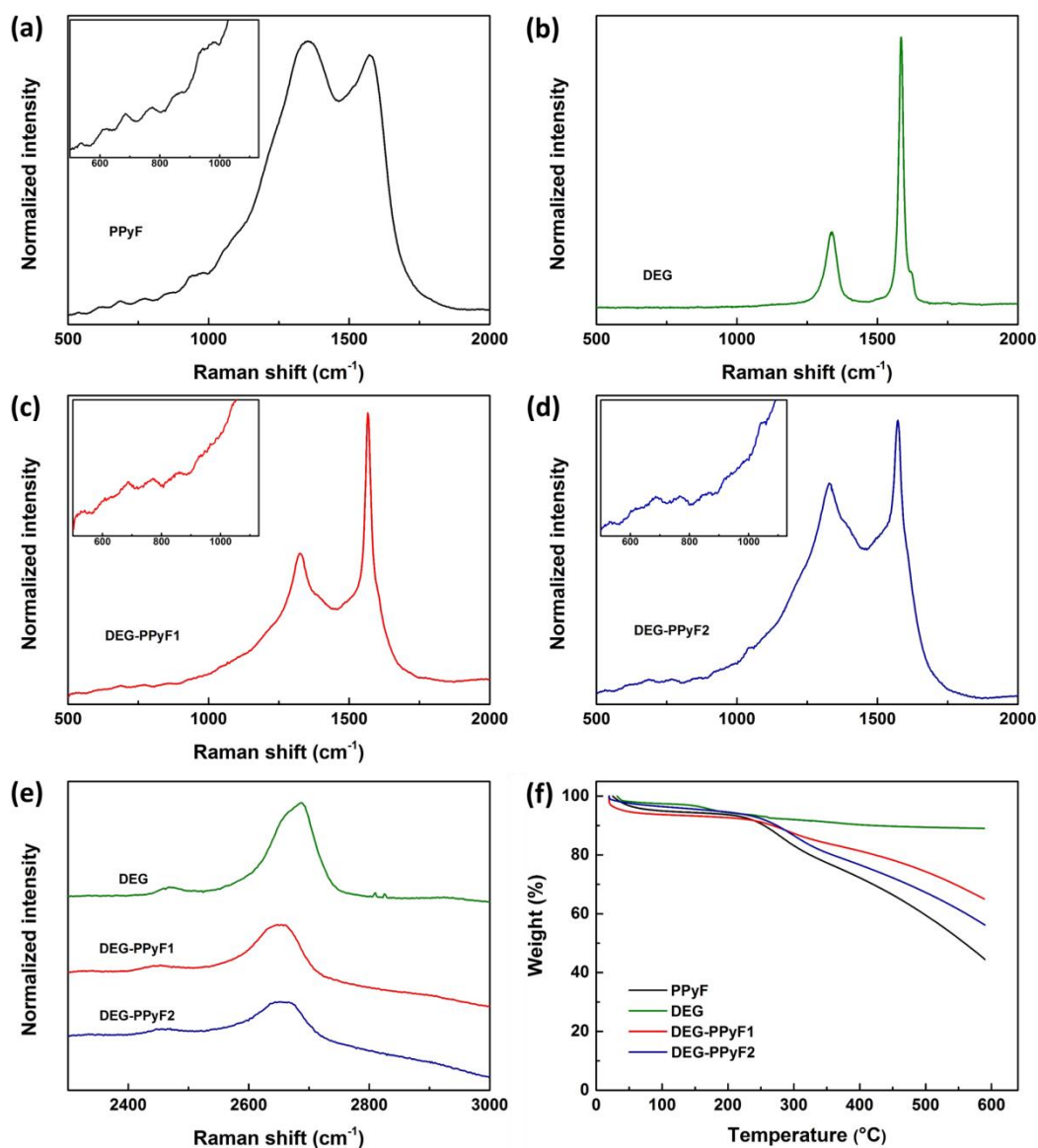


Figure 6.6 Raman spectra of PPyF (a), DEG (b), DEG-PPyF1 (c), DEG-PPyF2 (d) and 2D peak of DEG, DEG-PPyF1 and DEG-PPyF2 (e). TGA curves of PPyF, DEG, DEG-PPyF1 and DEG-PPyF2 film (f). (a, c, d inset: raman spectra between 500-1200 cm^{-1}).

6.3.3 Electrochemical performance of DEG-PPyF film

To study the capacitive performance, the film electrodes were assembled into Swagelok[®]-type cells using 1 M Li_2SO_4 electrolyte. Figure 6.7 shows the CV curves of PPyF, DEG, DEG-PPyF1 and DEG-PPyF2 films based supercapacitors. The CV curves

of PPyF film show a quasi-rectangular shape at a low scan rate of 20 mV s^{-1} . It became distorted with the increasing scan rate. At a scan rate of 400 mV s^{-1} , highly distorted leaf-shaped CV was presented indicating the limited ionic and electronic transport in bulk PPyF film. Due to the high conductivity and electrical double layer (EDL) capacitance feature, neat DEG film electrode can maintain the rectangular-shaped CV curves at such high scan rate (400 mV s^{-1}), but gives very low current response. With incorporation of DEG, the capacitive performance of DEG-PPyF composite film at high scan rate was significantly improved. The DEG-PPyF1 film can maintain a near-rectangular curve at 400 mV s^{-1} . For DEG-PPyF2 which has lower DEG ratio, a distorted CV shape was presented at the same scan rate. It can be found that the rate performance was improved with the increasing DEG ratio. In addition to the excellent rate performance, the DEG-PPyF1 still retained considerable high current response compared with DEG-PPyF2 and PPyF film. The specific capacitance at 20 mV s^{-1} was 170, 21, 120, 148 F g^{-1} for PPyF, DEG, DEG-PPyF1, DEG-PPyF2 film, respectively.

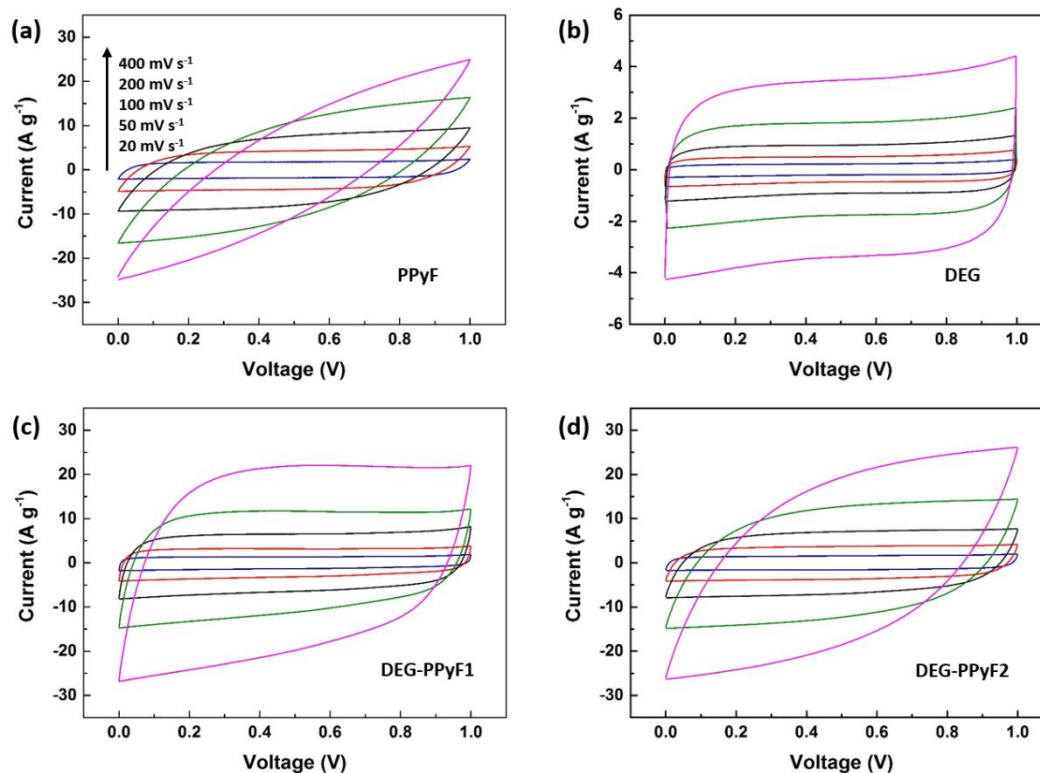


Figure 6.7 CV curves of PPyF (a), DEG (b), DEG-PPyF1 (c) and DEG-PPyF2 (d) film electrodes in 1 M Li_2SO_4 .

The charge/discharge tests were also investigated at different current densities, and the results are shown in Figure 6.8. Both PPyF and DEG-PPyF film electrodes displayed triangular or near triangular shaped curves at relatively low current density, suggesting their good capacitive performance. Due to the adsorbed surfactant and multilayered-graphene impurities during liquid exfoliation, DEG shows a very low capacitance of 20 F g^{-1} at 1 A g^{-1} , a value close to that for graphene via the graphite-exfoliation route [33]. At the same current density, PPyF film and DEG-PPyF2 film electrode have similar gravimetric capacitances of 152 F g^{-1} and 158 F g^{-1} respectively, while the DEG-PPyF1 film electrode offered a slightly lower capacitance of 130 F g^{-1} because of the increased DEG content. Suffering from limited conductivity and

electrolyte ionic accessibility, the PPy film electrode presents poor rate capability, showing a decreased capacitance of 120 F g^{-1} at 4 A g^{-1} , only 80% of the value obtained at 1 A g^{-1} . Meanwhile, the DEG film presents a capacitance of 20 F g^{-1} at 0.5 A g^{-1} . The performance of DEG film at higher current densities was not studied due to its low capacitance, even at low current density. The introduction of DEG sheets could effectively increase the conductivity and facilitate ion transport, thus render the composite electrodes DEG-PPyF1 and DEG-PPyF2 with better rate performance. The DEG-PPyF1 and DEG-PPyF2 films retained 98% and 91% of the initial capacitance (at 1 A g^{-1}) when the current density was increased to 4 A g^{-1} .

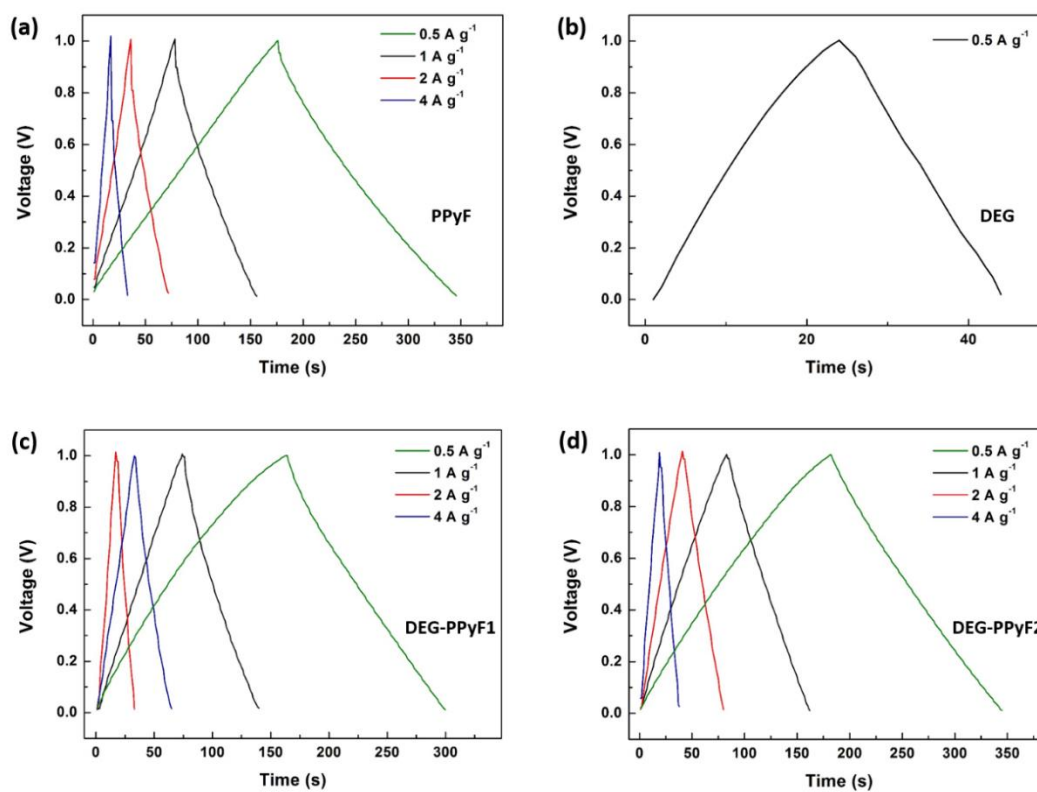


Figure 6.8 Charge/discharge curves of PPyF (a), DEG (b), DEG-PPyF1 (c) and DEG-PPyF2 film (d) electrode in $1 \text{ M Li}_2\text{SO}_4$

The rate performance and cycling stability of these film electrodes were compared from the galvanostatic charge/discharge tests (Figure 6.9a, b). The rate performance of DEG film was not evaluated due to its very low capacitance. The DEG-PPyF1 film with higher DEG content shows the best rate capability among these three electrodes. When the current density increased from 0.5 to 8 A g⁻¹, the capacitance retention was 94% (136 to 128 F g⁻¹). It was significantly improved, and much higher than that 56% (169 to 96 F g⁻¹) for PPyF film under the same condition. For DEG-PPyF2 film, the capacitance decreased from 161 at 0.5 A g⁻¹ to 128 F g⁻¹ at 8 A g⁻¹, also displaying a better capacitance retention (80%) than PPyF film. After 5000 cycles, the DEG-PPyF1 and DEG-PPyF2 films give a capacitance retention rate of 87 % and 82 % respectively, demonstrating their improved cycling stability compared with that (73%) for PPyF. The highly conductive DEG sheets employed resulted in such improved rate capability and cycle performance.

The Nyquist plots depict the relationship of imaginary and real parts of impedance at different frequencies ranging between 0.01 and 100 kHz, as shown in Figure 6.9c. Two types of equivalent circuit model are proposed to fit the Nyquist plots. For those film electrodes containing PPyF, the equivalent circuit includes three resistors, two capacitive elements and one Warburg element. The resistance elements include solution resistance R_s , double layer resistance R_{dl} , and electron transfer resistance R_{ct} . Two constant phase elements CPE_{dl} and CPE_f represent the double layer capacitance from the electrode-electrolyte interface, and the faradic pseudocapacitance from PPy redox reactions, respectively. Warburg element Z_w reflects the ion diffusion process between electrodes. According to the pure electric double-layer capacitance mechanism, the equivalent circuit for DEG film does not contain the elements of R_{ct} and CPE_f related to the pseudocapacitive redox reaction. The internal resistance, usually

named equivalent series resistance (ESR), can be calculated from EIS by the intercept of the semi-circle end with the real impedance axis. The total ESR of DEG and DEG-PPyF1 were around $\sim 12 \Omega$, which was lower than that of DEG-PPyF2 (18Ω) and PPyF (27Ω). The frequency response, which is plotted by the imaginary part of capacitance (C_{im}) against frequency, reflects the relative ion-transport rate within the electrode (Figure 6.9d). In the plot, the reciprocal of peak frequency is defined as relaxation time constant τ_0 , which describes the minimum time needed to discharge all the energy in the device with an efficiency $> 50\%$ [34]. A smaller τ_0 reflects a better frequency response of the electrode, indicating better rate performance. The relaxation time constant for DEG, DEG-PPyF1, DEG-PPyF2 and PPyF film is 12.6 s, 4.0 s, 1.2 s and 0.16 s respectively, which match well with the results of rate capability.

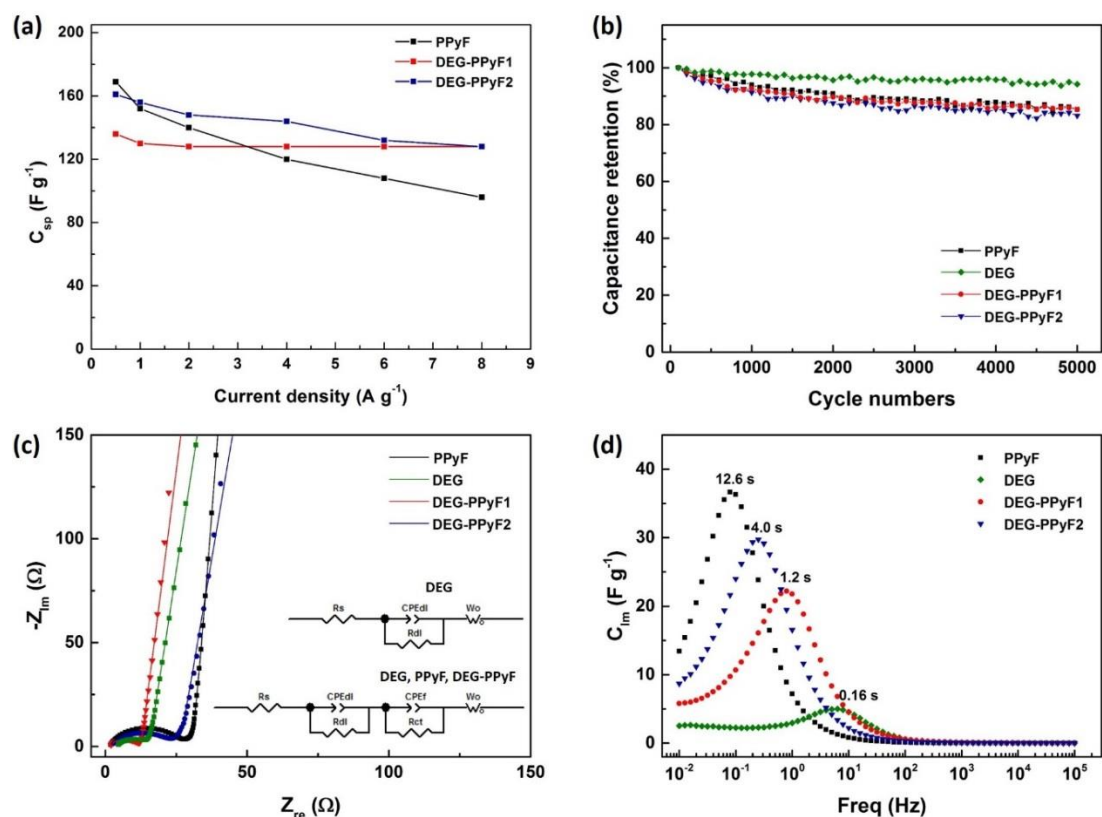


Figure 6.9 Rate performance (a), cycle stability (b), Nyquist plots (c) and frequency response (d) of DEG, PPyF and DEG-PPyF film electrodes. (c inset: proposed equivalent circuit)

6.4 Conclusion

In summary, a flexible free-standing graphene-polypyrrole fibre film was fabricated using graphene sheets directly exfoliated from worm-like expanded graphite with the assistance of a surfactant (CTAB). Raman spectrum revealed that such graphene contained weaker D peak than that of graphene obtained via exfoliated graphite oxide, indicating its less-defected structure. Following a tandem strategy, the surfactant after the liquid exfoliation was directly utilized as template for polypyrrole fibre synthesis without removal. The negative effect of the surfactant (insulator) on the electrochemical performance was minimized. In DEG-PPyF film, PPyF not only

provides large capacitance, but also improves the mechanical properties of the flexible film by binding and entangling the DEG platelets. On the other hand, the defect-free, highly conductive DEG can also effectively improve the rate capability of PPyF. The DEG-PPyF composite film electrode for supercapacitor demonstrated much larger capacitance than that of pure DEG film, and an improved rate capability compared to pure PPyF film.

6.5 References

- [1] S. Stankovich, R.D. Piner, X. Chen, N. Wu, S.T. Nguyen, R.S. Ruoff, Stable Aqueous Dispersions of Graphitic Nanoplatelets via the Reduction of Exfoliated Graphite Oxide in the Presence of Poly(sodium 4-styrenesulfonate), *Journal of Materials Chemistry*, 16 (2006) 155-158.
- [2] S. Stankovich, D.A. Dikin, R.D. Piner, K.A. Kohlhaas, A. Kleinhammes, Y. Jia, Y. Wu, S.T. Nguyen, R.S. Ruoff, Synthesis of Graphene-based Nanosheets via Chemical Reduction of Exfoliated Graphite Oxide, *Carbon*, 45 (2007) 1558-1565.
- [3] C.E. Hamilton, J.R. Lomeda, Z. Sun, J.M. Tour, A.R. Barron, High-Yield Organic Dispersions of Unfunctionalized Graphene, *Nano Letters*, 9 (2009) 3460-3462.
- [4] M. Lotya, Y. Hernandez, P.J. King, R.J. Smith, V. Nicolosi, L.S. Karlsson, F.M. Blighe, S. De, Z. Wang, I.T. McGovern, G.S. Duesberg, J.N. Coleman, Liquid Phase Production of Graphene by Exfoliation of Graphite in Surfactant/Water Solutions, *Journal of the American Chemical Society*, 131 (2009) 3611-3620.
- [5] M. Zhao, P. Liu, Adsorption of Methylene Blue from Aqueous Solutions by Modified Expanded Graphite Powder, *Desalination*, 249 (2009) 331-336.
- [6] M. Toyoda, M. Inagaki, Heavy Oil Sorption using Exfoliated Graphite: New Application of Exfoliated Graphite to Protect Heavy Oil Pollution, *Carbon*, 38 (2000) 199-210.
- [7] A. Sarı, A. Karaipekli, Thermal Conductivity and Latent Heat Thermal Energy Storage Characteristics of Paraffin/expanded Graphite Composite as Phase Change Material, *Applied Thermal Engineering*, 27 (2007) 1271-1277.
- [8] J. Bian, M. Xiao, S.J. Wang, Y.X. Lu, Y.Z. Meng, Novel Application of Thermally Expanded Graphite as the Support of Catalysts for Direct Synthesis of DMC from CH₃OH and CO₂, *Journal of Colloid and Interface Science*, 334 (2009) 50-57.
- [9] P.L. Zaleski, D.J. Derwin, R.J. Girkant, Method for Expanding Lamellar Forms of Graphite and Resultant Product, Google Patents, 2001.
- [10] R. Jalili, S.H. Aboutalebi, D. Esrafilzadeh, K. Konstantinov, S.E. Moulton, J.M. Razal, G.G. Wallace, Organic Solvent-Based Graphene Oxide Liquid Crystals: A Facile Route toward the Next Generation of Self-Assembled Layer-by-Layer Multifunctional 3D Architectures, *ACS Nano*, 7 (2013) 3981-3990.

- [11] G.S. Bang, H.-M. So, M.J. Lee, C.W. Ahn, Preparation of Graphene with Few Defects using Expanded Graphite and Rose Bengal, *Journal of Materials Chemistry*, 22 (2012) 4806-4810.
- [12] R. Hao, W. Qian, L. Zhang, Y. Hou, Aqueous Dispersions of TCNQ-anion-stabilized Graphene Sheets, *Chemical Communications*, (2008) 6576-6578.
- [13] L. Zhu, X. Zhao, Y. Li, X. Yu, C. Li, Q. Zhang, High-quality Production of Graphene by Liquid-phase Exfoliation of Expanded Graphite, *Materials Chemistry and Physics*, 137 (2013) 984-990.
- [14] S. Biswas, L.T. Drzal, Multi layered Nanoarchitecture of Graphene Nanosheets and Polypyrrole Nanowires for High Performance Supercapacitor Electrodes, *Chemistry of Materials*, 22 (2010) 5667-5671.
- [15] X. Zhou, J. Tang, J. Yang, J. Xie, B. Huang, Seaweed-like Porous Carbon from the Decomposition of Polypyrrole Nanowires for Application in Lithium ion Batteries, *Journal of Materials Chemistry A*, 1 (2013) 5037-5044.
- [16] H. Fu, Z.-j. Du, W. Zou, H.-q. Li, C. Zhang, Carbon nanotube Reinforced Polypyrrole Nanowire Network as a High-performance Supercapacitor Electrode, *Journal of Materials Chemistry A*, 1 (2013) 14943-14950.
- [17] S. Li, K. Shu, C. Zhao, C. Wang, Z. Guo, G. Wallace, H.K. Liu, One-Step Synthesis of Graphene/Polypyrrole Nanofiber Composites as Cathode Material for a Biocompatible Zinc/Polymer Battery, *ACS Applied Materials & Interfaces*, 6 (2014) 16679-16686.
- [18] S. Li, C. Zhao, K. Shu, C. Wang, Z. Guo, G.G. Wallace, H. Liu, Mechanically Strong High Performance Layered Polypyrrole Nano fibre/graphene Film for Flexible Solid State Supercapacitor, *Carbon*, 79 (2014) 554-562.
- [19] W. Gu, W. Zhang, X. Li, H. Zhu, J. Wei, Z. Li, Q. Shu, C. Wang, K. Wang, W. Shen, F. Kang, D. Wu, Graphene Sheets from Worm-like Exfoliated Graphite, *Journal of Materials Chemistry*, 19 (2009) 3367-3369.
- [20] B. Jiang, C. Tian, L. Wang, Y. Xu, R. Wang, Y. Qiao, Y. Ma, H. Fu, Facile Fabrication of High Quality Graphene from Expandable Graphite: Simultaneous Exfoliation and Reduction, *Chemical Communications*, 46 (2010) 4920-4922.
- [21] F. Tuinstra, J.L. Koenig, Raman Spectrum of Graphite, *The Journal of Chemical Physics*, 53 (1970) 1126-1130.

- [22] M. Wall, Raman Spectroscopy Optimizes Graphene Characterization, *Advanced Materials & Processes*, 170 (2012) 35-38.
- [23] A.C. Ferrari, J.C. Meyer, V. Scardaci, C. Casiraghi, M. Lazzeri, F. Mauri, S. Piscanec, D. Jiang, K.S. Novoselov, S. Roth, A.K. Geim, Raman Spectrum of Graphene and Graphene Layers, *Physical Review Letters*, 97 (2006) 187401.
- [24] D. Yang, A. Velamakanni, G. Bozoklu, S. Park, M. Stoller, R.D. Piner, S. Stankovich, I. Jung, D.A. Field, C.A. Ventrice Jr, R.S. Ruoff, Chemical Analysis of Graphene Oxide Films after Heat and Chemical Treatments by X-ray Photoelectron and Micro-Raman Spectroscopy, *Carbon*, 47 (2009) 145-152.
- [25] A. Ganguly, S. Sharma, P. Papakonstantinou, J. Hamilton, Probing the Thermal Deoxygenation of Graphene Oxide Using High-Resolution In Situ X-ray-Based Spectroscopies, *The Journal of Physical Chemistry C*, 115 (2011) 17009-17019.
- [26] L.M. Malard, M.A. Pimenta, G. Dresselhaus, M.S. Dresselhaus, Raman Spectroscopy in Graphene, *Physics Reports*, 473 (2009) 51-87.
- [27] S. Vadukumpully, J. Paul, S. Valiyaveetil, Cationic Surfactant Mediated Exfoliation of Graphite into Graphene Flakes, *Carbon*, 47 (2009) 3288-3294.
- [28] P. Krawczyk, J.M. Skowroński, Modification of Expanded Graphite Resulting in Enhancement of Electrochemical Activity in the Process of Phenol Oxidation, *J Appl Electrochem*, 40 (2010) 91-98.
- [29] X. Zhang, J. Zhang, Z. Liu, C. Robinson, Inorganic/organic Mesostructure Directed Synthesis of Wire/ribbon-like Polypyrrole Nanostructures, *Chemical Communications*, (2004) 1852-1853.
- [30] Y. Yang, C. Wang, B. Yue, S. Gambhir, C.O. Too, G.G. Wallace, Electrochemically Synthesized Polypyrrole/Graphene Composite Film for Lithium Batteries, *Advanced Energy Materials*, 2 (2012) 266-272.
- [31] L. Mao, H.S.O. Chan, J. Wu, Cetyltrimethylammonium Bromide Intercalated Graphene/polypyrrole Nanowire Composites for High Performance Supercapacitor Electrode, *RSC Advances*, 2 (2012) 10610-10617.
- [32] M. Omastová, M. Trchová, J. Kovářová, J. Stejskal, Synthesis and Structural Study of Polypyrroles Prepared in the Presence of Surfactants, *Synthetic Metals*, 138 (2003) 447-455.
- [33] L. Wu, W. Li, P. Li, S. Liao, S. Qiu, M. Chen, Y. Guo, Q. Li, C. Zhu, L. Liu, Powder, Paper and Foam of Few-Layer Graphene Prepared in High Yield by

Electrochemical Intercalation Exfoliation of Expanded Graphite, *Small*, 10 (2014) 1421-1429.

[34] P.L. Taberna, P. Simon, J.F. Fauvarque Electrochemical Characteristics and Impedance Spectroscopy Studies of Carbon-Carbon Supercapacitors, *Journal of The Electrochemical Society*, 150 (2003) A292-A300.

7 Conclusion and Outlook

This thesis has been dedicated to develop novel flexible graphene electrodes with high performance, combined with good mechanical strength, for energy storage devices. Different routes/strategies have been applied to prevent graphene sheets restacking. Flexible graphene papers with porous structure have been fabricated via freeze-drying technology, using either graphene solution or graphene wet gel as precursor. This successfully addresses the restacking problem during the graphene paper forming process. With the incorporation of polypyrrole, the areal capacitance of obtained graphene composite paper is greatly enhanced and this moves one big step forwards towards practical applications. The use of graphene obtained via direct solvent exfoliation instead of the graphite oxide route, as building block to construct high performance flexible electrodes, further expands the source of graphene for flexible electrode fabrication. These results obtained in this thesis would provide useful information in the development of graphene-based flexible electrodes for flexible energy storage devices.

The future key challenge to bring laboratory-based electrode materials into practical applications is to enable large production of these materials while maintaining their performance. In this study, techniques such as freeze drying, filtration, electropolymerization are involved to develop high performance graphene based flexible electrodes. Filtration has been proven to be a facile method to make graphene paper/film, and freeze drying was a simple, versatile, low-cost fabrication technique to construct a porous structure. These techniques and strategies allow the easy production of electrodes with larger thickness and dimensions with appropriate apparatus. Owing to the ordered nanostructure, the performances of materials with enlarged thickness or

dimensions are expected to be maintained. The weight of graphene based flexible electrodes can also be scaled up from milligram to subgram scale, thus ensuring better simulation of practical case studies.

Recently, more and more research has been focused on increasing the areal capacitance to meet the requirements of practical applications. In this thesis, PPy was deposited on the filtration formed graphene wet gel via electropolymerization, producing flexible graphene/PPy paper with large areal loading mass. It provided greatly enhanced areal capacitance with considerable gravimetric capacitance. This strategy can also be applied to deposit alternative active materials. Other conductive polymers such as polyaniline and PEDOT can be introduced to fabricate high performance electrode for flexible supercapacitors. When combined with metal oxides using similar electrodeposition methods, the resultant graphene composite paper can be used for flexible batteries. It is suggested that, for an electrode that is practically used, the areal mass loading should be at least 5 mg cm^{-2} , with a thickness range between 50-200 μm . Incorporating appropriate active materials, our flexible graphene composite electrode is able to reach these standards.

Another trend in current energy storage research is to scale down the device. Miniaturized energy storage devices are crucial for energy autonomy, to meet the increasing demand for autonomous electronic systems and wireless technology. Inspired by the technique of assembling all solid-state supercapacitor applied in this work, we are able to produce graphene based paper-like battery or supercapacitor. By changing the preparation condition, it is also possible to develop thinner flexible graphene based electrodes. The conformable shape enables integration of paper-like energy storage devices between and around a variety of structures and materials in products ranging from disposable medical, connected devices and wearable consumer electronics.

Combining with techniques such as laser patterning, these graphene based ultrathin films will be promising electrode materials for miniaturized power sources.

Finally, the materials we used to fabricate flexible electrodes—graphene and PPy—are cytocompatible. They have already been used for biomedical applications including drug delivery, biosensor, cell culture scaffold, etc. Therefore our graphene and graphene composite flexible electrodes can be easily designed to meet the requirements of flexible miniaturized implantable medical devices. In addition, these electrodes can easily find their application in bio-batteries (coupled with bioresorbable Mg or Mg alloy electrodes). Our research into flexible graphene paper will enable further development of flexible power sources for wearable and implantable devices in the future.